University of Padova

Department of Physics and Astronomy 'Galileo Galilei'

Master Thesis in Astrophysics and Cosmology

Investigating the mineralogical composition of Martian crater and intercrater deposits in Meridiani Planum using CRISM spectral data

Supervisor
Matteo Massironi
University of Padova

Co-supervisor
Beatrice Baschetti
University of Padova

Master Candidate
Marco Baroni

Student ID
1238631

Academic Year
2022-2023

"Dedication or Quote"
— Someone

Abstract

Meridiani Planum is a plain on Mars located near the equator south west of Arabia Terra. Its southern part was studied for about 14 years by the MER Opportunity rover, which landed on the 25th of January 2004. The rover detected hydrated and water altered minerals such as sulfates, phyllosilicates and hematite spherules. Other than the presence of hydrated minerals, Meridiani Planum harbors morphological features related to water erosion such as valley networks that cut the oldest units of this region, and most importantly, it hosts a thick sequence of sediments rich in hydrated minerals, which were deposited at the boundary between the Noachian and the Hesperian epochs. During this transition Mars evolved from being a warm and wet planet to the cold and dry place it is today. On the 10th of March 2006 the Mars Reconnaissance orbiter successfully entered orbit around Mars carrying with it some of the most advanced instruments at our disposal today. Among this instruments the Compact Reconnaissance Imaging Spectrometer for Mars (CRISM) permitted the gathering of high resolution reflectance spectroscopy data having resolution of 15-19 m/pixel and bandwidths of 6.55 nm/channel, and together with the High Resolution Imaging Science Experiment (HiRISE), that possesses a peak resolution of 0.3 m/px, and the Context Camera (CTX) provided information and data used in unprecedented discoveries about our neighboring planet. Using CRISM most advanced products called MTRDR we analyzed three regions in Meridiani Planum, the north portion of the Kai crater, and other two areas, located northwest and north of a formation called Piscinas Serpentes, specifically an unnamed small oblique impact crater and a portion of a intercrater formation. To do the analysis we developed an original Python pipeline composed of RGB map generation, spectra extraction, spectra normalization and spectra comparison including three different methods of spectra normalization to enhance the spectral characteristics. We located and identified deposits of hydrated minerals analyzing different regions of interest. In all of the studied regions we have found presence of several sulfates and phyllosilicates mineralogical phases belonging to different geological units. This suggests that the different hydrates minerals were deposited during several separate events, implying a difference in the presence and activity of water in the area during the timespan between late Noachian and early Hesperian. In the first region we have selected 8 different zones of interest in which we have found monohydrated sulfates, polyhydrated sulfates and Al, Mg and Fe smectites in different relative stratigraphic position and elevation. Regarding the second region we have selected 7 zones in which we have found Mg smectite and talc deposits in the crater basin with deposits of monohydrated and polyhydrated sulfates and traces of Al smectite on the outer south rim of the crater. Finally, regarding the intercrater formation we have selected 5 zones in which we have found polyhydrated and monohydrated sulfates, Mg/Fe smectites and talc. Combining the spectral information with Digital Terrain Models from CTX and HiRISE cameras, we can characterise the stratigraphic relationships between the clay and sulfate layers.

Contents

Listing of acronyms

. . . . . **CRISM**: Compact Reconnaissance Imaging Spectrometer for Mars

. . . . . **FRT**: Full Resolution Targeted

. . . . . **MRO**: Martian Reconnaisance Orbiter

. . . . . **MTRDR**: Map-Projected Targeted Reduced Data Record

. . . . . **ROI**: Region Of Interest

1 Introduction

1.1 General Characteristics of Mars

Mars is the fourth planet of the Solar System and its orbit is located between the orbit of Earth and the Asteroid Belt. It is a telluric planet just as the other inner planets. It is the second smaller telluric planet of the Solar System and one of the two with satellites (Phobos and Deimos). It has a mass approximately of a tenth of the Earth's, with a radius that is slightly more than half of Earth's, thus implying a very low density: around a fifth of that of the Earth.
These characteristics are coupled with a mean surface temperature of ~209 K, with minimum temperatures averaging at ~163 K and maximum temperatures averaging at ~293 K (above water freezing point, but only in some zones and in some periods) and an atmosphere made by CO_2 (95%), N_2 (2.8%), Ar (2%), O_2 (0.174%), CO (0.0747%) and with a small variable content of H_2O (that averages at 0.03%) (Franz et al., 2017).
The atmosphere is really thin and the atmospheric pressure at the height of the reference ellipsoid is 0.6% of Earth's. This implies that water can be present only in vapour and/or solid phase, given that the mean temperature and pressure are below the triple point of water.
Mars is differentiated into a crust, a mantle and a core that are in average 50 km, 2146 km and 1794 km thick respectively. Although the core is partially melt the planet does not exhibit a permanent magnetic field.
The martian crust is composed mainly by silicon and oxygen with notable percentages of iron,

Table 1.1: Mars' principal physical and orbital characteristics.

Physical Characteristics	
Mass [$M_\oplus$]	0.107
Radius [$r_\oplus$]	0.5316
g [m/s²]	3.7276
Mean Synodic Day [h:m:s]	24:39:36
Axial Tilt [°]	25.19
Geometric Albedo	0.17
Surface elevation range [km]	-8.2 to 21.2
Mean Temperature [K]	209
Mean Atmospheric Pressure [atm]	0.00628
Approx. Atmospherical Composition [%]	95 CO_2, 3 N_2, 2 Ar
Tropical Year [days]	686.9725
Orbital Characteristics	
a [AU]	1.523
e	0.0934
M [°]	19.412
i [°]	1.63
Ω [°]	49.57854
ω [°]	286.5

magnesium, aluminum, calcium, and potassium. The surface of Mars harbours some of the most astounding surface morphologies of the Solar System such as the Tharsis bulge, the Olympus Mons (the tallest volcano in the Solar System, being 21.9 km tall (Comins, 2009), see figure 1.1 B) and the canyon system of Valles Marineris (see figure 1.1 A).
Although Mars seems now a cold and dusty desert covered by craters, the presence of valley networks (see figure 1.4B) and the presence of hydrated minerals such as phyllosilicates suggests that liquid water may have been flowing on the surface during the past. There is even the possibility that large water bodies accumulated as an inner sea in Hellas Planitia (see figure 1.1C) and as a global ocean in the northern lowlands (Carr, 2012). A comprehensive table of the principal physical and orbital features is shown in Table 1.1.

1.1.1 Geological History

The geological history of Mars has been divided into 4 main eras on the basis of the relative ages of different geologic events, dated from the number of superimposed impact craters on

the related terrain units (Tanaka, 1986). Each era is named after the Planitiae encompassing the geological units of reference for that given age (Carr and Head, 2010).

A summary of the main events per epoch is presented in figure 1.2 and a map showing units

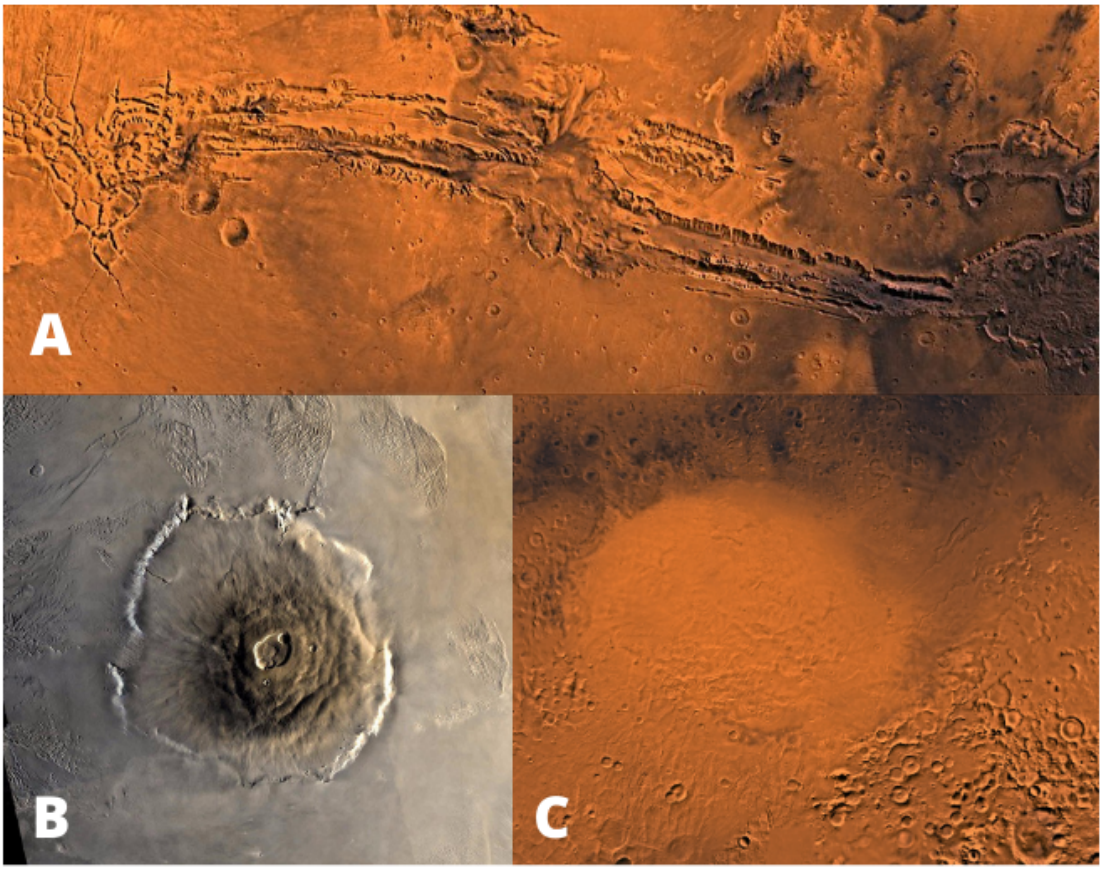

Figure 1.1: Examples of some of the most notorious Martian formations: **A** shows the Valles Marineris canyion systems, **B** shows the volcanic edifice of Olympus mons and **C** shows Hellas Planitia. Credits: NASA/JPL/USGS

with different crater chronology dated terrain is shown in figure 1.3:

- **Pre Noachian**: from 4.5 to 4.1 billion years ago. During this period Mars formed and differentiated, probably developing a global magnetic field (Solomon et al., 2005). Moreover during this era it is thought that the global dichotomy (still visible today) formed (Carr and Head, 2010). The events of this period are uncertain since most of the evidence has been erased by subsequent events;
- **Noachian**: from 4.1 to 3.7 billion years ago. The Noachian begun with the formation of the Hellas Basin (see figure 1.1 B). It is during this period that most of the huge Tharsis bulge formed (Carr and Head, 2010). Notably, in this era Mars had environmental

conditions enabling the formation of water-related weathering products such as phyllosilicates (Carr and Head, 2010). Lots of evidences of erosive processes that happened during this time are visible on the surface, such as the highly eroded rims of the large Noachian craters that contrast with the well maintained craters from the subsequent Hesperian era. The erosional rate estimated for the Nochian period is still well below Terrestrial rates: being as small as 5 μm/yr, while Earth exhibits erosional rates of about 47 cm/yr (Carr and Head, 2010). Another evidence of these erosive processes are the valley networks (see figure 1.4B) that could have been sustained by atmospheric precipitation (Carr and Head, 2010). Many craters also exhibit inlet and outlet valleys (Fassett et al., 2015), with even deltas observed in some cases (e.g. Eberswalde crater, see figure 1.4A), which suggests that these craters could have hosted lakes. Finally, in some areas it is possible to observe erosional debris deposits of sedimentary origin that in some cases presents a remarkable rhythmic layering (Lewis et al., 2008), (Zabrusky et al., 2012). From all the evidences above, it is thought that at least episodic warm and wet conditions were present on Mars during the Noachian (Carr and Head, 2010);

- **Hesperian**: from 3.7 to 3 billion years ago. The boundary between the Noachian and Hesperian is currently under debate but crater densities suggest that the period begins with the end of the Late Heavy Bombardment [1] (Hartmann and Neukum, 2001). It is during this period that the Valles Marineris (see figure 1.1A) is thought to have formed. Together with the continuing lava emplacement the main characteristics of this period are the steep decline in the formation of valley networks, the cessation of phyllosilicate formation and the local accumulation of sulfate-rich deposits (Carr and Head, 2010). Particular structures called ridged plains are thought to have formed during the Hesperian (Greeley and Spudis, 1981). The richness in olivine of the low-dust Hesperian plains likely implies limited chemical weathering(Putzig et al., 2005). Despite the global rate of valley formation declined steeply, the conditions for the formation of small valleys were enabled locally, for example from the geothermal melting of snow caps on volcanoes (Fassett et al., 2015). In addition, outstanding features of the Hesperian age are the outflow channels (see figure 1.4C) probably carved by huge flash flooding events triggered by sudden melting and release of groundwater icy aquifiers (permafrost), due to impact events or magmatic injections.
  The largest Hesperian flood features found up to today suggest a peak discharge between 10^7 and 10^8 m^3/s (Leask et al., 2007). Some estimate of the maximum regional erosional rate were extrapolated from the Gusev crater and the landing site of Pathfinder and were find to be between 20 and 30 μm/yr. As mentioned before, a distinctive feature of the Hesperian period is the accumulation of sulfate-rich deposits, especially in Meridiani

[1] The Late Heavy Bombardment (LHB), is a hypothesized event thought to have occurred approximately 4.1 to 3.8 billion years ago. According to the hypothesis, during this interval, a disproportionately large number of asteroids and comets collided with the early terrestrial planets in the inner Solar System, including Mercury, Venus, Earth and Mars.

Planum and around the North Pole (Carr and Head, 2010). Sulfate minerals can form by weathering of basalts from various processes such acid fogs, fumarolic condensates and groundwater affected by magmatic volatiles (Madden et al., 2004). They can also form as evaporite deposits from the evaporation of standing bodies of water;

- **Amazonian**: from 3 billion years ago up to today. As the boundary between Noachian and Hesperian, also the boundary between Hesperian and Amazonian is currently under debate. However, it is collectively agreed that the Amazonian is the longest geological era of Mars. It is in this period that the layered ice terrains located at the poles are thought to have formed(Carr and Head, 2010) and indeed one the most distinguishable features of the Amazonian era are the various effects of the action of ice, particularly at mid to high latitudes, as well as processes driven by obliquity variations (Carr and Head, 2010) like deposition and subsequent destruction of ice at low latitudes and polar ice caps migration. Another distinctive feature is the huge drop in volcanic activity and its confinement in the area of Tharsis and Elysium. Few outflow channels are documented to have formed during the Amazonian, such the Athabasca, Grjota, Rahway and Marte Valles in the southeast Elysium, whose crater ages range between 2 to 140 Myr (Berman and Hartmann, 2002), however, the most common fluvial-like feature of the Amazonian are the gullies (see figure 1.4D) and the related debris fans originated from crater rims. These formations are typically found in the 30°-60° latitude belts and are most abundant in the southern hemisphere. Their origin is still under debate, but there is broad consensus in relating them to water erosional processes (Carr and Head, 2010), probably associated to permafrost or snow melting processes during periods of high obliquity (Head and Marchant, 2003).

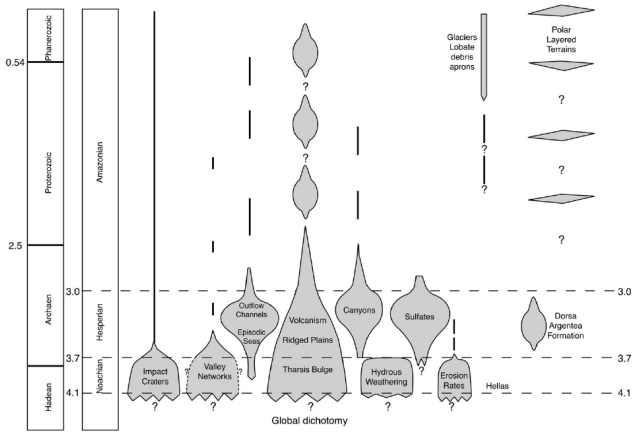

Figure 1.2: Geological activity as a function of time on Mars. This diagram shows the relative importance of different processes (impact cratering, volcanism), the time and relative rates of formation of various features and units (valley networks, Dorsa Argentea Formation), and the types and rates of weathering, as a function of time. The approximate boundaries of the major time periods of Mars history are also shown (Hartmann and Neukum, 2001), and are compared to similar major time subdivisions in Earth history (Head and Marchant, 2003).

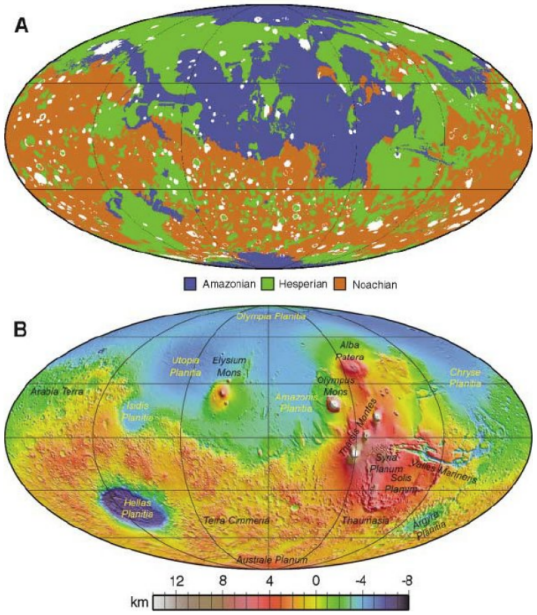

Figure 1.3: Map that relates topography and assigned age (Solomon et al., 2005). It is easy to see that a huge part of the southern highlands are Noachian in age, while the northern lowlands are younger being almost everywhere Hesperian or Amazonian in age.
A is the depiction of the ages of the different terrains while **B** is the topographic map of Mars. Credits: William Bruce Banerdt.

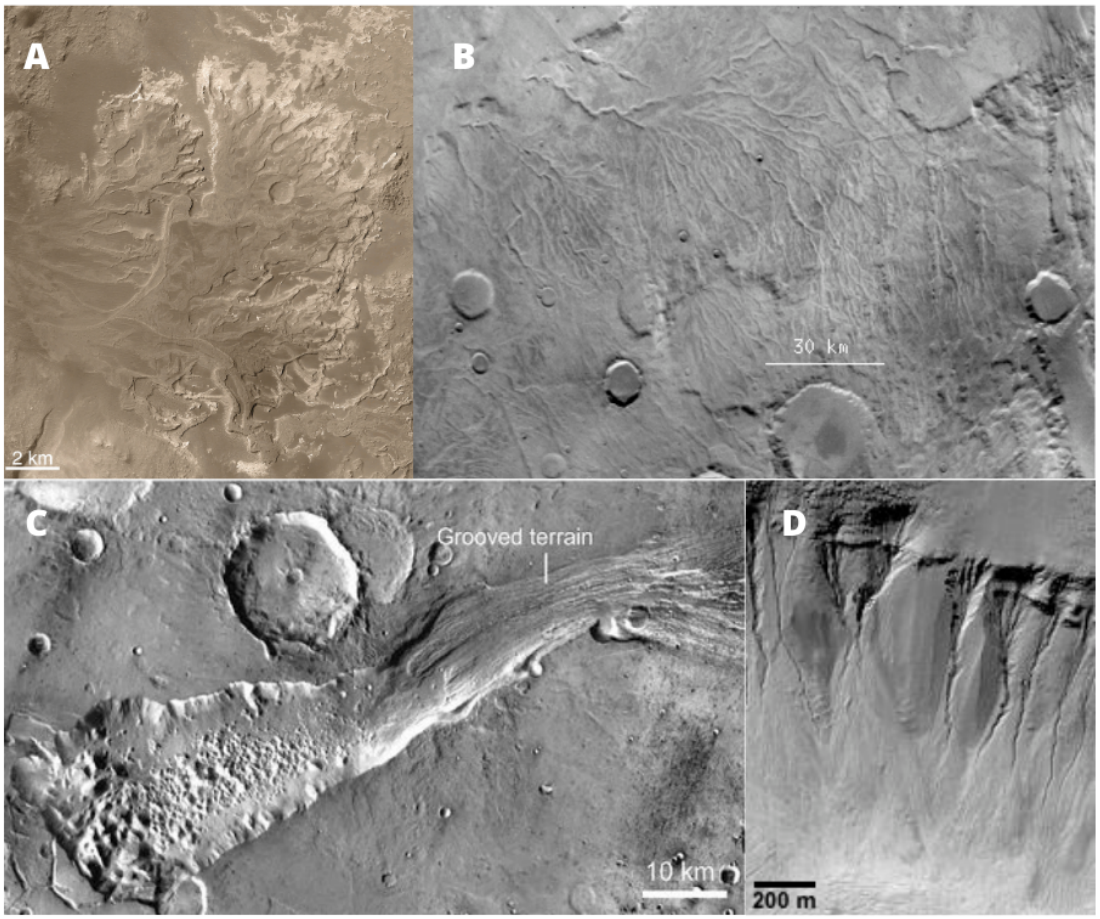

Figure 1.4: A: fluvial delta in Eberswalde crater. **B**: example of valley networks representing the Warrego Valleys. **C**: example of outflow channel representing the Ravi Vallis. **D**: example of gulleys located in an unnamed crater.
It is worth to notice the difference in dimension and complexity, especially regarding image A and image B: valley networks presents themselves as thinner and have lots of tributaries, while outflow channels presents less, if none, tributaries and presents larger beds. Credits: NASA/JPL/Malin Space Science Systems.

1.1.2 The Noachian/Hesperian Transition and the Past Martian Climate Hypothesis

Both morphological and mineralogical evidence clearly indicate that the climate of Mars experienced a transition from a warm and wet climate to a more arid one during the Late-Noachian to Early-Hesperian timespan. This trend eventually led to the hyperarid and cold climate we observe from the Amazonian to present times. However, it is still not clear what might have caused this drastic shift and how exactly surface conditions changed. Moreover, the existence of a sustained warm and wet climate in the Noachian is itself object of debate.

Other than the already cited valley networks and phyllosilicates presence, also hydrological models give hints about the abundance of water in the Noachian with levels mantained stable by atmospheric precipitation. The same models seems to suggest a solution involving large impacts and interaction with the solar winds as agents that may have been responsible for the lowering in the groundwater table and in the rarefaction of precipitation events (Andrews-Hanna and Lewis, 2011). However, topographic changes phenomenon such as crater formation or volcanic-driven upliftings could have created local groundwater upwelling, providing sparse hydric reservoirs to trigger episodical fluvial events in the Hesperian (Andrews-Hanna and Lewis, 2011) that could have formed local lakes that, by subsequent evaporation, left behind the sulfates we observe today in zones like Meridiani Planum (Carr, 2012).

In any case, even if hydrological models and observations seems to agree with a wet Noachian, stellar evolution models pose some challenges to the existence of such climate on ancient Mars: during that period the Sun had a luminosity of $\sim 75\%$ of its present value, implying a mean temperature for Noachian Mars of ~ 196 K without greenhouse warming but also considering a greenhouse effect that takes the temperature up to 273 K it would require Noachian Mars's atmosphere to intercept at least 85% of radiation from the surface. Assuming an atmosphere of mainly CO_2 and H_2O considering modern models for early terrestrial planets (Pepin, 1994), it could not have been possible to warm the surface higher than ~ 230 K, no matter how thick this primordial atmosphere could have been (Kasting, 1991). In this perspective, surface features related to water runoff and the aqueous mineralogy might have been formed during transient warm conditions, possibly related to atmospheric injection of CO_2, SO_2 and other greenhouse gases by massive volcanic events, which initiated hydrological cycles (Baker, 2001). Another possible explanation could be related to craterization processes: small to medium size impactors could have released huge amounts of greenhouse gases such as CO_2 and CH_4 in the atmosphere.

Lastly, another major issue, which challenges the warm and wet climate hypothesis, is the lack of abundant carbonates on the Martian surface (Ehlmann et al., 2008), (Ehlmann and Edwards, 2014). On primordial Earth is thought that inorganic carbonates formed by interaction with the oceanic water with the CO_2 contained in the atmosphere. If this was a similar scenario for Mars then a possible explanation for their absence could be related to the possibility of limited permanence of liquid water on the surface of Mars (Bibring and OMEGA Team, 2006). However, that would be in contrast to the widespread presence of phyllosilicates, which are a common aqueous mineral, especially on Noachian surfaces. Other explanations could be related to acidification of the Martian environment, which could have destroyed the carbonates, or the complete absence of a dense CO_2 in the history of Mars (Bibring and OMEGA Team, 2006).
All of this said, it is clear that the climate between the Noachian and the Hesperian is still a hot topic in the scientific community and further investigations are surely needed. Key information about this might be retained in areas which preserve sedimentary rock formations dating back to this boundary.

1.2 Meridiani Planum

Meridiani Planum is a plain area on Mars located in the southwest part of Arabia Terra (see figure 1.5). The first peculiar characteristic of Meridiani Planum is the widespread presence of ferric oxide in the form of Hematite crystals, Fe_2O_3, that is not usually detected in other zones over the surface of Mars. Moreover, on Earth, hematite can form in hydrothermal pools and/or in stagnant pools of water, suggesting the past presence of liquid water over this particular zone of Mars. From crater counting methods it is estimated that most of Meridiani Planum is between 3.36 and 3.85 Gyrs ago, so between the late Noachian and Early Hesperian (Zabrusky et al., 2012). On the 25th of January 2005, the rover Opportunity landed in Meridiani Planum and, during its journey observed, other than the presence of hematite in the form of spherules (see figure 1.6B), the presence of evaporitic deposits composed by sulfates and iron oxides (see figure 1.6A). This type of deposits are generally thought to form in playa environments (Grotzinger et al., 2005) or, more specifically, the presence of both hematite and sulfates indicate that aeolian grains were sourced from an evaporitic-cemented altered basalt, deposited in a playa or dune field environment and then cemented in dunes and inter-dunes areas by sulfate evaporites and groundwater (Zabrusky et al., 2012).
Studies made with satellite images of similar sulfates deposits over Arabia Terra set the age for

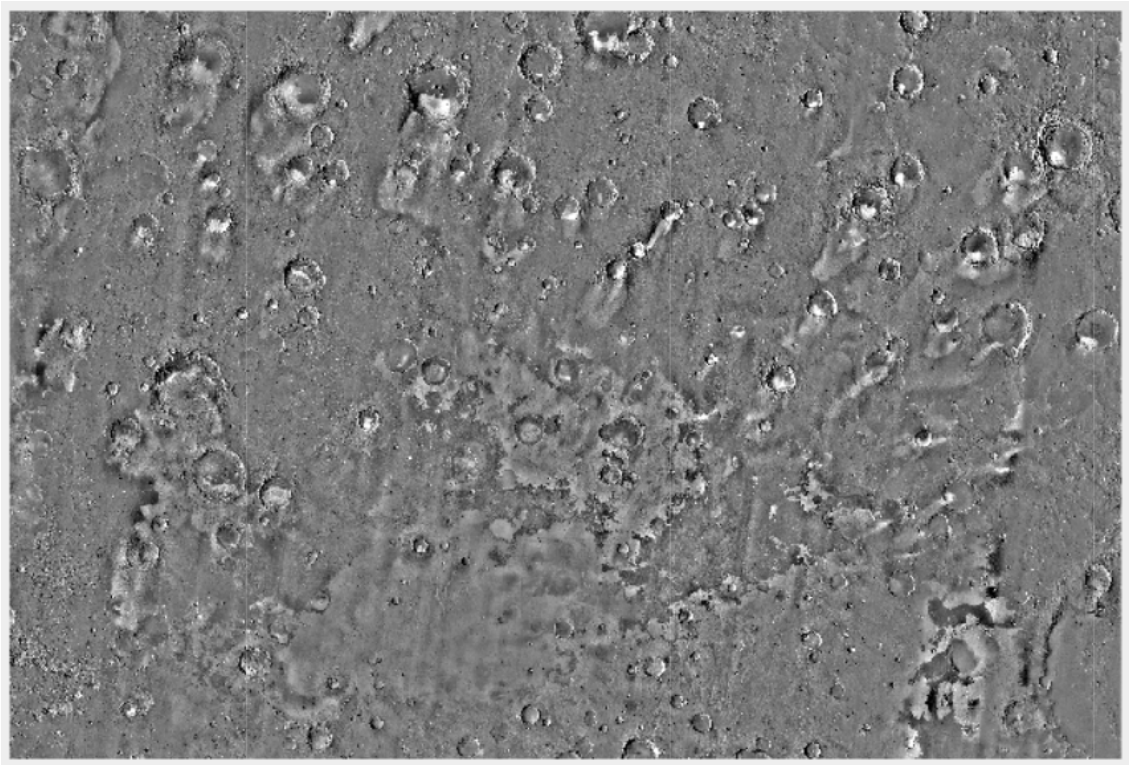

Figure 1.5: Approximate area of Meridiani Planum. The image is a mosaic of THEMIS daytime thermal inertia with a resolution of 100 m/px with portions not covered by THEMIS covered by Viking images. The map covers an area that covers $(\Delta\lambda,\Delta\varphi) = (30^\circ,20^\circ)$ covering from 345° to 15° in longitude and from -5° to 15° in latitude.
Credits: Hynek & Di Achille

this process of deposition and erosion between 3.5 and 3.8 Gyrs ago (Zabrusky et al., 2012), making the age of this deposition similar to the age of Meridiani Planum itself (late Noachian-early Hesperian). Particularly, from the geological map provided by (Hynek and Di Achille, 2017), the hematite fields explored by Opportunity are Early Hesperian in age, while older zones (such as the one studied in this work) have terrains that goes from Early Noachian to Late Noachian. Specifically, the Early Noachian terrain displays lots of valley networks and highly eroded craters often filled with Late Noachian-Early Hesperian deposits.
Other than sulfates and hematite, from data of the OMEGA mission, in Meridiani Planum are also detected phyllosilicates (Bibring and OMEGA Team, 2006). These phyllosilicates could have an aqueous origin separate from that of the sulfates, but it is nonetheless peculiar to see phyllosilicates and sulfates in the same zone.
The most puzzling question about Meridiani Planum is the fact that, stratigraphically, being phyllosilicates associated with Noachian terrains and sulfates associated with Hesperian ter-

rains (Bibring and OMEGA Team, 2006), we should expect to find sulfates always on top of clays. However, in this area interbedded layers of clays and sulfates are found, raising questions about a possible oversimplification of the boundary between Noachian and Hesperian (Baschetti et al., 2022).

Overall, Meridiani Planum is one of the most interesting zones on the surface of Mars and is also the object of study of this work. Particularly, we selected three targets located in a terrain Noachian in age (Hynek and Di Achille, 2017) located about 200 km northeast of the hematite bearing field partially explored by Opportunity (see next chapter). This zone of Meridiani Planum is dissected by valley networks and shows highly degraded impact craters with infilled floors (Hynek and Di Achille, 2017). Moreover, sedimentary units that are scattered throughout all Meridiani Planum are also found near the center of our unit and it is one of the region we have studied together with one small unnamed crater and the upper part of Kai crater. All of these targets have hints about the presence of sulfates deposits as well as clays both in layered sediments and in local deposits, thus being ideal targets of interest to investigate the composition of Meridiani Planum's deposits and their origin.

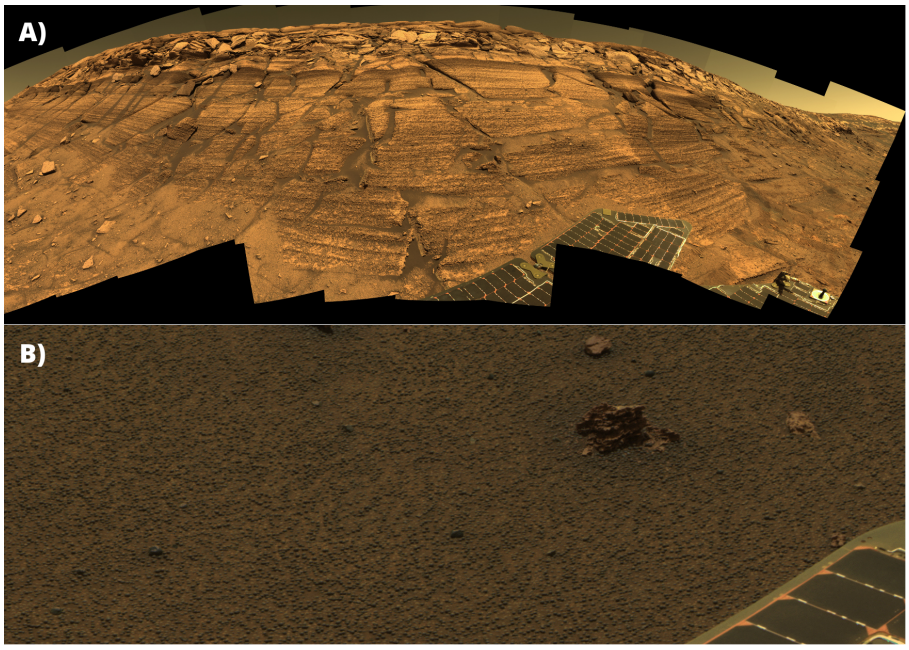

Figure 1.6: A): Mosaic image of Burns Cliff in Endurance Crater. This image is one of the best images taken by Opportunity's Pancam. It has a "fish eye" view distortion. Burns Cliff is at least 7 m tall (Grotzinger et al., 2005). Sediment cliffs as big as Burns Cliff are not common and they only occur in large Meridiani craters.
B): Detail showing hematite spherules eroding out of blocks of sediment ejecta. Notice the increased surface density of loose spherules lying in rings around the small clocks of sediment ejecta.

1.3 Geological Setting of the area of interest

Our targets are all placed in a terrain dated to the early-middle Noachian. This terrain is surrounded mainly by terrains dated to the early Hesperian and have small regions in which it is contact with later middle Noachian terrain in the North and with the Hematite field partially explored by Opportunity in the South (Calvin et al., 2008). In figure 1.7 we present the geological map of Meridiani Planum (Hynek and Di Achille, 2017). Our targets are placed within the Early-Middle Noachian unit called Nhc1, which is one of the oldest in the area (figure 4.3 shows a closer view of our study area). In this region we also find some small patches of HNMeu and HNme3, which are both dated between the Noachian and the Hesperian. Specifically, the infilling of Kai crater is part of HNMeu unit, while Piscinas Serpentes area partly belongs to HNMeu3. The unnamed oblique impact is mapped as part of Nhc1. The last relevant unit for our analysis is the c1 crater unit, that refers to craters from early to middle-late Noachian. The ages of these geological units as given by (Hynek and Di Achille, 2017) are schematically shown in figure 1.8. Following we report the description of the mentioned geological units as given by Hynek and Di Achille (2017):

- **Nhc_1** displays relatively low albedo and moderate thermal inertia. Posses highly degraded impact craters characterized by subdued rims and infilled floors. Dissected by integrated valley networks. Composed by mixture of volcanic deposits, impact breccias and sediments. These sediments come from fluvial and eolian processes. In general, it formed during the Late Heavy Bombardment and was modified by fluvial processes;
- **$HNme_3$** posses high albedo and high thermal inertia rugged surface features. Images from HiRISE and CTX shos deposits composed of horizontal to sub-horizontal bright layers. It probably formed as a result of groundwater-cemented eolian deposits and/or volcanic depositional processes. In the past it was probably more contiguous, as numerous isolated outliers seems to suggest, and was probably broken down by processes such as eolian erosion;
- **$HNme_u$** units have lower albedo and thermal inertia when comapred to $HNme_3$ units. The surfaces of this unit posses various degrees of ruggedness, from tabular to rugged and are intensely affected by eolian erosion. As for $HNme_3$, also for this unit high resolution images shows deposits of horizontal/subhorizontal layers probably formed, again, as result of groundwater-cemented eolian deposits and/or volcanic depositional processes;
- **c_1** represents degraded crater material which craters shows absence of central peaks or peak ring structures and the ejecta are not visible and, moreover, their crater floors are often overlaid by internal layered deposits.

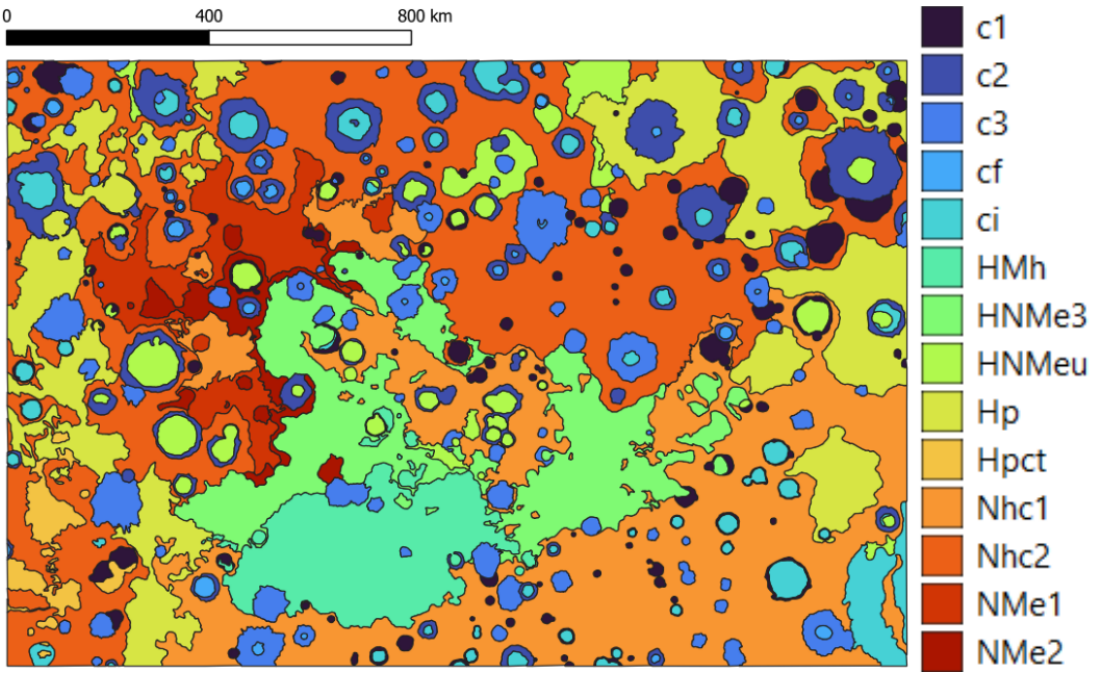

Figure 1.7: Geological map of Meridiani Planum, adapted from (Hynek and Di Achille, 2017). Colors are different from the original map and surface features are not shown.The North is in the upward direction. Credits: (Hynek and Di Achille, 2017).

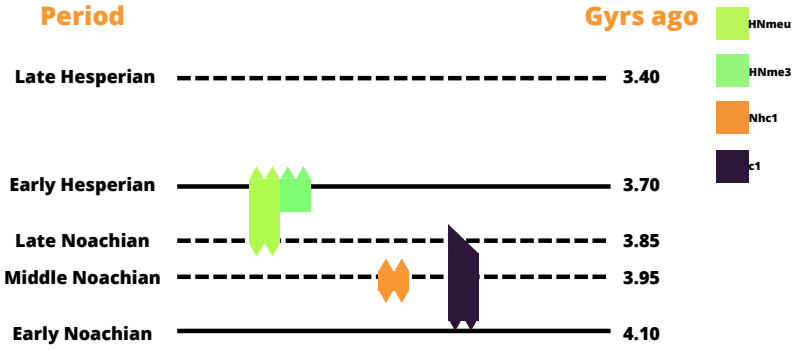

Figure 1.8: Approximate ages of the units that are found in our area. The colors are the same from the geological map in figure 1.7. The serrated border indicates that the contact between two subsequent units has deteriorated in response of some mechanisms (e.g. erosional contact etc). Redacted from (Hynek and Di Achille, 2017). The ages for the Noachian sub-periods are given by (Nimmo and Tanaka, 2005), while the age for the Hesperian subperiods are given by (Hartmann, 2005).

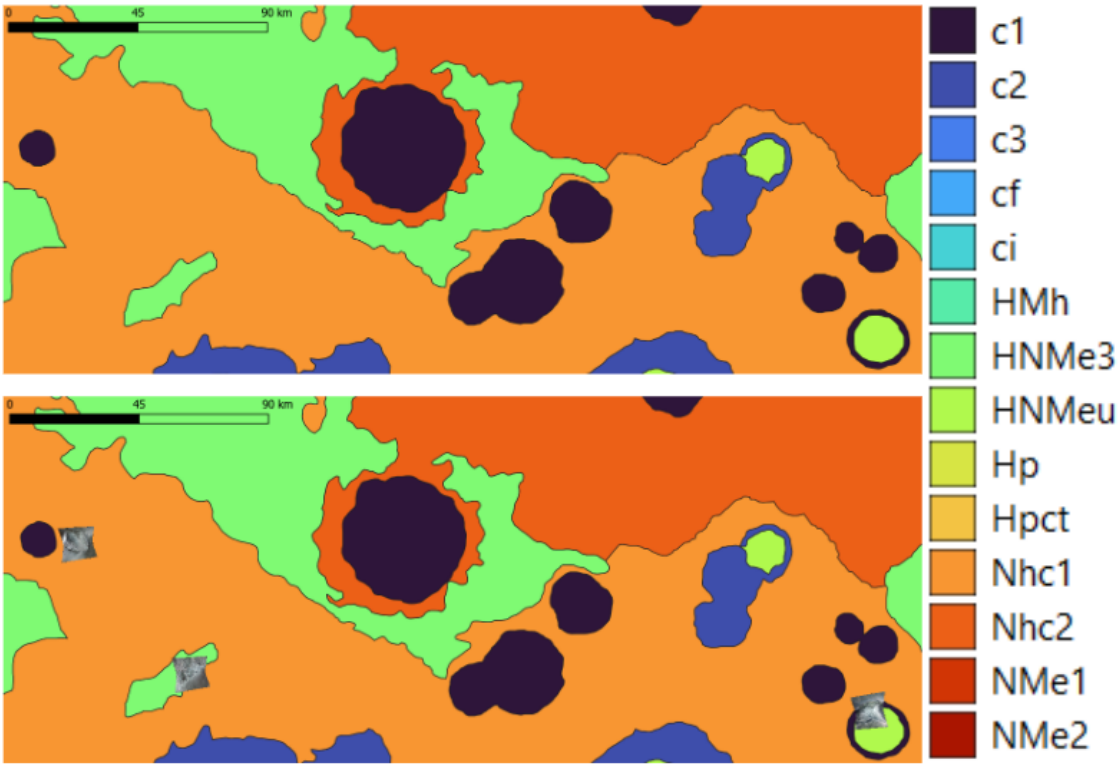

Figure 1.9: Detail pf the geological map of Meridiani Planum over the zone we analyzed (top). Superimposed CRISM false color images showing the target location (bottom). TO see more details about our targets see chapter 2.1.3 .

2

Dataset and Methods

2.1 Instrumentation and Data Characteristics

We used data taken from the Mars Reconnaisance Orbiter (MRO), specifically hyperspectral data from the Compact Reconnaissance Imaging Spectrometer for Mars (CRISM). We selected the following 3 sites with CRISM acquisitions from the database *Mars Orbital Data Explorer* (https://ode.rsl.wustl.edu/mars/): *FRT00009b5a*, *FRT00003e24* and *FRT000062e6*. The prefix FRT stands for *Full Resolution Targeted*, thus meaning that the data we used had the highest resolution avaliable, with 6.55 nm/channel of spectral resolution and ~18.4 m/px of spatial resolution. The first CRISM acquisition (FRT00009b5a) covers the northern part of Kai crater in Meridiani Planum and some of the area outside its rim; the second one (FRT00003e24) was acquired over a small unnamed oblique impact crater northwest of Kozova crater; the last one (FRT000062e6) is centered on some intercrater deposit in Piscinas Serpentes just north from the Kozova crater (for more details see table 2.1 and to see the approximate location see figure 2.1). After downloading the CRISM data we created a custom Python code to:

1. Create RGB maps and stretch them to enhance contrast;
2. Select specific zones from which to extract the spectra;
3. Normalize the selected spectra over 3 different types of neutral spectra;
4. Compare the normalized spectra with CRISM certified spectra from (MICA, 2019) and, when possible, with the laboratory spectra indicated by (MICA, 2019).

Table 2.1: Summary table of targets name, location and typology. λ and φ are, respectively, the longitude and latitude.

CRISM name	λ range [°]	φ range [°]	Description
FRT00009b5a	[2.6960749 , 2.9329382]	[4.3443401 , 4.5699675]	Crater deposits
FRT00003e24	[-1.9589518 , -1.7211730]	[5.3255739 , 5.5390642]	Crater deposits
FRT000062e6	[-1.0625761 , -1.2988321]	[4.5616021 , 4.7762974]	Intercrater deposits

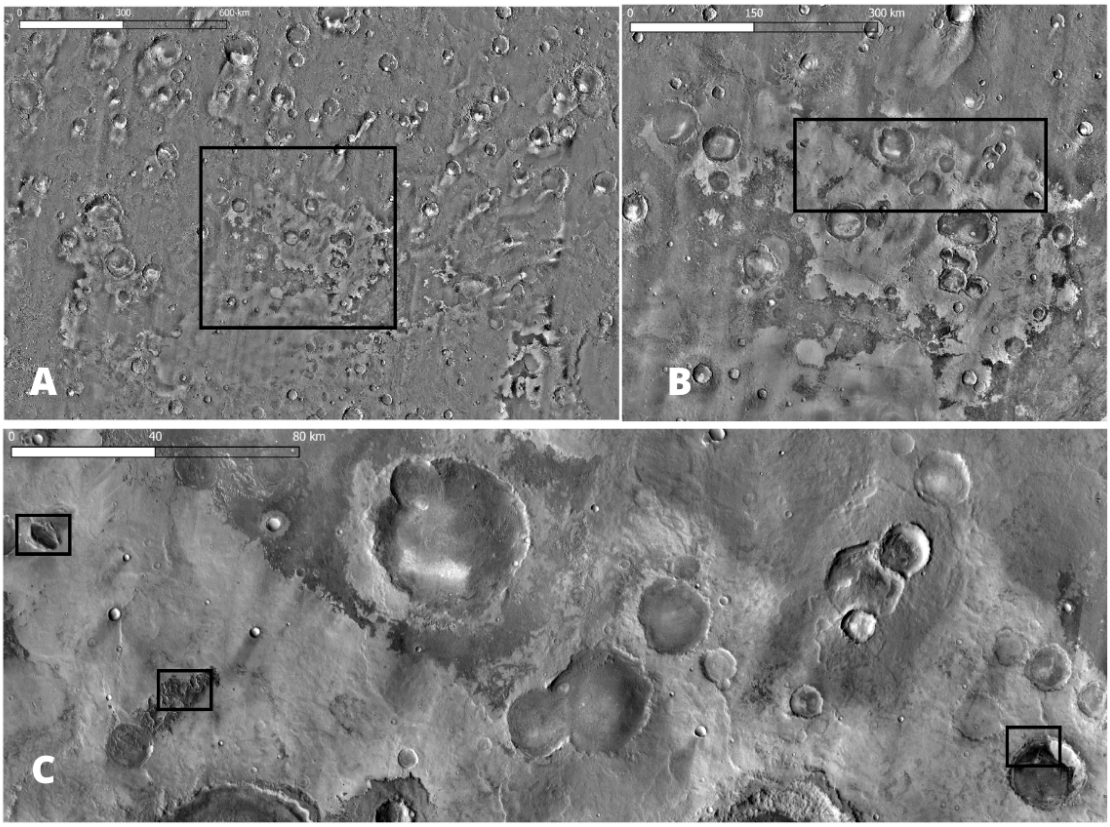

Figure 2.1: Location of our three targets in Meridiani Planum taking the THEMIS/Viking map given by Hynek Di Achille shown globally also in figure 1.5.

2.1.1 Mars Reconnaissance Orbiter

On March 10th 2006 the Mars Reconnaissance Orbiter (MRO) reached the Martian orbit and in November of the same year it began gathering data. Its orbit around Mars is nearly circular and it is inclined by 93°, reaching 255 km distance over the South Pole and 320 km distance over the North Pole. MRO carried along six principal scientific instruments (see table 2.2). During more than 17 years of operations MRO collected more than 456 Tb of data. A schematic view of MRO is presented in figure 2.2.

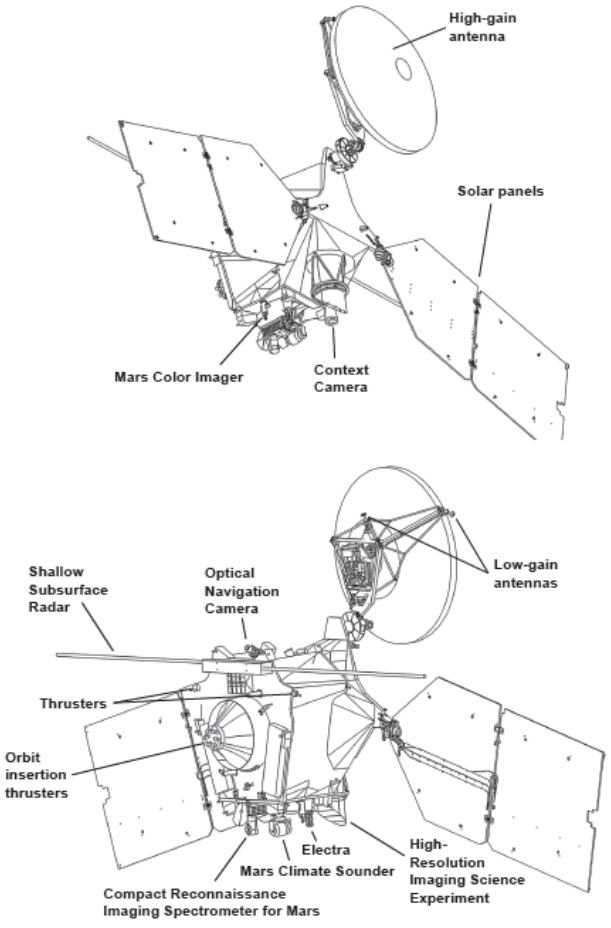

Figure 2.2: Schematic view of the Mars Reconnaissance Orbiter. Credits: MRO Press Kit, 2006

Table 2.2: MRO instruments brief description.

Name	Resolution	Description
HiRISE	0.3m/px from 300km	0.5 m reflecting telescope, collects images in three color bands, 400 to 600 nm (blue–green or B–G), 550 to 850 nm (red) and 800 to 1,000 nm (near infrared or NIR).
CTX	up to 6m/px	Provides grayscale images (500-800 nm) as context maps for HiRISE and CRISM.
MARCI	1-10km/px	Provides global map in five visible and two UV bands giving weekly weather report for Mars, helps to characterize its seasonal and annual variations, and maps the presence of water vapor and ozone in its atmosphere.
CRISM	18m/px from 300km	Visible and near infrared spectrometer that is used to produce detailed maps of the surface mineralogy of Mars. It operates from 362 to 3920 nm, measures the spectrum in 544 channels (each 6.55 nm wide).
MCS	×	Spectrometer with one visible/near infrared channel (0.3 to 3.0 μm) and eight far infrared (12 to 50 μm) channels to quantify the global atmosphere's vertical variations.
SHARAD	max depth 1 km, hor. res. 0.3-3 km/px	Probe the internal structure of the Martian polar ice caps and also gathers planet-wide information about underground layers of ice, rock and possibly liquid water that might be accessible from the surface. It uses HF radio waves between 15 and 25 MHz.

2.1.2 CRISM and MTRDR Data

CRISM is a hyperspectral imager covering a wavelength range from 362 to 3920 nm and with a spectral resolution of 6.55 nm/channel (For a total of 544 channels).
This means that CRISM can observe in both the visible range (380 – 700 nm) and the infrared wavelength range (>700 nm).
Studying the reflected/diffused light coming from the surface of Mars in this range enables CRISM to detect a broad range of minerals on the Martian surface (NASA CRISM Team, 2006), (Murchie et al., 2007).
At visible wavelengths, the way light is reflected is strongly influenced by iron minerals (i.e. rust, or iron oxide, appears red).
At infrared wavelengths, CRISM can then detect features associated with sulfates, carbonates and minerals containing hydroxyl and water such as phyllosilicates (NASA CRISM Team, 2006).
The CRISM instrument is composed of three main units:

- **Optical Sensor Unit (OSU)**: which includes the optics, a gimbal to remove smear due to spacecraft motion, two detectors, one for the visible and one for the infrared, cryocoolers to cool the infrared detectors, radiators to keep the instrument cold, and electronics;
- **Gimbal Motor Electronics (GME)**: which commands and powers the gimbal and analyzes data from its angular position encoder in a feedback loop;
- **Data Processing Unit (DPU)**: which accepts and processes commands from the spacecraft and data from the OSU to communicate it to the spacecraft.

The optics are shown and described in figure 2.3 and are composed by a 100mm Ritchey-Chrétien telescope that focuses the light reflected from the Martian surface onto a slit 27 μm $\times$ 16.3 mm.
The specifics of the instrument are shown in table 2.3.

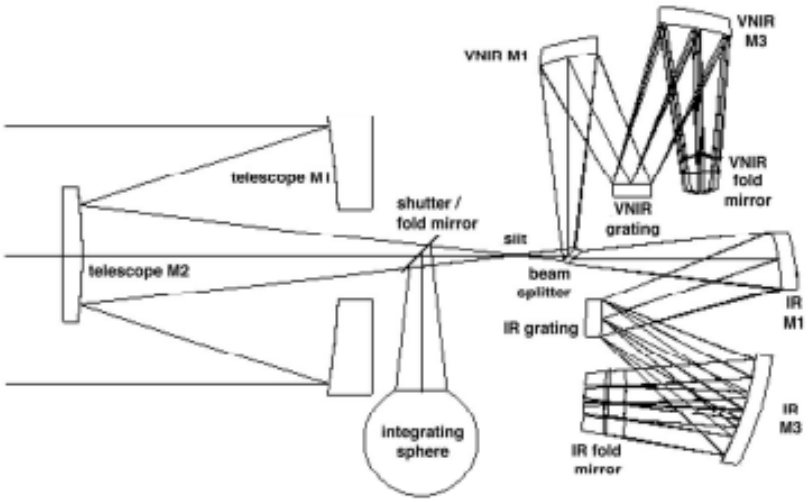

Figure 2.3: CRISM optical diagram. After the slit, the light encounters a wedged ZnSe dichroic beamsplitter and the VNIR light is reflected, while the IR is transmitted. The two beams are then directed to the spectrometers and dispersed by a diffraction grating. The detectors of the spectrometers are an array of Si photodiodes for the VNIR and an array of HgCdTe diodes for the IR. The shutter and the integrating sphere that are placed between the telescope and the slit are for calibration. The integrating sphere is used for in-flight reference for radiometric calibration sampling all the optics without the telescope, while the shutter has three positions: to witch between the light coming from the telescope, the light coming form the integrating sphere and no light.

Table 2.3: CRISM specifics. The swath width and the spatial sampling are given as if the image was taken from 300 km of altitude. The pointing aperture was subject to changes in 2010 and 2012 due to problems with the gimbals, originally the Pointing was between -60 ° and 60 ° (NASA CRISM Team, 2006).

Aperture [mm]	100
FOV [mrad]	37
Spectral Range VNIR [nm]	362-1053
Spectral Range IR [nm]	1002-3920
Swath Width [km]	11.1
Pointing [°]	from -1 to 30
Focal Length [mm]	441
Instantaneous FOV [μrad]	61.5
Spectral Sampling [nm/channel]	6.55
Spatial Sampling [m/px]	18.4

CRISM spectral data present themselves as data cubes (see figure 2.4), in which the x and y dimensions are the spatial dimensions and the z dimension is the spectral one (λ), as if each slice

along the third dimension is a spatial image seen in a specific wavelength interval. The data are firstly taken along the x and λ dimensions, then the y dimensions is obtained by joining all the x-λ frames together in succession. This type of scanning is called *push-and-broom*.
After the data are taken, a calibration is performed on the raw data taking into account the instrument's response and the shutter-closed dark measurement from the scene (bias/flat field measurements). The radiance data (in $\frac{W}{m^2 sr \mu m}$) are then extracted from the raw data. This radiance data are composed by the solar spectrum minus the absorbed component by the surface $I_{surf}(\lambda) = I_{odot}(\lambda) - I_{abs}(\lambda)$. Then the data is normalized by the solar flux (scaled to Mars) assuming the surface to be Lambertian and, finally, the data is corrected for the incidence angle as if the image was observed with the Sun at Nadir. The formula for this photometric correction is:

$$RD = M \left(\frac{\frac{K(D_{14} \cdot D_N - B_{iaT})}{t} - B_{kgd} - S_{cat}}{RST \cdot FF} \right) \tag{2.1}$$

Where:

$$\begin{cases} RD \equiv RD(x, \lambda, r) & \text{Observed spectral radiance at the instrument aperture} \\ M \equiv M(x, \lambda, r, Hz) & \text{Detector mask for bad pixel correction} \\ K \equiv K(x, \lambda, Hz) & \text{Correction for VNIR dark column, initial bad pixels, nonlinearity etc.} \\ D_{14} \equiv D_{14}(\lambda) & \text{Converts from war data to 14-bit} \\ D_N \equiv D_N(x, \lambda, T_{aV}, T_{aW}, T_{aI}, T_{aJ}, T_{a2}, Hz, t, r) & \text{Raw data} \\ B_{iaT} \equiv B_{iaT}(x, \lambda, T_{aV}, T_{aW}, T_{aI}, T_{aJ}, Hz, t) & \text{Detector bias} \\ B_{kgd} \equiv B_{kgd}(x, \lambda, T_{aI}, T_{a2}, Hz, r) & \text{Dark subtraction} \\ RST \equiv RST(x, \lambda, T_{aV}, T_{aI}, T_{a2}) & \text{Responsivity as computed from the calibration images} \\ FF \equiv FF(x, \lambda, Hz) & \text{Flat Field} \end{cases}$$

Where x is the spatial position in a row of the focal plane, λ [nm] is the wavelength, Hz is the frame rate, T_{aI} [K] is the temperature of the IR detector, T_{aV} [K] is the temperature of the VNIR detector, T_{a2} [K] is the spectrometer housing temperature, T_{aJ} [K] is the temperature of the focal plane board in IR, T_{aW} [K] is is the temperature of the focal plane board in VNIR, t [s]is the integration time and r is the distance [AU] of Mars from the Sun.

From the radiometric calibration the diffuse spectral reflectivity (I/F) is calculated using:

$$IF(x, y) = \pi r^2 \cdot \frac{RD(x, \lambda, r)}{SF(x, \lambda)} \tag{2.2}$$

Where SF is the solar spectral irradiance for a normally illuminated surface at 1 AU from the Sun.

There are several types of final products from CRISM. We used the most advanced one, called MTRDRs (Map-Projected Target Reduced Data Records). The MTRDR images are hyperspectral that covers the entire range of CRISM's wavelength (362 to 3920 nm) from which the so called "bad bands" were removed (these bad bands were columns, i.e. y-axis slices, in which noise were present in the majority of the pixels composing the column), and, in general, the quality of the images were enhanced by removing bad pixels.

From all the data types provided by the MTRDR format we used the hyperspectral cube in units of corrected I/F (marked with an "IF" in the file name and calculated from the raw data using equations 2.1 and 2.2), and the refined spectral summary parameter cube (marked with an "SR") which are noise-mitigated versions of the spectral summary parameters (see chapter 2.2). Finally, Projected MTRDR are products where, the longitude and latitude information of each pixel is recorded, allowing to locate their position on the Martian surface. The projected data have an hourglass-like shape due to the changing range of the spacecraft with respect to the target during the image acquisition.

Other than CRISM data, we also used the High Resolution Imaging Science Experiment (HiRISE) images for high resolution morphology and the Context Camera (CTX) images to provide contextual information.

Lastly, regarding the spectra that will be extracted from the CRISM dataset, it is important to remember some limits of the CRISM instrument:

- The bands between ~1650 nm and ~1750 nm have an artefact due to overlapping of two filters;
- The bands between ~1900 nm and ~2050 nm, and between ~2600 nm and ~2800 nm have artefacts due to a residual of atmospheric CO_2 absorption;
- The final bands, from ~3000 nm to the sensor wavelength limit, have a lower signal-to-noise ratio (SNR). SNR usually exceeds 400 at key wavelengths such as 2300 nm, but it is only around 100 at >2700 nm due to the less reflected light at that wavelength. Moreover, the presence of Mars' black body radiation affects measurements at >3000 nm.

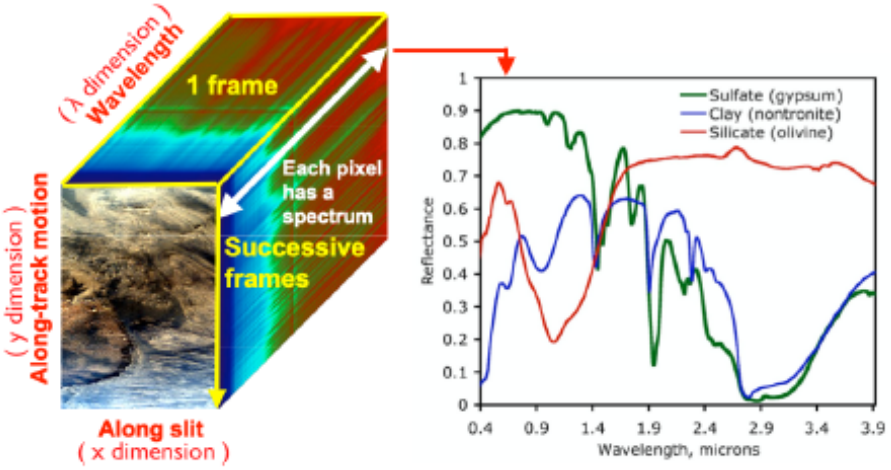

Figure 2.4: Example of a data cube. On the left a schematic visualization with x-y spatial dimension and z spectral dimension and, on the right, a view of the spectra extracted from a slice. Credits:

2.1.3 Target Selection

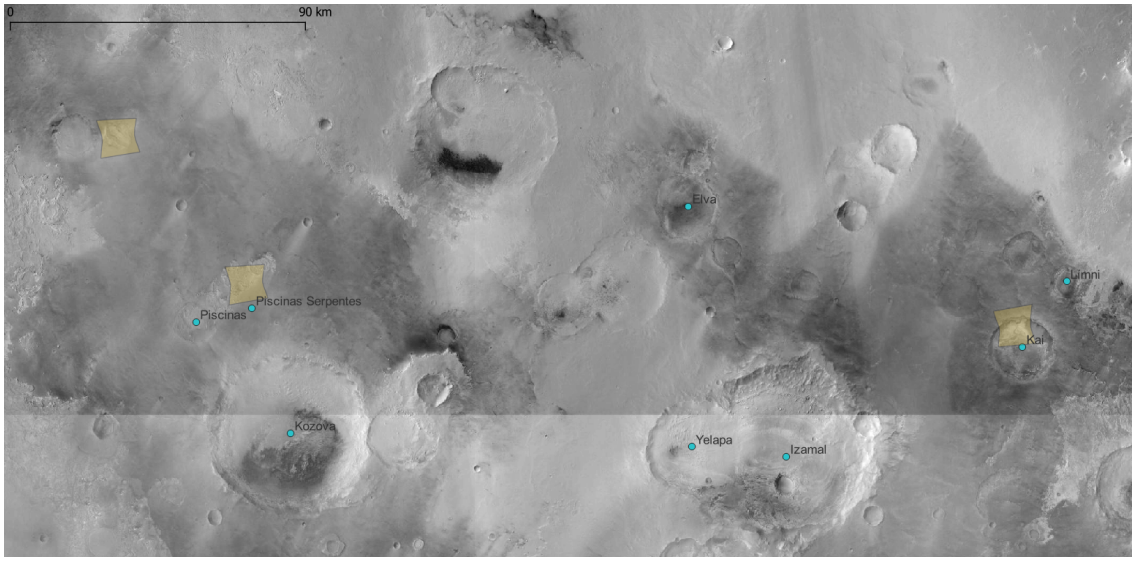

Figure 2.5: CTX mosaic of the studied region in Meridiani Planum. The three yellowish hourglass shaped polygons are the three ROI we selected. The leftmost one is FRT00003e24, then there is FRT000062e6 and the rightmost one is FRT00009b5a. The North is in the upward direction. Credits of CTX Mosaic: Murray Lab.

As stated before, this work focuses on the analysis of three CRISM data cubes located in the Northern portion of Meridiani Planum (see figure 2.5 and table 2.1). The three data cubes

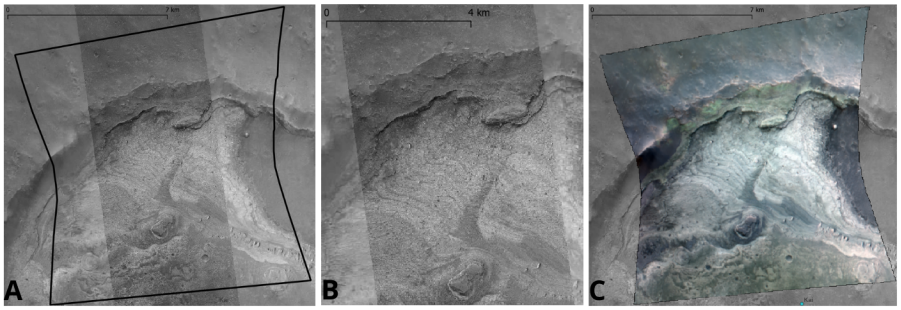

Figure 2.6: Detail of the cube located in the Kai crater. The North is in the upward direction. **A** contains the outline of the MTRDR image including the high resolution HiRISE image and the lower resolution CTX image. **B** contains a detail of the HiRISE image. **C** contains our stretched false color image.

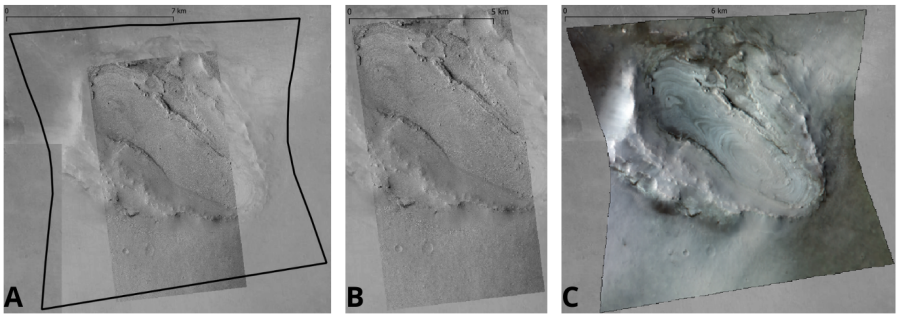

Figure 2.7: Detail of the cube located in the unnamed crater northwest of Piscinas Serpentes. The North is in the upward direction. **A** contains the outline of the MTRDR image including the high resolution HiRISE image and the lower resolution CTX image. **B** contains a detail of the HiRISE image. **C** contains our stretched false color image.

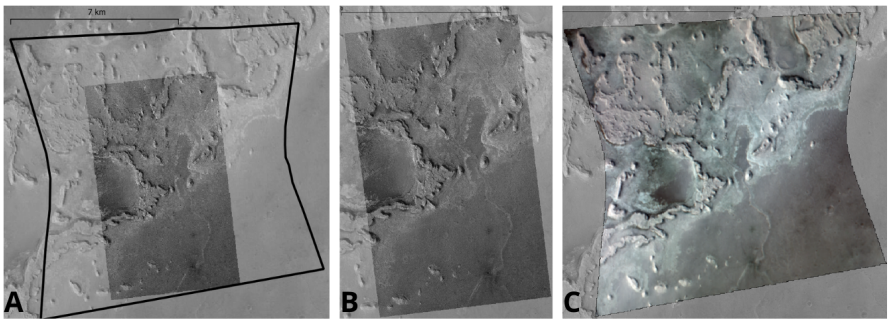

Figure 2.8: Detail of the cube located slightly north of Piscinas Serpentes. The North is in the upward direction. **A** contains the outline of the MTRDR image including the high resolution HiRISE image and the lower resolution CTX image. **B** contains a detail of the HiRISE image. **C** contains our stretched false color image.

cover areas where complex sedimentary structures and hydrated materials are observed. Their detailed studies can provide important information on the environment in which the sediment formed and on the aqueous history of the area.

Regarding the selection of the cubes, we have chosen FRT00009b5a due to fact that it presents lots of distinguishable features (see figure 2.6) and, moreover, Kai it is also an already known crater (Baschetti et al., 2022) and so it was chosen also to see if our code (see chapter 2.3) was a feasible method to analyze CRISM data cubes.
The cube named FRT000003e24 was chosen for its peculiar morphological features such as the oblique impact structure and the layered sediments on the crater floor, which are similar to the ones observed in Kai crater (see figure 2.7). Finally, we selected the last cube (FRT000062e6, see figure 2.8), as it represents a portion of Meridiani Planum sediment which was not deposited on a crater floor. Analyzing this area can provide information on a geological context which is distinct from the crater deposits, enriching the breadth of our analysis and interpretation.

2.2 Introduction to Remote Sensing and Reflectance Spectroscopy

Reflectance spectroscopy is a type of spectroscopy that relies on the possibility of detecting the presence of substances using light that comes from another source (i.e. the Sun) being reflected from an opaque surface. The detection of a given material depends on the absorptions occurring at specific wavelengths of its reflectance spectrum. Contrary to the spectroscopy of gases, reflectance spectroscopy does not permit the characterization of the quantity (mass) of the material, but only its presence on the studied surface.
The main spectral features from primary and secondary minerals such as mafic minerals, clays, sulfates and carbonates come from electronic and vibrational processes detectable in the wavelength of visible to short wave infrared (from $\sim$1000 to $\sim$2600 nm). Those processes, and thus the spectral feature they give, are the results of energy changes in the atoms and molecules that compose the surface (Clark, 1999).
A process can be electronic when the electrons of an atom or molecule change its energy state also changing orbital. In mineral spectroscopy this type of process is typically related to crystals, in which the degeneracy of d-type orbitals can break, splitting so the orbital in different energy states, thus enabling an electron to move from lower to higher levels if a photon of adequate energy is absorbed (as states the Planck relation $E = \frac{hc}{\lambda}$). The splitting happens differently for different matches of transition elements and ligands, thus making the electronic transitions of crystals a successfully useful tool in mineral identification. This process is also called *crystal field effect*. Another common process that involve electronic transition is the so-called *charge*

transfer absorption, in which the absorption of a photon can cause an electron to be exchanged in a ion-ion, ion-ligand or ligand-ligand way.
On the other hand, emission and absorption resulting from vibrational transitions are related to the vibration of the molecules inside the crystals. The quantity of possible movements, and so the number of spectral traces of a molecule, depends from the number of atoms composing the molecule and if the molecule is linear or nonlinear. So if n is the number of modes and N is the number of atoms:

$$\begin{cases} n = 3N - 5 & \text{If the molecule is linear} \\ n = 3N - 6 & \text{If the molecule is nonlinear} \end{cases} \tag{2.3}$$

The 3N component arises from the number of degrees of freedom of the molecule, either translational (around the center of mass), rotational and vibrational. While the second term derives from the fact that, from the total number of degrees of freedom, translational and rotational degrees of freedom of the molecule must be adjusted in order to take into account only the vibrational ones. In particular all molecules have 3 translational degrees of freedom but the nonlinear molecules have 3 rotational degrees of freedom (making a total of 6 degrees of freedom to subtract from the total), whereas the linear ones have only two rotational degrees of freedom given that the rotation around the molecular axis does not involve movement of the nuclei (making a total of 5 degrees of freedom to subtract from the total). The frequencies of vibration modes depends on the strength of the bond between atoms in the molecule and the mass of each different atom (the atomic number A) and they show off only if the absorbing/emitting molecule has a dipole moment.
Moreover, each vibration can occur at the integer multiples of the original fundamentals and at combinations of different fundamentals (overtones and combinations), for example, if a molecule posses 3 fundamentals (usually noted with the greek letter ν):

$$\begin{cases} \text{Overtones} \longrightarrow a\nu_1, b\nu_2, c\nu_3 \\ \text{Combinations} \longrightarrow \nu_1 + \nu_2, \nu_1 + \nu_3, \nu_2 + \nu_3, \nu_1 + \nu_2 + \nu_3 \end{cases} \tag{2.4}$$

Typically, electronic and vibrational transitions are found in, respectively, visible and infrared light domains.
As stated before, we used two types of the MTRDR CRISM products, the cubes containing the spectras and the cubes containing the spectral parameters. The spectral parameters can be

used in the creation of mineral maps, highlighting different mineralogic compositions with different colors. This is an effective way to highlight spectral features, given that we adjust the contrast of the image by correctly *stretching* the parameters.
CRISM's spectral parameters are of various types, principally slopes, reflectances and band depths, but it is this last one that is most commonly used. Each spectral parameter focuses on characterising a specific feature of the spectrum. Band depths are calculated projecting the deepest point(s) of an absorption feature vertically onto the extrapolated continuum, calculating then the difference between the depth value and the projected point. Usually bands are asymmetric with respect to the continuum, and to better compute the spectral parameter, two supplementary values a and b are extracted and used in the calculation of the parameters (see equations from 2.6 to 2.9) (Viviano-Beck et al., 2014):

$$\begin{cases} b = \frac{\lambda_C - \lambda_S}{\lambda_L - \lambda_S} \\ a = 1 - b \end{cases} \tag{2.5}$$

Band depths parameters can be of four types (Viviano-Beck et al., 2014) (see figure 2.9):

- **Band Depth Parameter (BD)**, see figure 2.9 A for variable's names: a single absorption band that occurs at a λ_C value. Band Depths Parameters are expressed as follows (Viviano-Beck et al., 2014):

$$BD(\lambda_C) = 1 - \frac{R_C}{R_{C*}} = 1 - \frac{R_C}{aR_S + bR_L} \tag{2.6}$$

- **Inverse Band Depth Parameter (BH)**, see figure 2.9 B for variable's names: not a literary inverted band, but, instead of using the depth of the band, the height of an inflection (with respect to the continuum) is derived to define the spectral parameter. The inverse band depth is used when absorption features overlap in the characteristic spectrum (Viviano-Beck et al., 2014):

$$BH(\lambda_C) = 1 - \frac{R_{C*}}{R_C} = 1 - \frac{aR_S + bR_L}{R_C} \tag{2.7}$$

- **Doublet/Two-Band Parameter (MIN)**, see figure 2.9 A and 2.9 C for variable's names: used when a spectral feature contains a doublet or when two absorptions must be present to characterize thespectrum. In this case we must combine the information from both band depths (Viviano-Beck et al., 2014) using a minimum calculation:

$$MIN(BD(\lambda_{C1}), BD(\lambda_{C2})) = min[BD(\lambda_{C1}), BD(\lambda_{C2})] \tag{2.8}$$

- **Broad Band Parameter (BD)**, see figure 2.9 A and 2.9 D for variable's names: some spectra show broad absorption bands spanning multiple CRISM wavelengths. To calculate the corresponding spectral parameter a weighted average is computed (Viviano-Beck et al., 2014):

$$BD(\lambda_{C1-CN}) = \sum_{i=1}^{N} d_i(BD(\lambda_{Ci})) \tag{2.9}$$

  Where D_i represents a weighting coefficient that may vary for each band depth and are determined empirically.

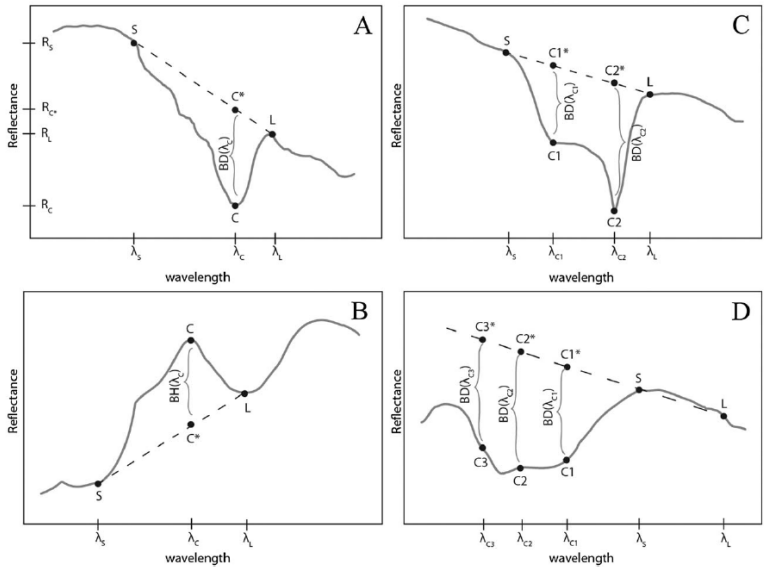

Figure 2.9: Examples of band depth types. **A** represents a Band Depth Parameter , **B** represents an Inverse Band Depth Parameter, **C** represents a Doublet/Two-Band Parameter and **D** represents a Broad Band Parameter. The solid lines are the hypothetical spectras while the dashed lines are the inferred continuums. Credits: (Viviano-Beck et al., 2014)

In CRISM spectral parameters some band width parameters are called INDEX, these parameters are specific types of band depth that represent typical spectral traces of some minerals (i.e. OLINDEX3 detects the spectral feature associated with the presence of olivine). Other types of parameters include the ones indicates with *R* that represent reflectance values, the *BDI*, or Integrated Band Depth, that are integration of band depth over a discrete interval (for example, to avoid specific wavelength associated with other absorption features), the *SLOPE* parameter that marks a specific slope of the spectrum associated with a mineral, the *DOUB* that is analogues to the MIN parameter, the *D* parameters that indicates a sudden drop in the spectrum, the *SH* that are the so-called shoulder heights parameters, the *IR* that indicates reflectance ra-

tios and, finally, the *ICER* parameters that represents specific spectral features related to H_2O or CO_2 ices. In this work we did not used all parameters types since we produced only some RGB maps (see tables 2.4 and 2.5).
In particular we produced 7 types of mineral maps for each CRISM cube combining three different spectral parameters in a RGB image, where each color channel is associated to a parameter (see tables 2.4 and 2.5). It is important to correctly stretch the spectral parameters in order to highlight significant mineral detections. The images are stretched by visualizing an histogram of each channel and adjusting the range of values of each spectral parameter from a minimum threshold (detection limit) to a maximum threshold (upper limit).
The detection limit and upper limit are adjusted following the following empirical rules (Viviano-Beck et al., 2014) set for non cumulative hisotgrams:

- If the spectral parameters are pure reflectances or SH600_2 and ISLOPE1, it is sufficient to stretch between the 0.1th and 99.9th percentiles;
- For all the other spectral parameters we have two subcases:
  - If the maximum of the histogram is greater than 0, then the stretch is done between the maximum and the 99.9th percentile;
  - If the maximum of the histogram is less than 0, then the stretch is done between 0 and the 99.9th percentile.

Lastly, we used only standard RGB maps. These maps are composed by spectral parameters correlated with specific mineralogies (Viviano-Beck et al., 2014). In our work we used the standard RGB maps shown in table 2.6 composed by the spectral parameters described in table 3.3. As a last note, since we were searching for hydrated minerals, we selected a range between 1000 nm and 2600 nm as wavelength range in which our analysis was conducted. This range contains the major absorptions of most families of hydrated minerals such as sulfates and clays.

Table 2.4: RGB maps we produced with the corresponding spectral parameters and description (Viviano-Beck et al., 2014)

Map	Red	Green	Blue	Description
FAL	R2529	R1506	R1080	An enhanced infrared false color representation of the scene.
MAF	OLINDEX3	LCPINDEX2	HCPINDEX2	Olivine will appear red in the MAF browse product. Low and high-Ca pyroxene appear green/cyan and blue/ magenta, respectively.
HYD	SINDEX2	BD2100_2	BD1900_2	Polyhydrated sulfates appear magenta, monohydrated sulfates appear yellow/green, blue colors are indicative of other hydrated minerals
PHY	D2300	D2200	BD1900r2	Fe/ Mg-OH bearing minerals will appear red, or magenta when hydrated. Al/ Si-OH bearing minerals will appear green, or cyan when hydrated. Blue colors are indicative of other hydrated minerals.
PFM	BD2355	D2300	BD2290	Red/yellow colors indicate the presence of prehnite, chlorite, epidote, or Ca/Fe carbonate, while cyan colors indicate the presence of Fe/Mg smectites or Mg carbonate.
HYS	MIN2250	BD2250	BD1900r2	Light red/yellow colors indicate the presence of hydrated silica, whereas cyan colors indicate Al-OH minerals. Additionally, jarosite will appear yellow. Blue colors are indicative of other hydrated minerals.
FM2	BD530_2	BD920_2	BDI1000VIS	Red colors indicate the presence of nanophase ferric oxides, green colors suggest coarser-grained Fe minerals (particularly low-Ca pyroxene), and blue colors are often dust-free or more mafic surfaces.

Table 2.5: Description of the spectral parameters used in RGB maps. For completeness: $RB\# = \frac{RC\#-R\#}{RC\#}$, where RC denotes the value of point at a wavelength of # nm along a modeled line that follows the average slope of the spectrum (Viviano-Beck et al., 2014). The # symbol indicate a generic value of a wavelength.

Parameter	Wavelength [nm]	Formula
R2529	2529	$R2529$
R1506	1506	$R1506$
R1080	1080	$R1080$
OLINDEX3	Broad at 1000	$0.1RB1210 + 0.1RB1250 + 0.2RB1263 + 0.2RB1276 + 0.4RB1330$
LCPINDEX2	Broad at 1810	$0.2RB1690 + 0.2RB1750 + 0.3RB1810 + 0.3RB1870$
HCPINDEX2	Broad at 2120	$0.1RB2120 + 0.1RB2140 + 0.15RB2230 + 0.3RB2250 + 0.2RB2430 + 0.15RB2460$
SINDEX2	Convexity at 2290	$1 - \left(\frac{a \cdot R2120 + b \cdot R2400}{R2290}\right)$
BD2100_2	2100	$1 - \left(\frac{R2123}{a \cdot R1930 + b \cdot R2250}\right)$
BD1900_2	1900	$\frac{1}{2}\left[1 - \left(\frac{R1930}{a \cdot R1850 + b \cdot R2067}\right)\right] + \frac{1}{2}\left[1 - \left(\frac{R1985}{a \cdot R1850 + b \cdot R2067}\right)\right]$
D2300	Dropoff at 2300	$1 - \left(\frac{\frac{R2290}{RC2290} + \frac{R2320}{RC2320} + \frac{R2330}{RC2330}}{\frac{R2120}{RC2120} + \frac{R2170}{RC2170} + \frac{R2210}{RC2210}}\right)$
D2200	Dropoff at 2200	$1 - \left(\frac{\frac{R2210}{RC2210} + \frac{R2230}{RC2230}}{2\frac{R2165}{RC2165}}\right)$
BD1900r2	1900	$1 - \left(\frac{\frac{R1908}{RC1908} + \frac{R1914}{RC1914} + \frac{R1921}{RC1921} + \frac{R1928}{RC1928} + \frac{R1934}{RC1934} + \frac{R1941}{RC1941}}{\frac{R1862}{RC1862} + \frac{R1869}{RC1869} + \frac{R1875}{RC1875} + \frac{R2112}{RC2112} + \frac{R2120}{RC2120} + \frac{R2126}{RC2126}}\right)$
BD2355	2355	$1 - \left(\frac{R2355}{a \cdot R2300 + b \cdot R2450}\right)$
BD2290	2292 and 2300	$1 - \left(\frac{R2290}{a \cdot R2250 + b \cdot R2350}\right)$
MIN2250	min 2210 and 2260	$min\left[1 - \left(\frac{R2210}{a \cdot R2165 + b \cdot R2350}\right), 1 - \left(\frac{R2265}{a \cdot R2165 + b \cdot R2350}\right)\right]$
BD2250	Broad 2250	$1 - \left(\frac{R2245}{a \cdot R2120 + b \cdot R2340}\right)$
BD530_2	530	$1 - \left(\frac{R530}{a \cdot R614 + b \cdot R440}\right)$
BD920_2	920	$1 - \left(\frac{R920}{a \cdot R807 + b \cdot R984}\right)$
BDI1000VIS	Integrated from VNIR at 1000	$\int_{R833}^{R1023}\left(1 - \frac{R}{RPEAK1}\right) dR$

Other than RGB maps it is possible to generate a lot of other maps, such as single color maps

(we used this in one case, for the phyllosilicates analysis of FRT00009B5A). These maps take only one spectral parameter as input , showing the distribution of its values with a color map of your choice. It is then possible to stretch the parameter between a lower and upper level of choice, with a process analogue to the one used for the RGBs.
After the RGB maps, the spectra of targeted regions of interest (ROI) can be extracted by taking the mean of all the spectras that corresponds to the selected ROI and then normalize it by a neutral spectra (see chapter 2.3.2) to enhance the spectral features. Finally after having the normalized spectra the mineral identification can be done by comparing the absorptions of the extracted spectra with laboratory spectra of known minerals or with CRISM spectra of certified detections, such as those in (Viviano-Beck et al., 2014).

2.3 Python

2.3.1 Python vs. propietary softwares

Classically, the analysis of CRISM data cubes is done using the IDL programming language and the software ENVI®. These programs are not free and require the user to buy a license to work with them. This hugely limits the possibility of use, especially from users with limited means.
To try to provide a free and open source alternative to the community we developed a pipeline using only Python, with some functions similar to the one available in IDL and/or ENVI®.
Another main advantage of Python over the classical IDL/ENVI® is that it is best suited for general programming purposes, it is easy to implement in other pipelines and is not difficult to expand the code at user will also with other packages and modules.
One of the main disadvantage regarding the choice of Python is the lack of a pure graphical interface, however, this can and possibly will be resolved in the near future by creating a Python-based dashboard using our code as a part of its back-end using the Panel Python module.

2.3.2 General Code Overview

RGB Map generation

To generate the RGB maps we developed a widget containing the three frequency (or, if needed, cumulative) histograms, one for each RGB channel, on top of which 6 sliders are set at groups of two: one for the maximum stretch value and one for the minimum stretch value. The fi-

nal RGB image with the legend as given by (Viviano-Beck et al., 2014) is shown, along with the percentiles values of the channels' histograms. Finally, it is possible to change between the generated RGB map and a true color or a false color image of the scene, which provides information about surface morphology.
By moving the sliders, the user is able to visualize the maximum and minimum stretch values, which are shown at the end of each slider. The stretch values are also visible on the histograms (vertical red bars) and the percentile values are shown left to the histograms. The RGB image updates accordingly to the stretch. When the desired result is obtained, by closing the widget the final RGB map is saved to memory, as well as the last values of the given stretches. An example of the widget interface is shown in figure 3.5.
Lastly, the generated RGB map can be saved as a .tiff image and then georeferenced to use it in ArcGis or QGis environments.

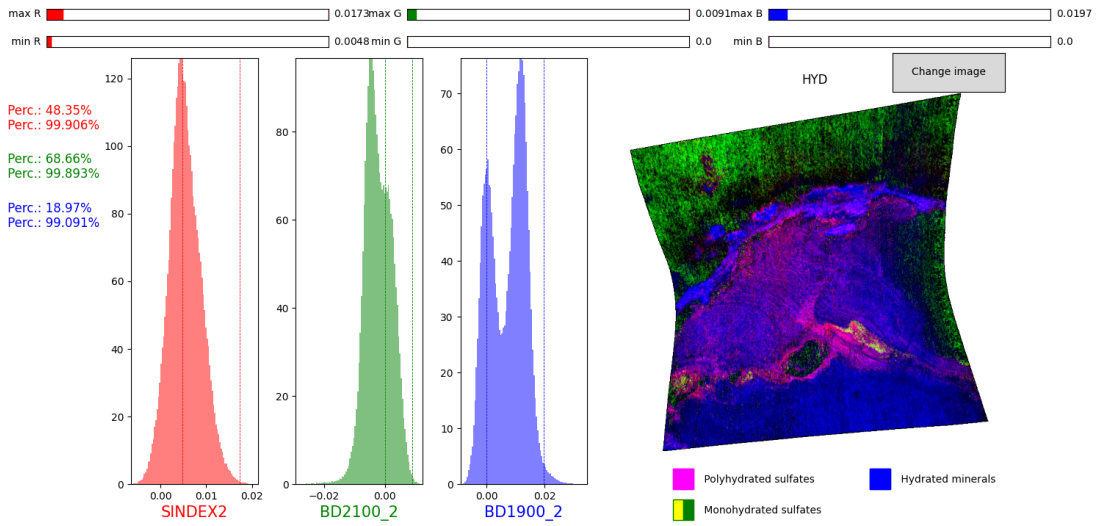

Figure 2.10: Example of the widget interface. In this case made with the spectral parameters needed to produce an hydrated minerals RGB map (HYD).

Spectra Selection

To select the target spectra we implemented three different methods:

- **Point Method**: with this it is possible to select a given number of points on the RGB map, then save the pixels' coordinates, and subsequently extract the spectra of the corresponding pixels from the I/F cube;

- **Square Method**: with this it is possible to select a point, which will be the center of a box with a given side length on the RGB map. It saves the coordinate of each pixels inside the square to subsequently extract the spectra from the corresponding pixels from the IF cube;
- **Polygon Method**: with this it is possible to manually draw a polygon on the RGB map to, again, save the enclosed pixels' coordinates and extract the spectra from the corresponding pixels on the IF cube. The polygon will close automatically upon reaching a set distance from the first drawn point. For this method we also implemented the possibility to see the color legend as given by (Viviano-Beck et al., 2014).

In this work we only used the Polygon Method, for which an example of the drawing interface is presented in figure **??**. Finally, for each method, it is possible to take either the mean or the median of all the spectra, calculating also the respective standard deviation or median absolute deviation.

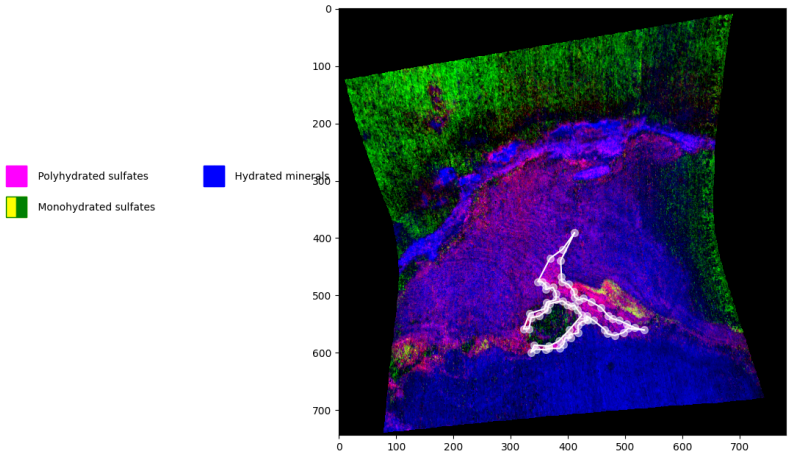

Figure 2.11: Example of the drawing interface of the Polygon Method. In this example we used the HYD RGB map of FRT00009b5a.

Selection of neutral spectra: three methods

To better visualize the spectral features it is needed to normalize the mean spectrum of the target with a neutral spectrum that does not contain any (or minimal) spectral features (see figure 2.12).

To extract the neutral spectra we used three different methods:

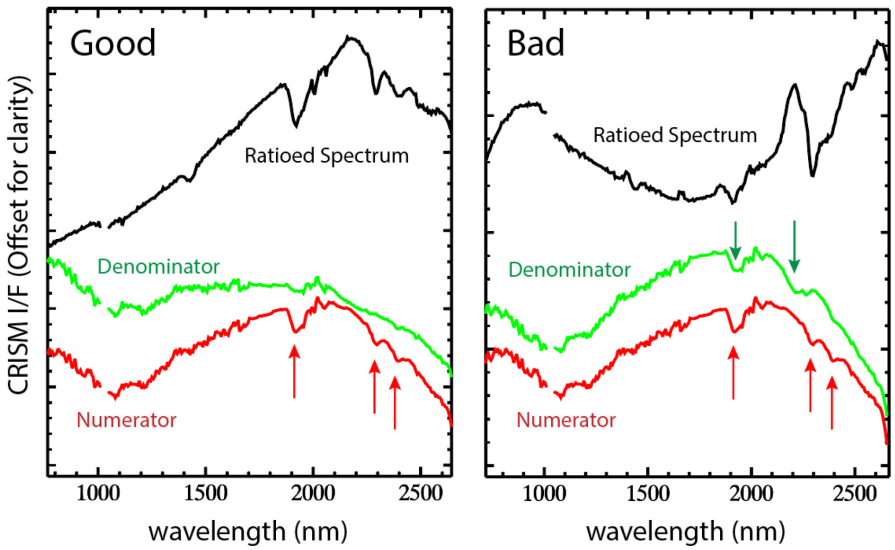

Figure 2.12: Example of ratioed CRISM spectra. On the left a relatively spectrally-neutral denominator in the wavelength range pertaining to the narrower absorption bands (red arrows). On the right a denominator with narrow spectral features (green arrows) that are injected into the resulting ratioed spectrum, which could result in an incorrect interpretation. Credits: (MICA, 2019)

- **Polygon Method**: since CRISM can have column-dependent noise, a method to select the neutral spectrum is to choose an area as it follows:

  1. The zone must be spectrally neutral, meaning that it appears dark in *all* the RGB maps. If the scene doesn't have areas which meet this requirement, ratioing with mafic areas can also provide a good spectral enhancement as the broad absorptions of mafic minerals do not affect much the shape of smaller absorptions such as those of the hydrated minerals;
  2. The zone must have almost all pixels taken inside the same column of the ROI from which the spectra of interest are extracted. If working with the MTRDR cubes the curvature of the hourglass shape must me taken into account.;
  3. To mitigate the noise of the ratioed spectrum, the number of neutral spectra extracted must be at least of the same order of magnitude of the spectra selected from the ROI, but better if greater;
  4. The closer the area from which the neutral spectra is to the ROI the better;
  5. It is best to avoid selecting the neutral spectra near the border of the image.

- **All-map Method**: since MTRDR cubes are refined data cubes with less column noise than their predecessors, a method of extracting the neutral spectrum can be devised by

selecting a set of the selected RGB maps (In our case MAF, HYD, PHY, PFM and HYS) and then extract the spectras from pixels that are dark (i.e. have close to zero value for each RGB channel) in each map.

- **Mineral Mask Method**: this method is similar to the All-map but, instead to select zeroed out pixels around the map, it works by selecting a set of spectral parameters and a threshold value for each of them and for each pixel the Mineral Mask Method evaluates if it has values conforming to the following:

$$\begin{cases} \text{If reflectance:} \begin{cases} R\ldots \geqslant threshold \implies \text{pixel in mineral mask} \\ R\ldots \leqslant threshold \implies \text{pixel outside mineral mask} \end{cases} \\ \\ \text{If other:} \begin{cases} BD\ldots \leqslant threshold \implies \text{pixel in mineral mask} \\ BD\ldots \geqslant threshold \implies \text{pixel outside mineral mask} \end{cases} \end{cases} \tag{2.10}$$

  The main objective of the mineral mask is to collect all pixels that show no major absorption bands due to primary and secondary minerals (Horgan et al., 2020) and then to take the median of all the spectra in those pixels to obtain the neutral spectra.
  This method was inspired by the work of (Horgan et al., 2020).

Spectra Ratioing and Spectra Comparison

Lastly, the spectra ratioing is performed, with consequent final error from error propagation formula:

$$\begin{cases} Ratio = \frac{A}{B} \\ \sigma_{Ratio} = \sqrt{\left(\frac{\sigma_A}{B}\right)^2 + \left(\frac{A\sigma_B}{B^2}\right)^2 - 2\frac{A}{B^3}C_{A,B}} \end{cases} \tag{2.11}$$

Where A is the target mean spectrum, B is the neutral median spectrum, σ_A is the standard deviation of the target mean spectrum, σ_B is the median absolute deviation of the neutral median spectrum and $C_{A,B}$ is the covariance of the two spectra.
The final comparison with known spectra is done by overlying the final spectra to certified CRISM spectra (meaning CRISM spectra from the CRISM spectra library) and, if present, the laboratory spectra.
To do so we created a .csv file (see table 2.6) containing the certified CRISM spectra and the laboratory spectra from various sources and other details as listed by the MICA files (MICA, 2019). The comparison is done with a smoothed version of the spectra to flatten out the noise.

For the smoothing we used the Savitzky-Golay filter (Savitzky and Golay, 1964) which has the property of increasing data precision without distorting the data trend. The filter works like a convolution by fitting successive subsets of points of given length with a low-degree polynomial using linear least square method:

$$Y_j = \sum_{i=\frac{1-m}{2}}^{\frac{m-1}{2}} C_i \cdot y_{j+i} \tag{2.12}$$

Where Y_j is the point on the smoothed curve, m is the polynomial order, n the number of points in the subsets and C_i is the convolution coefficient as given by tabulated values. The pedix j obeys:

$$\frac{m+1}{2} \leqslant j \leqslant n + \frac{1-m}{2} \tag{2.13}$$

To implement the filter we just used the relate Python's Scipy function named *savgol_filter*.

Table 2.6: Example extracted from the .csv file we created for the comparison phase. The bold entries are the voices of the file while the non bold entries are posed as example. The first entry gives the name of the mineral, the second the type of mineral as from (MICA, 2019), the third gives the given name of the file in which the certified CRISM spectra is stored, the fourth is the same as the third but for the laboratory spectra, the fifth is the CRISM cube from which the certified spectra is extracted, the sixth is the type of mineral used in the laboratory analysis, the seventh is the name of the library from which we have taken the laboratory spectra as given on (MICA, 2019), the eighth is the code associated with the particular laboratory spectra as given on (MICA, 2019), the ninth is again the name of the library for the laboratory spectra and is different from the sixth if there is a change between the website name and the name reported on (MICA, 2019), the tenth are the marked absorptions of the certified CRISM spectra as given by (MICA, 2019), the eleventh is the same as the tenth but for laboratory spectra and the twelfth is the grain size used in the laboratory analysis.

Mineral Name	**Mineral Type**
Fe Olivine	Nesosilicate
txt name CRISM	**txt name LAB**
crism_spec_fe_olivine.txt	fe_olivine_LAB.txt
CRISM spectra cube	**Lab. Mineral**
FRT00003e12	Fayalite
Type of Lab. from MICA	**MICA Lab. Code**
RELAB	LAO05
Type fo Lab. from website	**Notable Absorptions CRISM [nm]**
GEO	850,1120,1300
Notable Absorptions LAB [nm]	**Sample Grain Size [μm]**
900,1080,1300	max 4

3 Results

3.1 Results of the Spectral Analysis

Here we present the results of our spectral analysis for each spectral cube.
We have found that the best neutral spectra in almost all cases are given by the polygon method (see figure 3.1), probably because the all-map method selects pixels covering mineralogies that are too different to represent a good base for a median neutral spectra thus resulting in a too noisy normalized spectra and, moreover, in some cases it selects a number of pixels that is too low. The mineral mask method performs better than the all-map method, but in this case the possible problems regard either the choice of threshold values and/or spectral parameters or the fact that some areas covered by the mask may be included in our ROIs. In either cases the result is a noisy spectra, although less than the one obtained with the all-map. In the majority of cases, anyway, the major part of the spectral features is still well identifiable, just not as well as with the normalized spectra obtained with the polygon method. A problem related to both the all-map and the mineral mask methods regards the column dependant noise: both methods select pixels algorithmically from different areas of the image and then compute a median value, which is used as neutral spectrum. This also takes any column dependent noise in the selected spectra and averages it, creating artefacts in the radioed spectrum. This is particularly visible around 1900 nm.
To identify our resulting smoothed ratioed spectra we confronted them with the certified CRISM

spectra, by comparing their absorption features. The overall shape of the spectrum instead is generally less indicative of the mineralogy, as it can be affected by the ratioing. Lastly, it is in fact important to mention that some spectra exhibit slope issues, especially in the last part of the spectrum. This is typically due to the fact that in some cases the neutral spectrum presents a more steep slope in the 2400 nm - 2600 nm interval (see for example the first image in figure 3.1), thus resulting in the ratio operation to give a resulting upward slope. In any case the absorption bands are still clearly visible, especially in the smooth ratioed spectra obtained with the polygon method, so this was not much of a serious issue in spectra recognition.

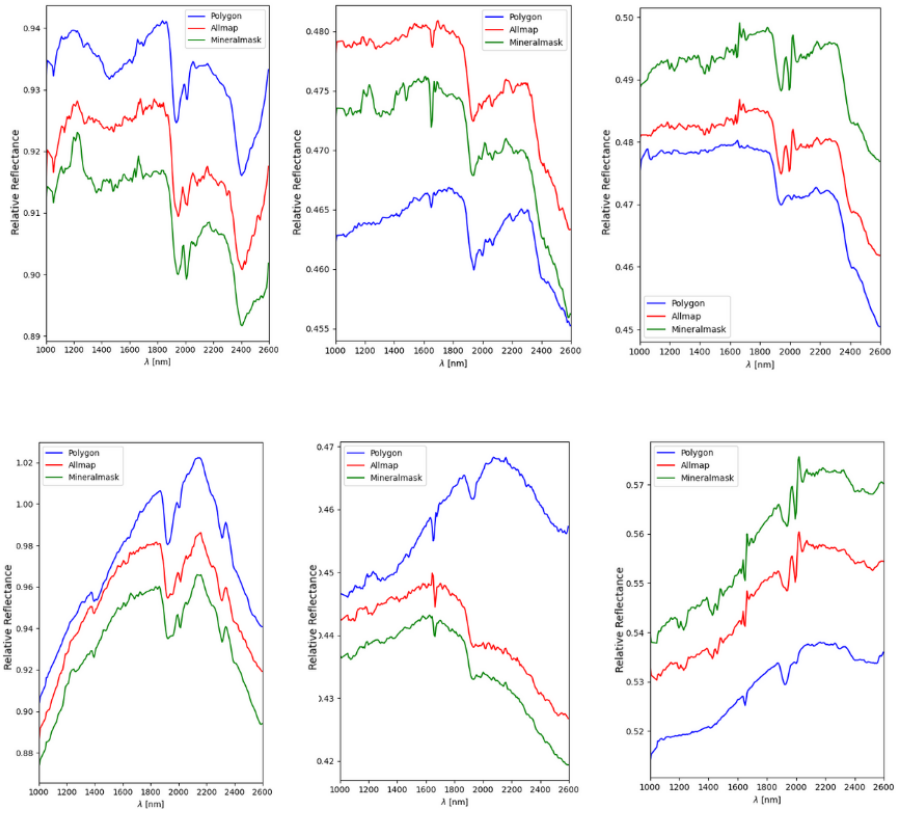

Figure 3.1: Example to show that the polygon method gives the best ratioed spectrum. On the first row of figures some sulfate spectra are shown and in the second row phyllosilicates spectra are shown. The first column shows spectra taken from cube FRT00009b5a, the second are taken from FRT00003e24 and the third one from FRT000062e6. The blue spectra are the one obtained with the polygon method, the red one is obtained with the all-map method and the green one is obtained with the mineral mask method. Each separate figure is associated to one particular ROI. As it can be seen quite clearly, the polygon and all-map methods are more likely to cause artefacts in some parts of the spectrum, like for example at 1200 nm and at 2000 nm, and in general the spectrum is noisier with respect to the one obtained through the polygon method.

For the sake of completeness, in figure 3.2, 3.3 and 3.4 we present the resulting selected pix-

els both for the all-map and mineral mask methods. In table 3.1 we give the threshold values used for the mineral mask method. For summary, the all-map method gave, respectively for FRT00009b5a, FRT00003e24 and FRT000062e6, 579, 1619 and 3534 total neutral pixels, while the mineral mask method gave, for the same cubes, 13961, 17437 and 4364 selected pixels.

in table 3.2 we present a summary table of all the minerals we identified in our regions with the mineral's components that causes those absorptions.

Table 3.1: Threshold values for the mineral mask for our CRISM cubes. The first block is for FRT00009b5a, the second is for FRT00003e24 and the last is for FRT000062e6.

R770	BDI1000IR	OLINDEX3	BD1300	LCPINDEX2	HCPINDEX2
0.23	0.035	0.09	0	0	0
D2200	**BD2290**	**D2300**	**BD2500_2**	**SINDEX2**	**BD1900_2**
0.001	0.001	0.001	0	0.0045	0.012
R770	**BDI1000IR**	**OLINDEX3**	**BD1300**	**LCPINDEX2**	**HCPINDEX2**
0.27	0.023	0	0	0	0
D2200	**BD2290**	**D2300**	**BD2500_2**	**SINDEX2**	**BD1900_2**
0.0003	0	0	0	0.0072	0
R770	**BDI1000IR**	**OLINDEX3**	**BD1300**	**LCPINDEX2**	**HCPINDEX2**
0.266	0.0253	0.0794	0.01	0.0035	0
D2200	**BD2290**	**D2300**	**BD2500_2**	**SINDEX2**	**BD1900_2**
0	0	0	0	0.0046	0

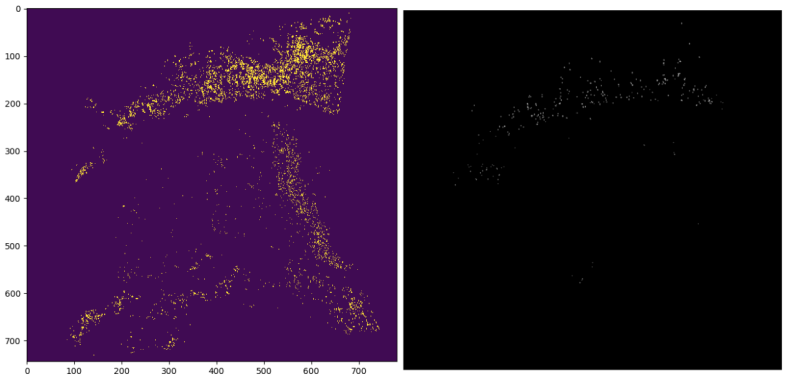

Figure 3.2: On the left image the selected pixels for the mineral mask method for the cube FRT00009b5a are presented. On the right image the resulting null pixels for the all-map method for the cube FRT00009b5a are presented.

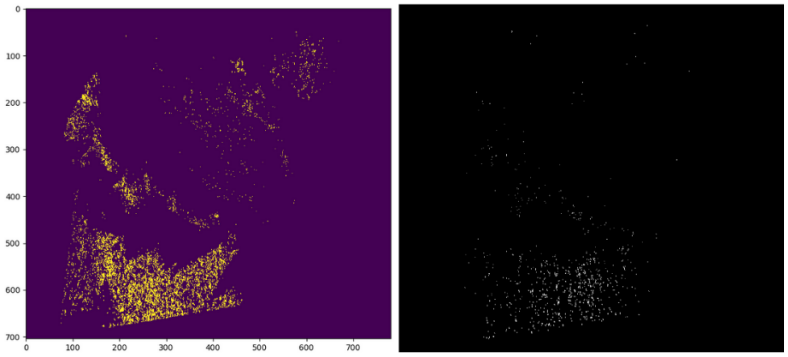

Figure 3.3: On the left image the selected pixels for the mineral mask method for the cube FRT00003e24 are presented. On the right image the resulting null pixels for the all-map method for the cube FRT00003e24 are presented.

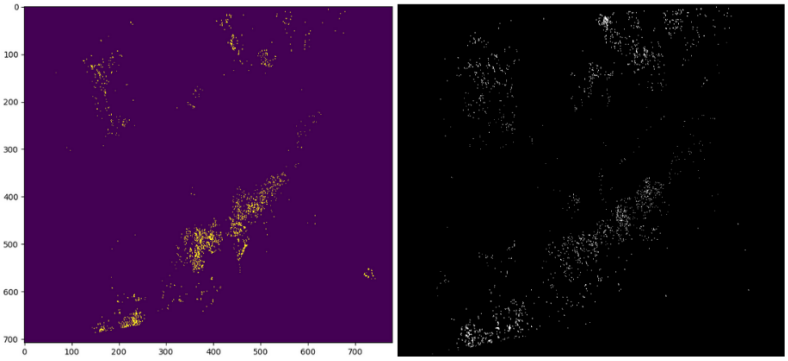

Figure 3.4: On the left image the selected pixels for the mineral mask method for the cube FRT000062e6 are presented. On the right image the resulting null pixels for the all-map method for the cube FRT000062e6 are presented.

Table 3.2: Summary table with all the found minerals and their absorption's origin. The absorptions are given as from the certified CRISM spectras (MICA, 2019). The cause of the absorptions have the citation at the apex: [1] is (Clark et al., 1990), [2] is (MICA, 2019) and [3] is (Cloutis et al., 2006). The explanations are given below the absorption wavelength and the one marked with "?" are the one for which we did not found an explanation in the literature.

	Abs. 1 [nm]	Abs. 2 [nm]	Abs. 3 [nm]
Polyhyd. Sulfate	1180 H_2O [3]	1430 H_2O [3]	1940 H_2O [2]
Monohyd. Sulfate	1620 ?	1970 H_2O [3]	2140 $H_2O + OH + SO$ [3]
Mg Smectite	1410 $H_2O + OH$ [1]	1920 H_2O [1]	2310 Mg-OH [2]
Fe Smectite	1420 H_2O [1]	1910 H_2O [1]	2230 Fe-OH
Al Smectite	1410 $H_2O + OH$ [1]	1910 H_2O [1]	2200 Al-OH [1]
Talc	1390 Mg_3-OH [1]	1910 H_2O [2]	2240 Mg-OH [1]

	Abs. 4 [nm]	Abs. 5 [nm]	Abs. 6 [nm]
Polyhyd. Sulfate	2430 H_2O [2]		
Monohyd. Sulfate	2400 H_2O [2]		
Mg Smectite	2390 H_2O [2]		
Fe Smectite	2290 Fe-OH [1]	2390 H_2O [2]	2520 Fe-OH
Al Smectite			
Talc	2310 Mg-OH [1]	2390 Mg-OH [1]	2470 ?

3.1.1 FRT00009B5A

From this cube we selected 8 different ROIs: 4 using the HYD (hydrated minerals) RGB map and 4 using the PHY (phyllosilicates) RGB map (figure 3.5 shows all the RGB maps generated for this cube, table 3.3 shows the stretch values for each map), finding:

- Smectites of, respectively, Aluminium, Iron and Magnesium;
- Talc;
- Polyhydrated and monohydrated sulfates.

The ROIs were named progressively pertaining to the parent RGB map on which they were selected: HYD_1, HYD_2, HYD_3, HYD_4, PHY_1, PHY_2, PHY_3 and PHY_4.
The ROIs named HYD_2 and HYD_4 revealed a composition of polyhydrated sulfates, while HYD_1 revealed a composition of monohydrated sulfates. Regarding the other ROIs, all of them resulted in various composition of smectites: HYD_3 gives a composition of mixed Iron and Magnesium smectites, PHY_1 gives a main composition of Magnesium smectites, PHY_2 is similar to HYD_3, but with more Iron than Magnesium and gives hints about the possible presence of Magnesium carbonate, but more analysis should be conducted to obtain solid conclusions. Lastly, PHY_3 contains talc and PHY_4 has a composition of mainly Aluminium smectite mixed with Magnesium smectite. In the following paragraphs we present the results for each ROI we selected. In table 3.4 the total number of spectra used for each ROI is presented, together with the total number of spectra used for the neutral spectra using the polygon method. Lastly, in figure 3.2 we present all the ROIs selected for this cube and in figure 3.2 we present the neutral polygons chosen for the normalization corresponding to each ROI.

Table 3.3: Stretch values for the FRT00009b5a RGB maps.

	R_{min}	R_{max}	G_{min}	G_{max}	B_{min}	B_{max}
FAL	0.1416	0.3	0.1544	0.3	0.144	0.279
MAF	0.0627	0.1088	0	0.0146	0	0.0103
HYD	0.0048	0.0173	0	0.0091	0.0048	0.026
PHY	0	0.0095	0	0.0083	0.0048	0.0267
PFM	0	0.0033	0	0.0111	0.0056	0.0099
HYS	0	0.0048	0	0.006	0.0056	0.0267
FM2	0.2111	0.2556	0	0.0123	0.0103	0.0181

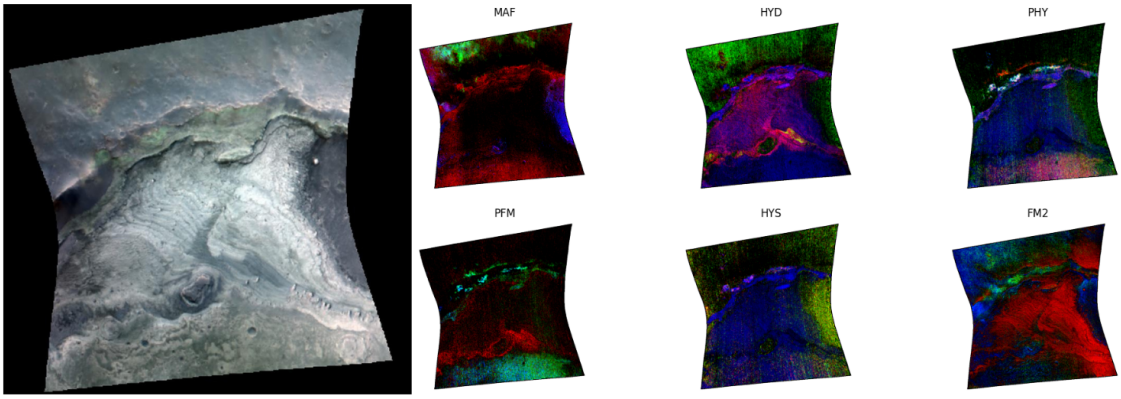

Figure 3.5: Generated RGB maps for the cube FRT00009b5a.

Table 3.4: Total number of spectra used for the mean target spectra and neutral spectra used for the median neutral spectra listed for each ROI.

	Target spectra	Neutral spectra
HYD_1	445	1301
HYD_2	4468	9616
HYD_3	1488	762
HYD_4	1340	1373
PHY_1	356	1959
PHY_2	18258	24232
PHY_3	794	8270
PHY_4	166	572

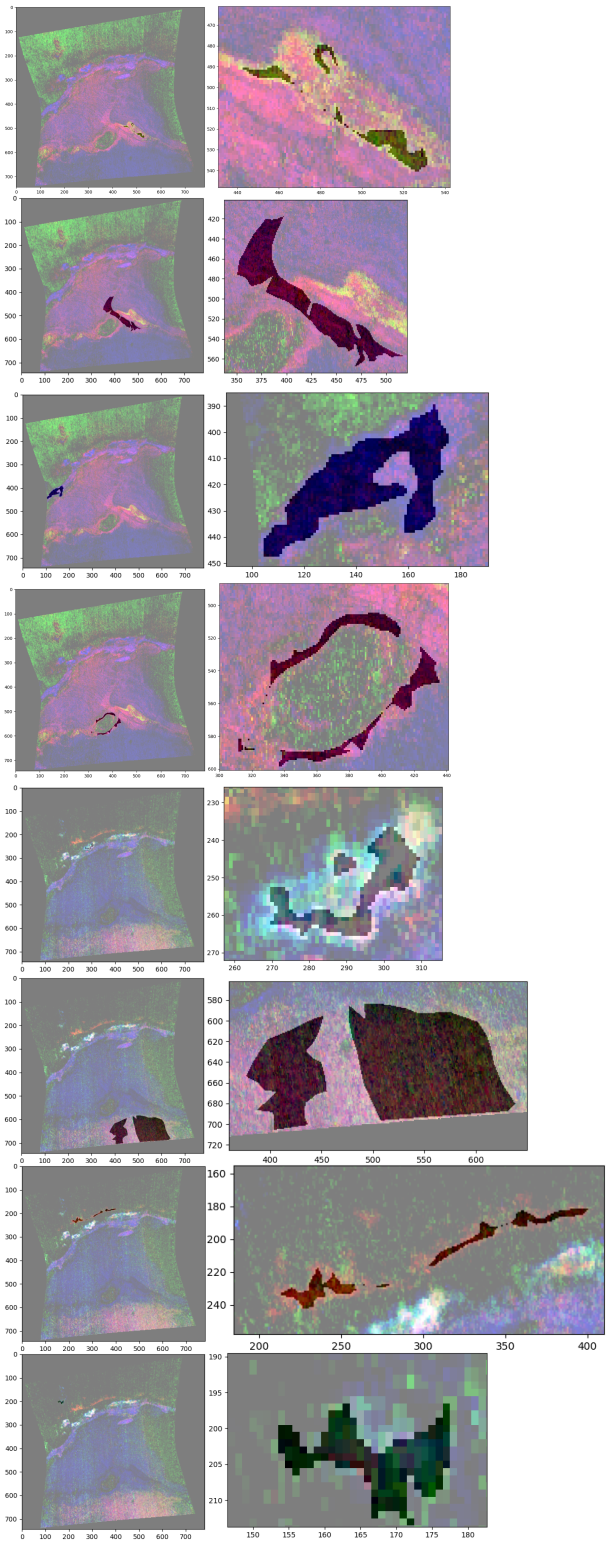

Figure 3.6: Selected ROIs for the cube FRT00009b5a. On the right there is position of the ROI on the global scale of the CRISM cube while, on the left, there is the detailed vision of the ROI. From top to bottom are presented the ROIs in the following order: HYD_1, HYD_2, HYD_3, HYD_4, PHY_1, PHY_2, PHY_3 and PHY_4.

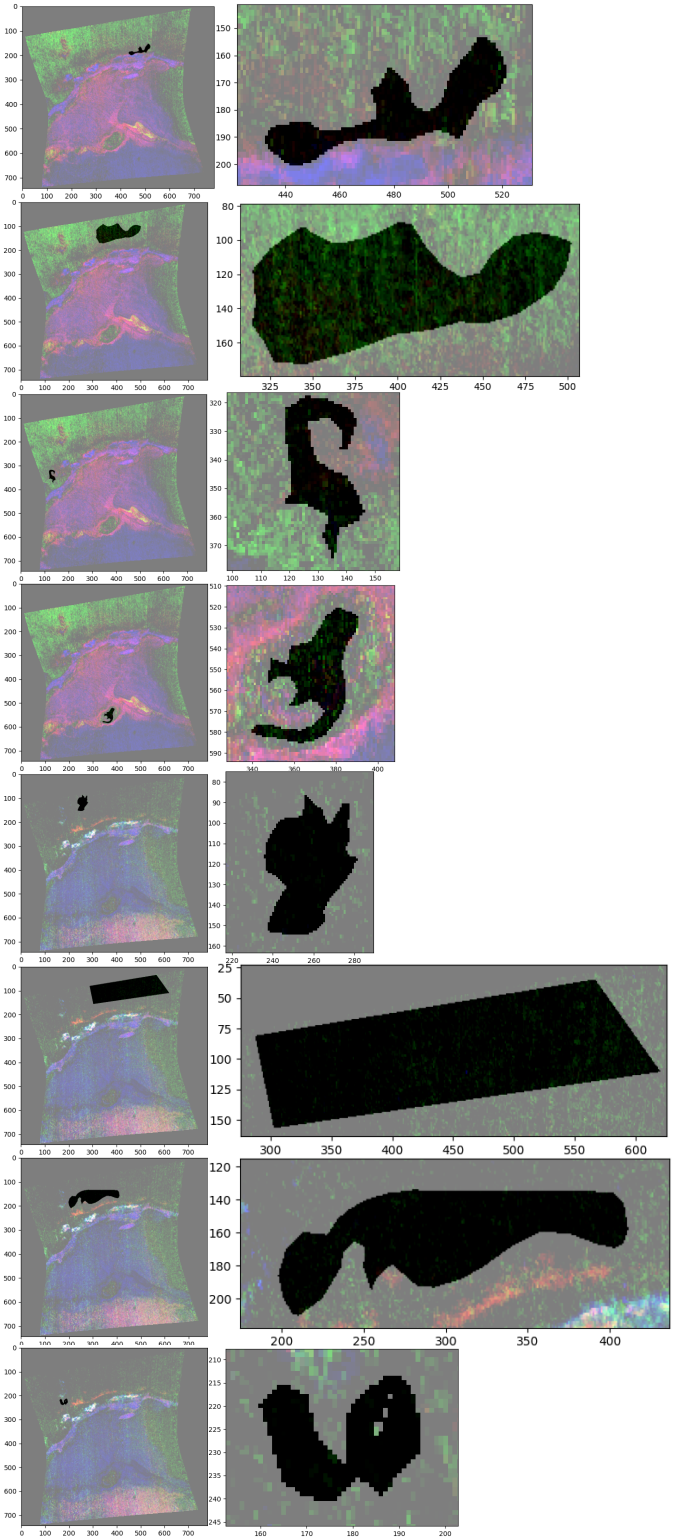

Figure 3.7: Selected neutral ROIs for the cube FRT00009b5a. On the right the position of the neutral ROI on the global scale of the CRISM cube while, on the left, there is the detailed vision of the neutral ROI. From top to bottom are presented the neutral ROIs in the following order: HYD_1, HYD_2, HYD_3, HYD_4, PHY_1, PHY_2, PHY_3 and PHY_4.

Following (from figure 3.8 to 3.15) we present all the resulting spectra, for the sake of simplicity we describe here what the figures mean avoiding to repeat the same things for each figure:

- The first plot represents the mean spectrum of the target with the standard deviation, 1-σ, (blue) and the median neutral spectrum with enhanced median absolute deviation (black);
- The second plot represents in blue the ratioed and smoothed target spectrum, which is obtained by ratioing the mean target spectrum with the median neutral spectrum shown in the first plot, and in black we have the certified CRISM spectrum as given by (MICA, 2019) and (Viviano-Beck et al., 2014). The red vertical lines mark the minimum of the absorption features for our spectrum;
- The third plot represent the laboratory spectrum as given by (MICA, 2019). Again, the red vertical lines mark the absorptions of the spectrum.

For all spectra the proposed mineralogy is given in the legend of the second plot. The position of the observed absorption features for all three spectra (from MICA, from laboratory, and finally from our ROIs) and associated mineralogy are shown in table 3.5. This description is valid also for figures from 3.21 to 3.27 and from 3.31 to 3.35.
For this particular cube we have found deposits of both Polyhydrated (ROIs HYD_2 and HYD_4, see figures 3.9 and 3.11) and Monohydrated Sulfate (ROI HYD_1, see figure 3.8). These compositions are well recognizable from the bands at 2140 nm and 2400 nm, for the Monohydrated Sulfate, and the bands at 1940 nm and 2430 nm for the Polyhydrated Sulfate. Moreover the difference between the two sulfates is well recognizable from the overall shape.
We then have phyllosilicates in several areas of the scene: we have found traces of Mg smectite in HYD_3, PHY_1, PHY_2 and PHY_4. The spectra of the phyllosilicates are shown in 3.10, 3.12, 3.13 and 3.15. Specifically, the ROI PHY_1 reveals a major composition of Mg Smectite, as revealed both by the shape of the spectrum and the really small difference between the position of the absorptions in the certified CRISM spectrum and the target spectrum, as well as in the laboratory spectrum (see table 3.5). Indeed we clearly see the 1900 nm band from the H_2O vibration and the water-related combinations at 1400 nm and 2400 nm. Moreover, also the absorption around 2300 nm is really close to its teorethical value (see table 3.5), meaning that indeed the Iron composition is at the lowest (MICA, 2019). The ROIs HYD_3 and PHY_2 reveal phyllosilicates with a mixed composition between Magnesium and Iron Smectites, but relatively richer in Magnesium for HYD_3 and Iron for PHY_2. This is clear because the supplementary line around 2500 nm that arise from Fe-OH vibrational modes is not so enhanced and,

moreover, we see that our absorptions around 1400 nm and 2300 nm are, respectively 1414.59 nm and 2304.56 nm, so closer to the certified CRISM's spectra value for Mg smectite (1410 nm, 2310 nm) than to Fe smectite (1420 nm, 2290 nm) (MICA, 2019).
In general, having a mixed composition of Fe/Mg smectite has as main effect the shift to longer wavelengths for the absorption line at ~2300 nm as the Mg content increases (MICA, 2019).
The other ROI, PHY_4, shows evidence of Magnesium smectite this time mixed with Aluminium smectite, instead of Iron smectite. The presence of Aluminum is well visible from the band around 2200 nm, which is typical of minerals with Al-OH bonds (MICA, 2019). Overall the presence of both minerals can be inferred by the contemporaneous presence of the single band around 2200 nm (Al Smectite) and the couple of bands around 2310 nm and 2390 nm (Mg Smectite), with the first caused by Mg-OH bonds and the other one by combination modes of water inside the crystalline structure (MICA, 2019). This mix between Al and Mg smectite also shows the absorption at 1400 nm, and this is related both to presence of the Mg-OH bond and of water inside the crystalline structure (MICA, 2019). Finally, the ratioed spectrum from PHY_3 ROI can be associated to Talc. We can see both the shoulder that gives rise to the absorption around 2230 nm and three absorptions located around 2320 nm, 2390 nm and 2470 nm that are due to Mg-OH bond. Also, the absorption at 1400 nm is visible and its caused by vibrational modes of the OH molecule (Clark et al., 1990). The main difference used to discriminate between talc and Mg smectite is the lack of the 1900 nm band, that we can anyway see but lot smaller than in the Mg smectite bearing spectra and could given by the mixing with some smectite, and the narrowing of the 1400 nm band caused by the less water content in relation to Mg smectite (MICA, 2019). In general, to see what mineral's component cause the observed absorption see table 3.2.

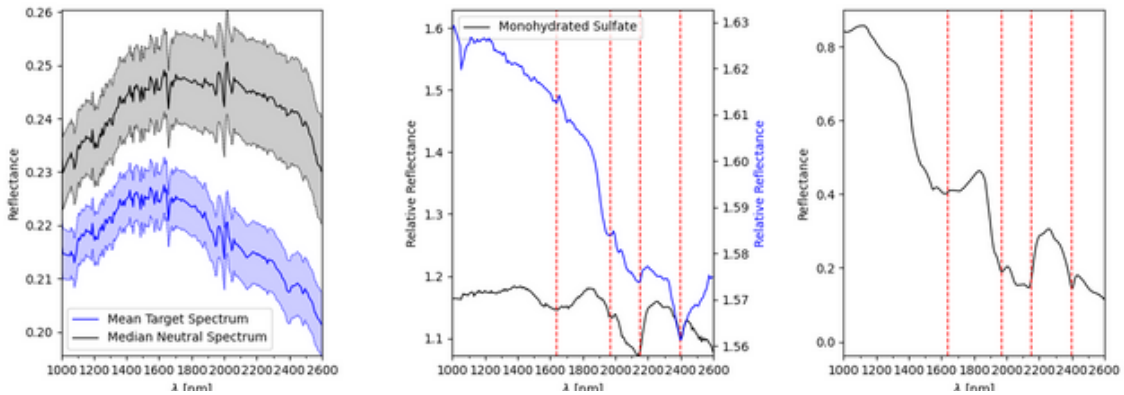

Figure 3.8: Spectral results for ROI HYD_1 of cube FRT00009b5a. We have associated this spectrum to monohydrated sulfate.

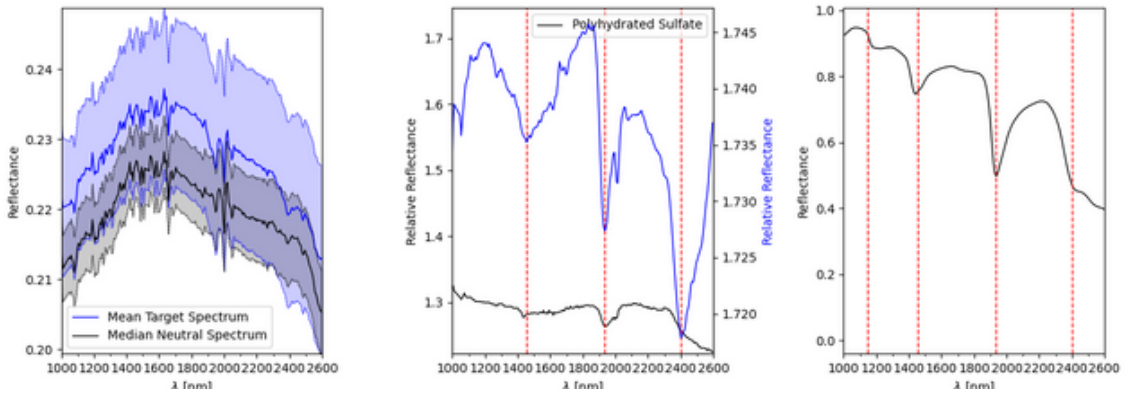

Figure 3.9: Spectral results for ROI HYD_2 of cube FRT00009b5a. We have associated this spectrum to polyhydrated sulfate.

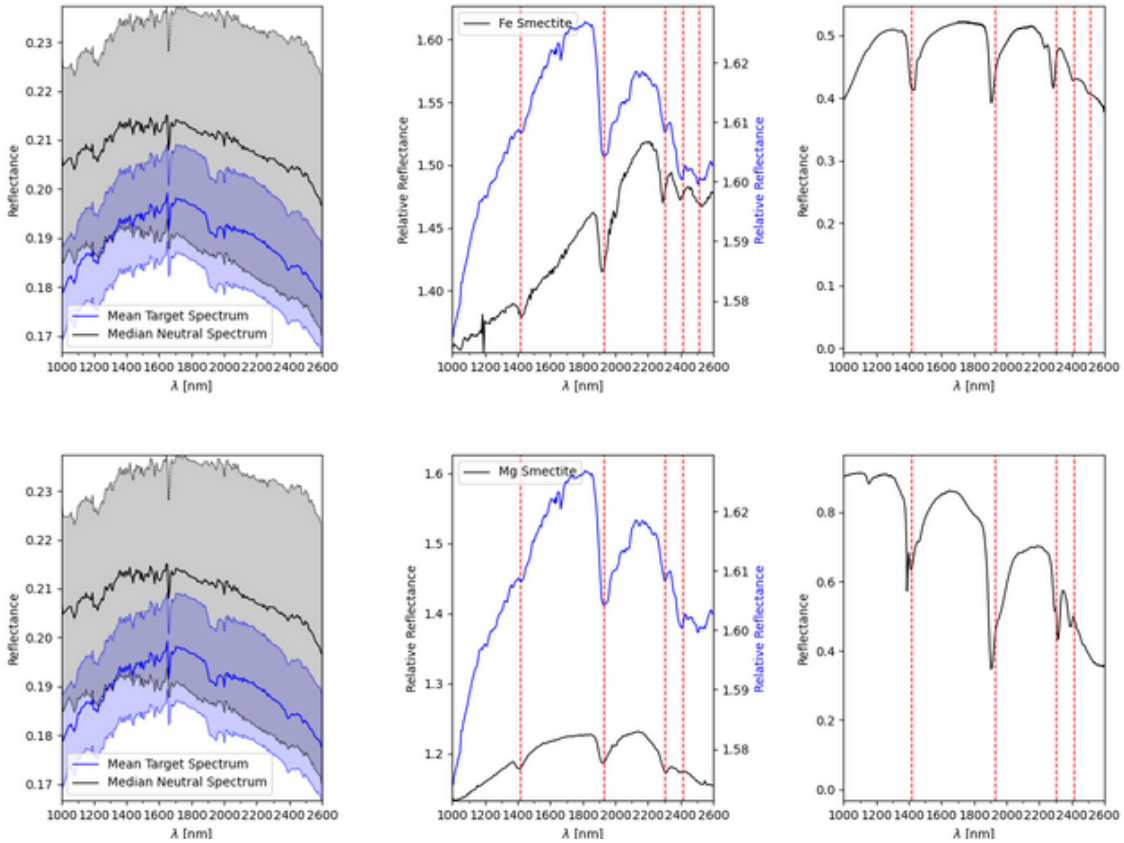

Figure 3.10: Spectral results for ROI HYD_3 of cube FRT00009b5a. We have associated this spectrum to a mix of Fe/Mg smectite.

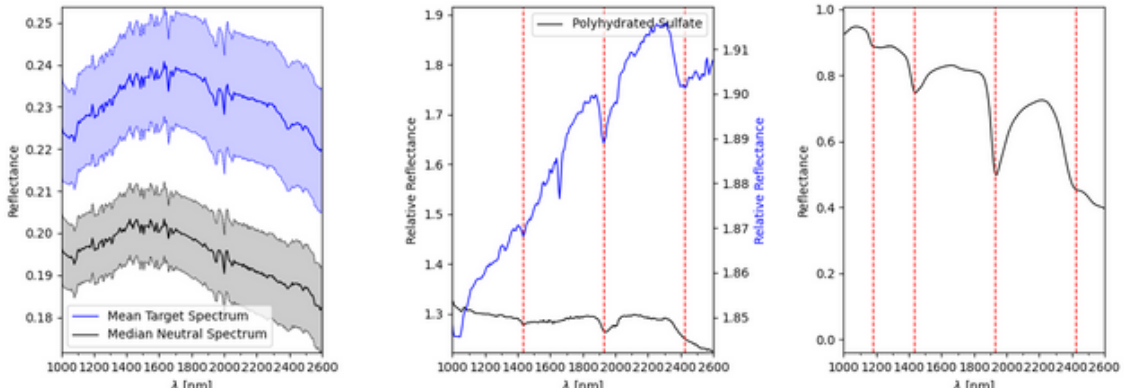

Figure 3.11: Spectral results for ROI HYD_4 of cube FRT00009b5a. We have associated this spectrum to polyhydrated sulfate.

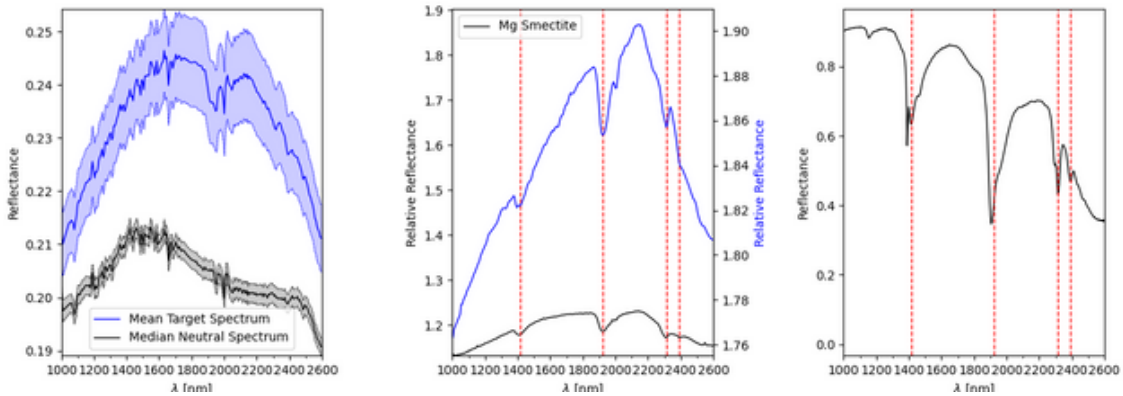

Figure 3.12: Spectral results for ROI PHY_1 of cube FRT00009b5a. We have associated this spectrum to Mg smectite.

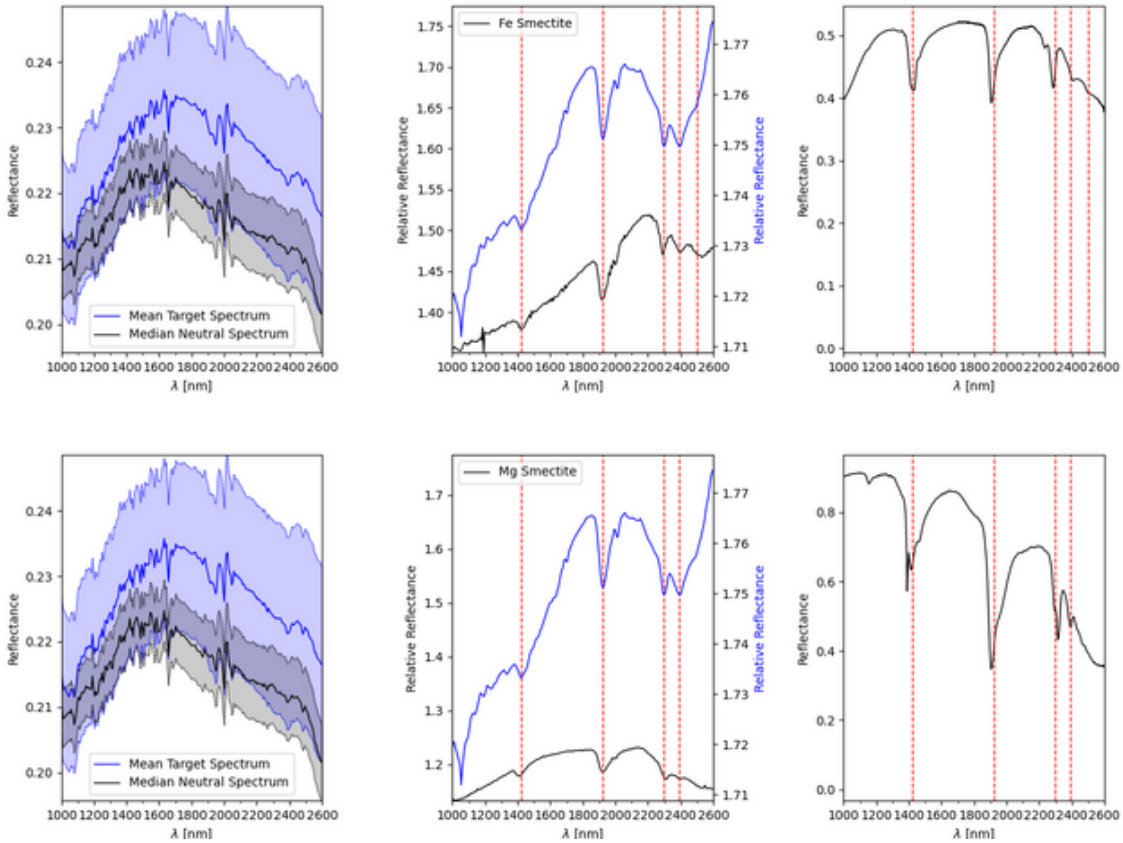

Figure 3.13: Spectral results for ROI PHY_2 of cube FRT00009b5a. We have associated this spectrum to a mix of Fe/Mg smectite.

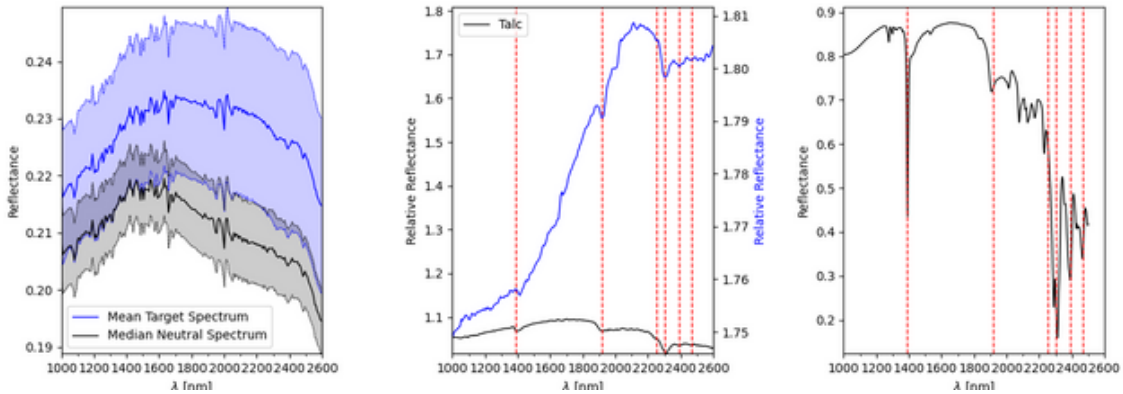

Figure 3.14: Spectral results for ROI PHY_3 of cube FRT00009b5a. We have associated this spectrum to talc.

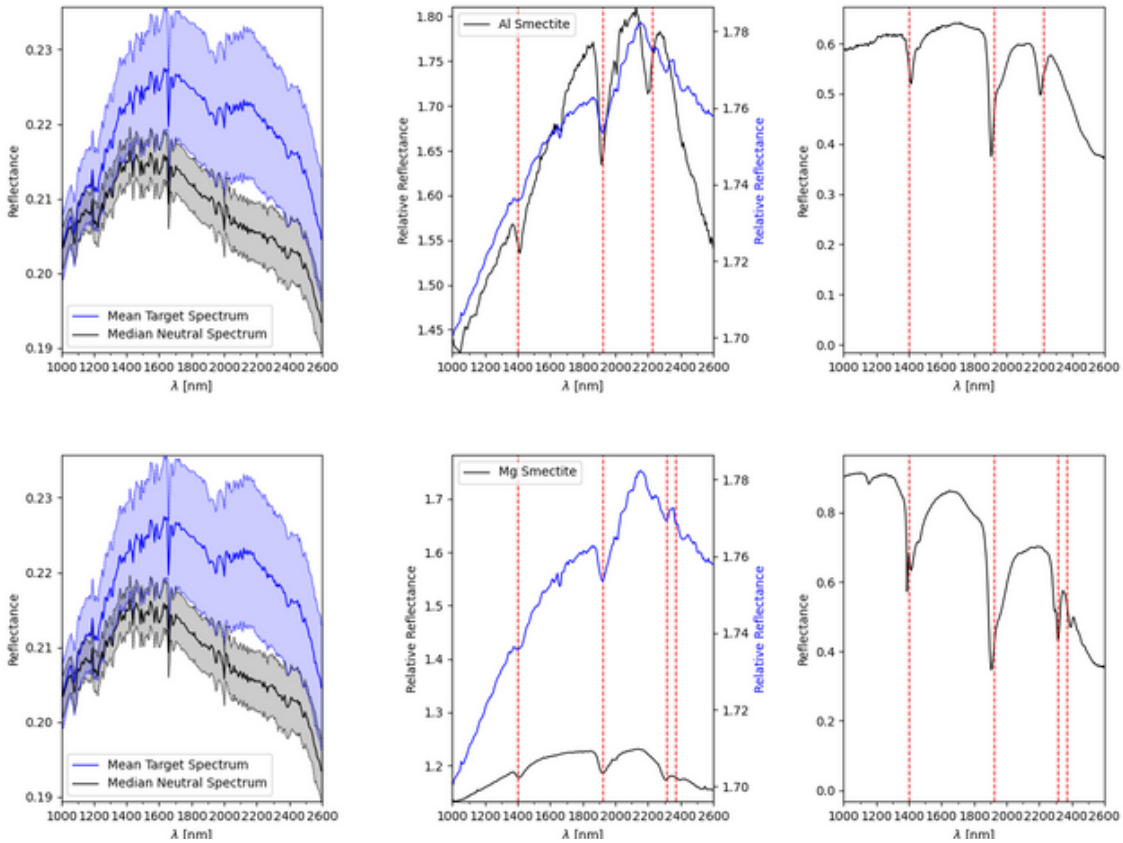

Figure 3.15: Spectral results for ROI PHY_4 of cube FRT00009b5a. We have associated this spectrum to a mix of Al/Mg smectite.

Table 3.5: Summary table of the spectral analysis results for each ROI. On the first column there is the detect mineral, the second column stores the certified CRISM lines as given from (MICA, 2019), the second column stores the laboratory absorption, always as given by (MICA, 2019) and the last one stores our detected absorption lines.

	Mineral	MICA Abs. [nm]	Lab. Abs. [nm]	Target Abs. [nm]
HYD$_1$	Monohydrated Sulfate	1630, 1970, 2140, 2400	1620, 1970, 2140, 2400	1638.16, 1967.64, 2145.9, 2397.2
HYD$_2$	Polyhydrated Sulfate	X, 1430, 1940, 2430	1180, 1440, 1940, 2420	1145.51, 1454.02, 1934.65, 2403.82
HYD$_3$	Mg Smectite	1410, 1920, 2310, 2390	1390, 1910, 2320, 2390	1414.59, 1928.06, 2304.56, 2410.44
	Fe Smectite	1420, 1910, 2290, 2390, 2520	1420, 1900, 2230, 2280, 2410, 2500	1414.59, 1928.06, 2304.56, 2410.44, 2509.72
HYD$_4$	Polyhydrated Sulfate	X, 1430, 1940, 2430	1180, 1440, 1940, 2420	1178.29, 1434.31, 1928.06, 2423.68
PHY$_1$	Mg Smectite	1410, 1920, 2310, 2390	1390, 1910, 2320, 2390	1414.59, 1921.46, 2311.18, 2390.58
PHY$_2$	Mg Smectite	1410, 1920, 2310, 2390	1390, 1910, 2320, 2390	1421.16, 1921.46, 2297.95, 2390.58
	Fe Smectite	1420, 1910, 2290, 2390, 2520	1420, 1900, 2230, 2280, 2410, 2500	1421.16, 1921.46, 2297.95, 2390.58, 2503.12
PHY$_3$	Talc	1390, 1910, 2240, 2310, 2390, 2470	1390, 1910, 2230, 2320, 2390, 2470	1388.32, 1914.87, 2251.65, 2304.56, 2390.58, 2470.03
PHY$_4$	Al Smectite	1410, 1910, 2200	1410, 1910, 2210	1401.45, 1921.46, 2225.21
	Mg Smectite	1410, 1920, 2310, 2390	1390, 1910, 2320, 2390	1401.45, 1921.46, 2311.18, 2370.72

As a last note it is important to say that, for the ROI PHY_1, we also tested single parameter maps, in order to try getting the clearest spectrum possible of that area. We did it by selecting all the cube's pixels that have the strongest values of the parameter D2200, namely, greater than 0.9 (metti proprio il valore) (see table 2.5 for more details about this spectral parameters. The pixels selected with this method are shown in figure 3.16, where we also show the area from which we extracted the neutral spectrum for the ratioing. The results are shown in figure 3.16 and confirm a composition of Mg smectite, probably mixed with some Al smectites.

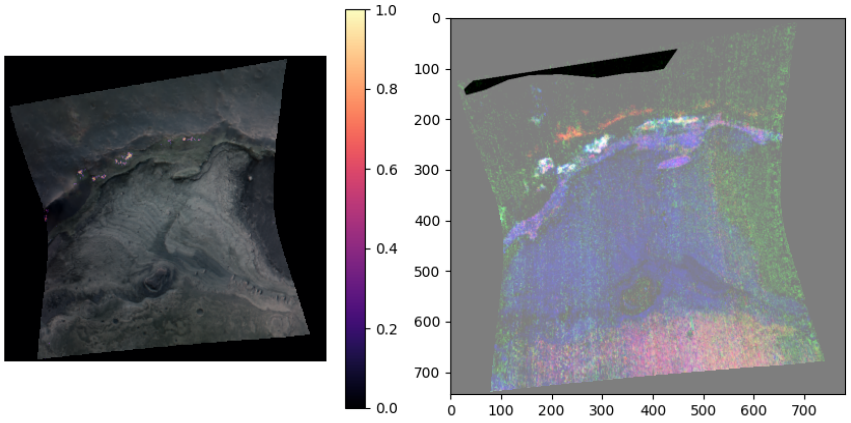

Figure 3.16: On the left we present the pixels that had a value of the D2200 spectral parameter of the threshold of 0.9. On the right there is the neutral polygon used for the spectral rationing.

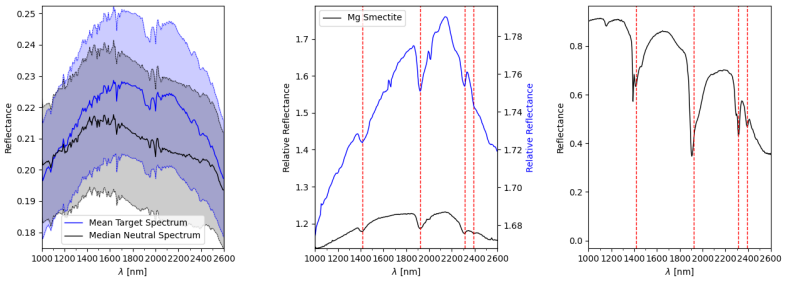

Figure 3.17: Resulting spectra from the single parameter map (D2200) extracted spectrum. We associated the resulting spectrum to the same mineral of the ROI PHY_1, Mg smectite.

3.1.2 FRT00003E24

From this cube we selected 7 different ROIs: 6 using the HYD RGB map and 1 using the PHY RGB map (see figure 3.18 to see all the RGB maps generated for this cube, table 3.6 to see the stretch values for each map), finding Iron, Magnesium and Aluminium Smectites, Polyhydrated and Monohydrated Sulfates. The ROIs were named progressively pertaining to the parent RGB map: HYD_1, HYD_2, HYD_3, HYD_4, HYD_5, HYD_6 and PHY_1 Particularly, the ROIs named HYD_1 and HYD_2 revealed a composition of, respectively polyhydrated sulfate and monohydrated sulfate. All the other HYD ROIs resulted in a composition of mainly Magnesium Smectite. PHY_1 gives a mixed composition of Aluminium and Magnesium Smectite. In the following paragraphs we present the results for each ROI we selected and in table 3.7 the total number of spectra extracted from each ROI is presented, together with the total number of spectra used for the neutral spectra using the polygon method. Lastly, in figure 3.19 we present all the ROIs selected for this cube and in figure 3.20 we present the neutral polygons chosen for the normalization corresponding to each ROI.

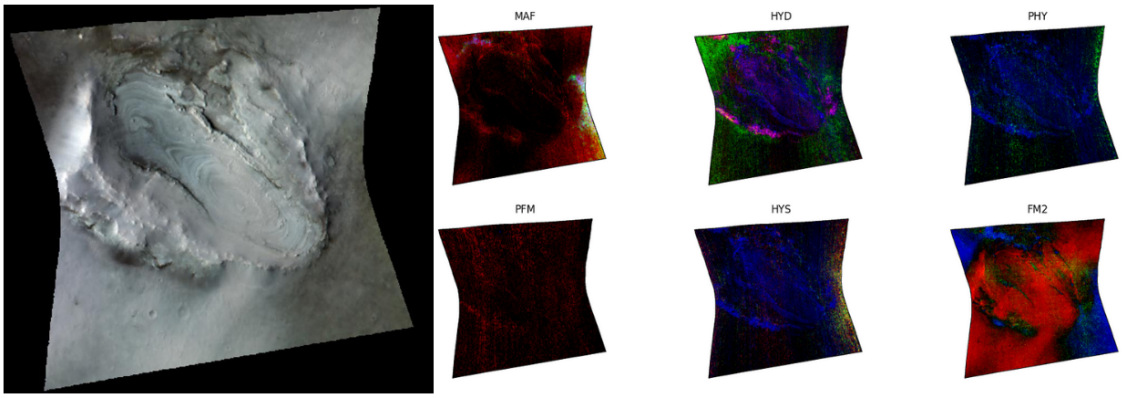

Figure 3.18: Generated RGB maps for the cube FRT00003e24. The false color image is presented on the left, while all the other are presented and labeled on the right.

Table 3.6: Stretch values for the FRT00003e24 RGB maps.

	R_{min}	R_{max}	G_{min}	G_{max}	B_{min}	B_{max}
FAL	0.1513	0.3533	0.18	0.3267	0.1773	0.3043
MAF	0.059	0.0996	0	0.015	0	0.008
HYD	0.0074	0.0187	0.0025	0.0105	0	0.0096
PHY	0	0.0002	0	0.0036	0	0.015
PFM	0.003	0.008	0	0.001	0	0.0002
HYS	0	0.0038	0	0.0036	0	0.0146
FM2	0.2047	0.2438	0	0.0087	0.012	0.017

Table 3.7: Total number of spectra used for the mean target spectra and neutral spectra used for the median neutral spectra listed for each ROI.

	Target spectra	Neutral spectra
HYD_1	553	5020
HYD_2	174	2500
HYD_3	1245	3049
HYD_4	451	3775
HYD_5	2246	2341
HYD_6	497	361
PHY_1	132	1204

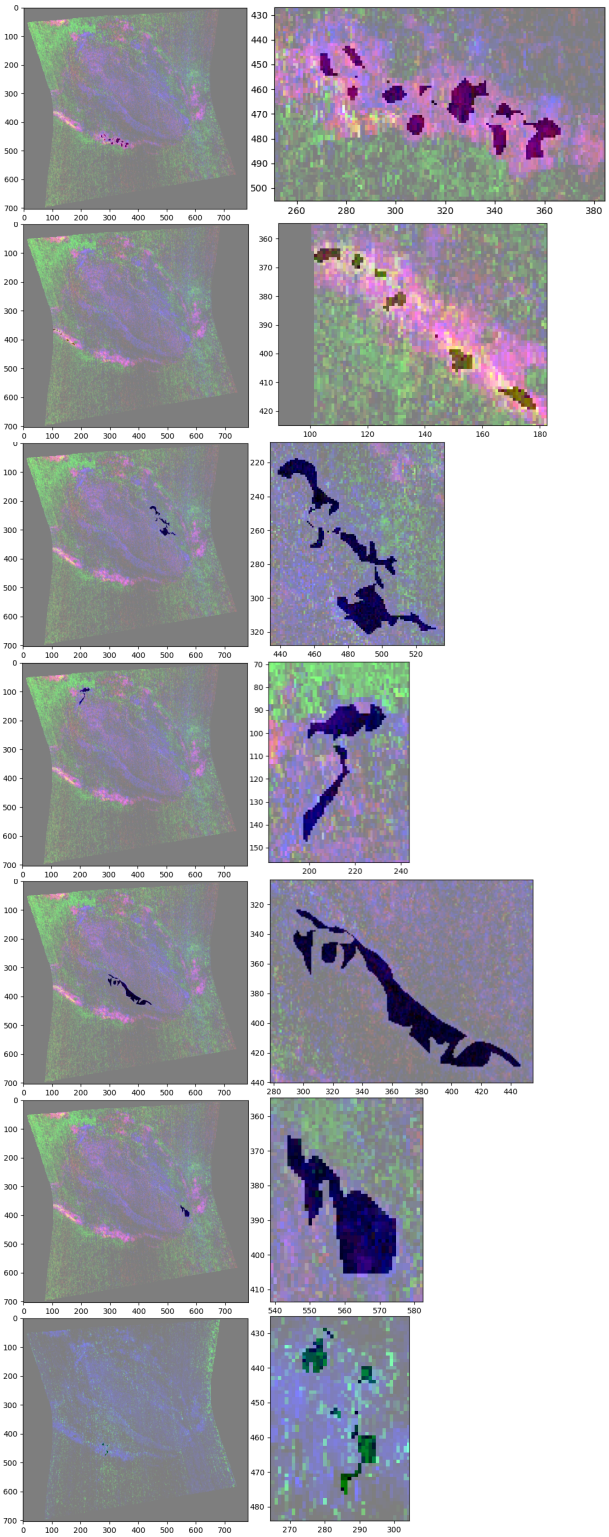

Figure 3.19: Selected ROIs for the cube FRT00003e24. On the right there is position of the ROI on the global scale of the CRISM cube while, on the left, there is the detailed vision of the ROI. From top to bottom are presented the ROIs in the following order: HYD_1, HYD_2, HYD_3, HYD_4, HYD_5 and HYD_6, PHY_1.

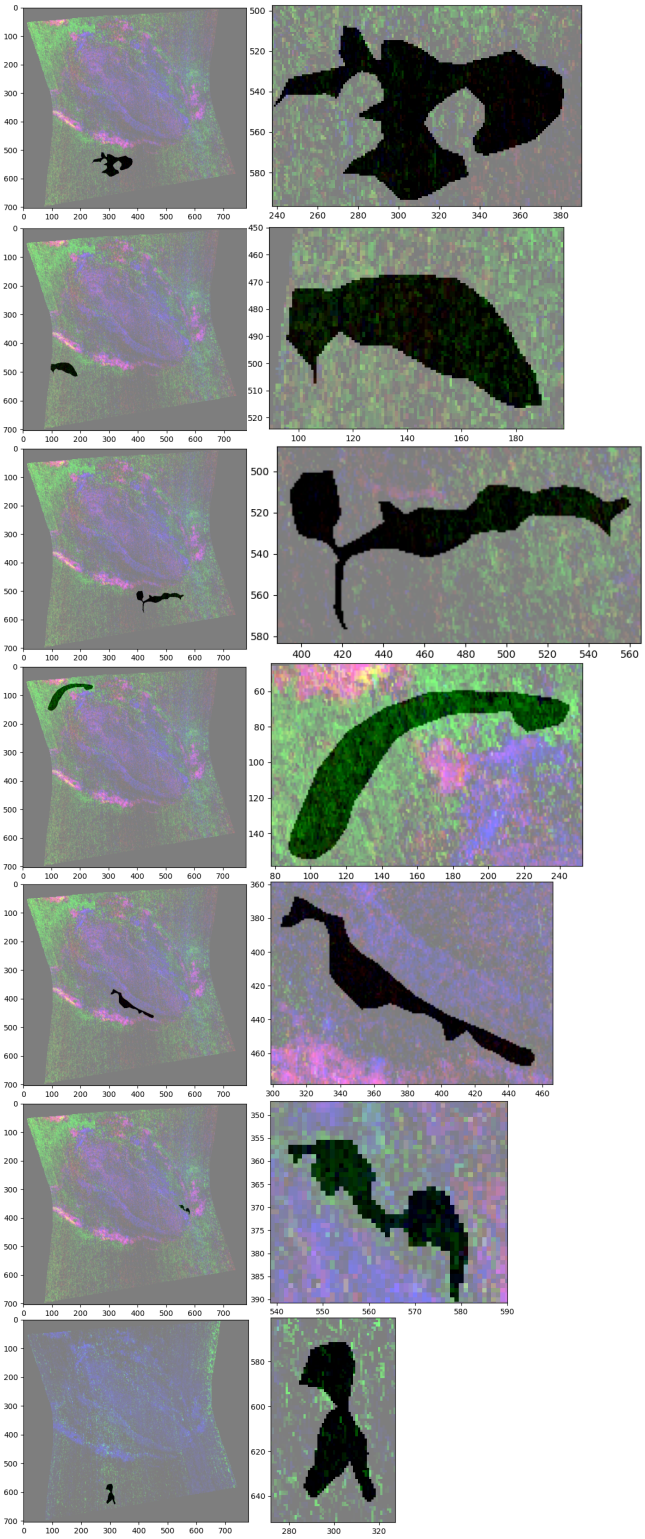

Figure 3.20: Selected neutral ROIs for the cube FRT00003e24. On the right there is position of the neutral ROI on the global scale of the CRISM cube while, on the left, there is the detailed vision of the neutral ROI. From top to bottom are presented the ROIs in the following order: HYD_1, HYD_2, HYD_3, HYD_4, HYD_5 and HYD_6, PHY_1.

The spectra extracted from this cube were a lot more noisy than the one extracted from FRT00009b5a.
This might depend on various factors such as specific observation conditions, sensor issues, or processing issues arisen during the creation of the MTRDR product. Nevertheless, the noise was not a huge obstacle for the mineralogical identification and we managed to extract several significant detections. For this particular cube we have found, similarly to FRT00009b5a, deposits of both polyhydrated (ROI HYD_1, see figure 3.21) and monohydrated Sulfate (ROI HYD_2, see figure 3.22). These compositions are well recognizable from the bands at 2140 nm and 2400 nm, for the monohydrated sulfate, that are caused by water vibrational combination modes, and the bands at 1940 nm and 2430 nm for the polyhydrated sulfate that are caused, respectively, by the molecular water stretch and bend vibration and by water combination modes. We then have found traces of Fe/Mg smectite in all the other ROIs, minus the one named PHY_1, and this is well recognizable in figures 3.23, 3.24, 3.25 and 3.26. Fe/Mg smectites tend towards a more Magnesium-rich composition. This can be seen by comparing the absorptions of the certified CRISM or Laboratory spectra with the ones extracted in our scene (see table 3.8) as we can see that our absorption near 2310 nm are all around that value. Indeed for HYD_3 we have it at 2317.79 nm, for HYD_4 we have it at 2304.56 nm, for HYD_5 we have it at 2311.18 nm and for HYD_6 we have it at 2297.95 nm. So we see that, if HYD_3 shows somewhat high Iron abundance in the mixing, and HYD_4, HYD_5 and HYD_6 shows almost no presence of this component. This is also well visible from the plots: 3.23 well shows both the longer-wavelength shift of the 2310 nm band and the presence of $\sim$2500 nm Fe-OH band, 3.24 shows clearly that the band of Mg-OH at 2310 nm is well in place when compared to the certified CRISM spectrum and shows small trace of the 2500 nm Fe-OH trace, 3.25 have the 2310 nm band almost perfectly in place with the certified CRISM spectrum and shows the $\sim$2500 nm absorption of the Fe-OH bond but this could be some kind of artifact related some some slope issue and 3.26 also is well placed when compared to the certified CRISM spectrum and provides almost no traces of the Iron content from the $\sim$2500 nm. Anyway it is almost impossible to completely rule out the presence of some Fe smectite mixed with the Mg smectite, so we classified all of these ROIs as containing Fe/Mg smectite.
Lastly, the small ROI PHY_1 seems to lead to a composition of Al smectite. This last spectrum has a strong downward slope, probably due to mixed contamination from polyhydrated sulfates (that are present in the same zone) and from the noise-related issues we spoke about earlier. Anyway the Aluminium content is well recognizable from from the band, in shape of a shoulder (see figure 3.27) around 2200 nm that is due to vibrational modes of the Al-OH bond.

In general, to see what component in the mineral cause the observed absorption see table 3.2.

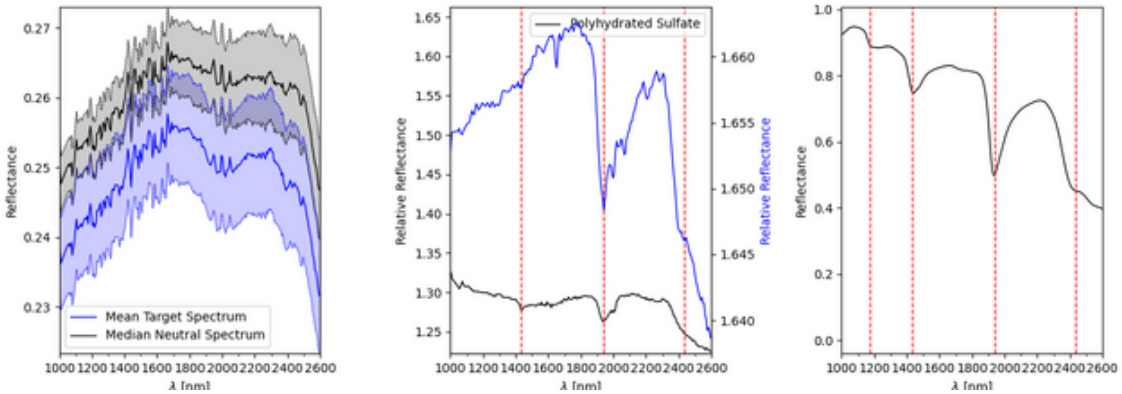

Figure 3.21: Spectral results for ROI HYD_1 of cube FRT00003e24. We associated this spectrum to polyhydrated sulfate.

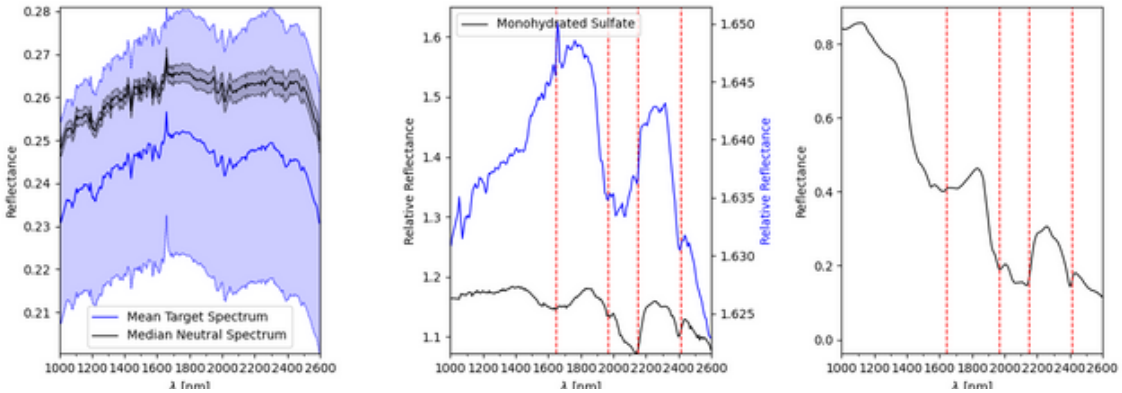

Figure 3.22: Spectral results for ROI HYD_2 of cube FRT00003e24. We associated this spectrum to monohydrated sulfate.

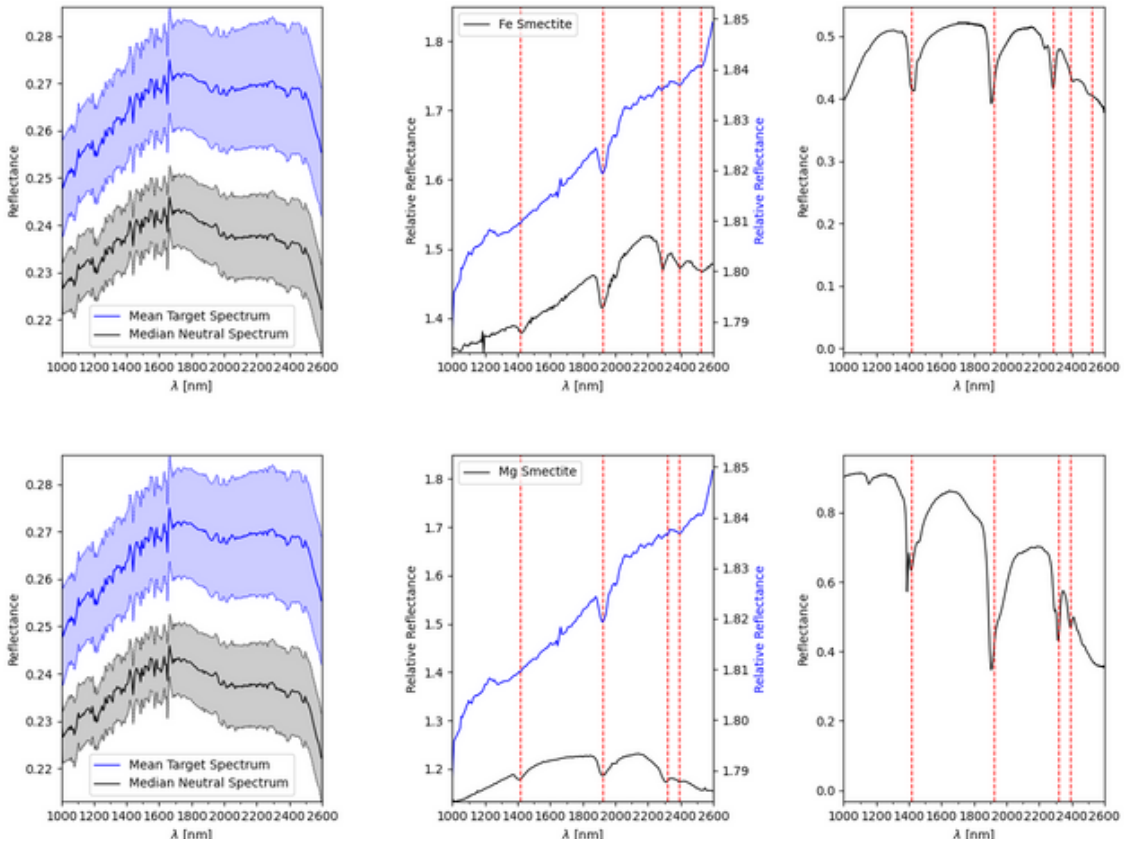

Figure 3.23: Spectral results for ROI HYD_3 of cube FRT00003e24. We associated this spectrum to a mix of Fe/Mg smectite.

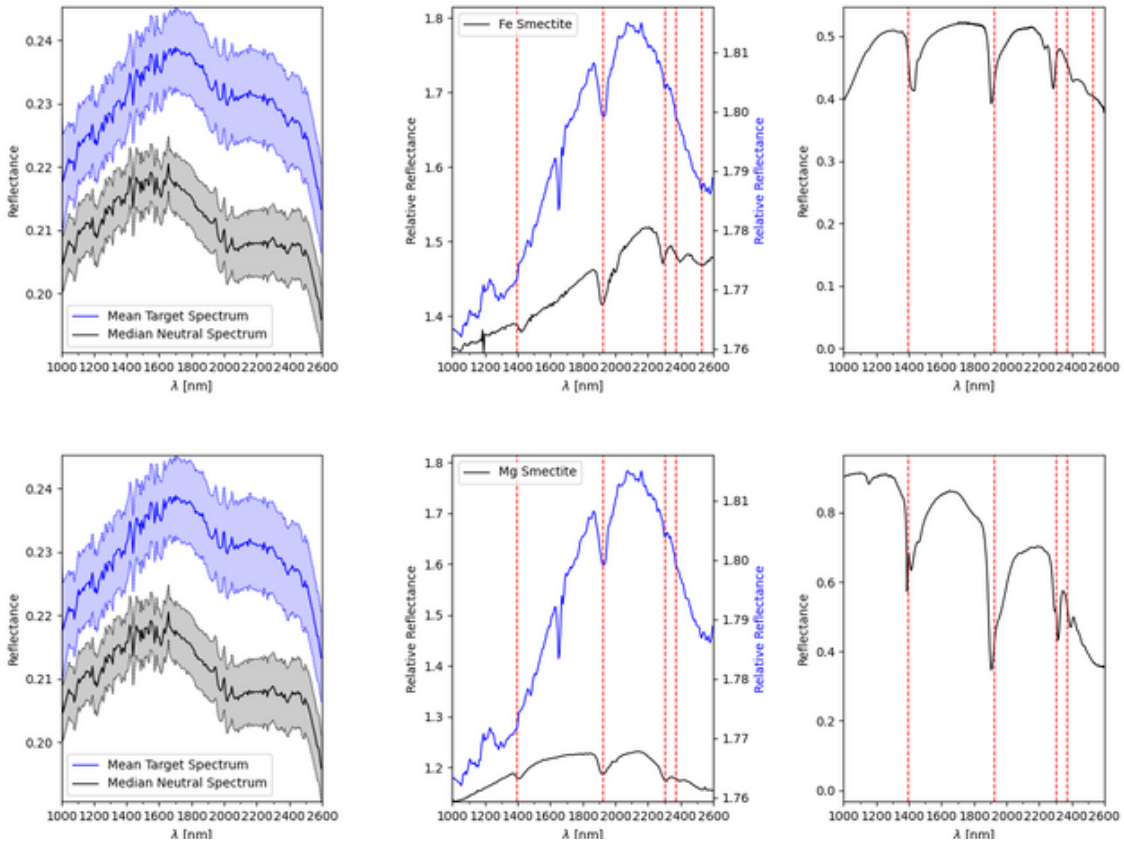

Figure 3.24: Spectral results for ROI HYD_4 of cube FRT00003e24. We associated this spectrum to a mix of Fe/Mg smectite.

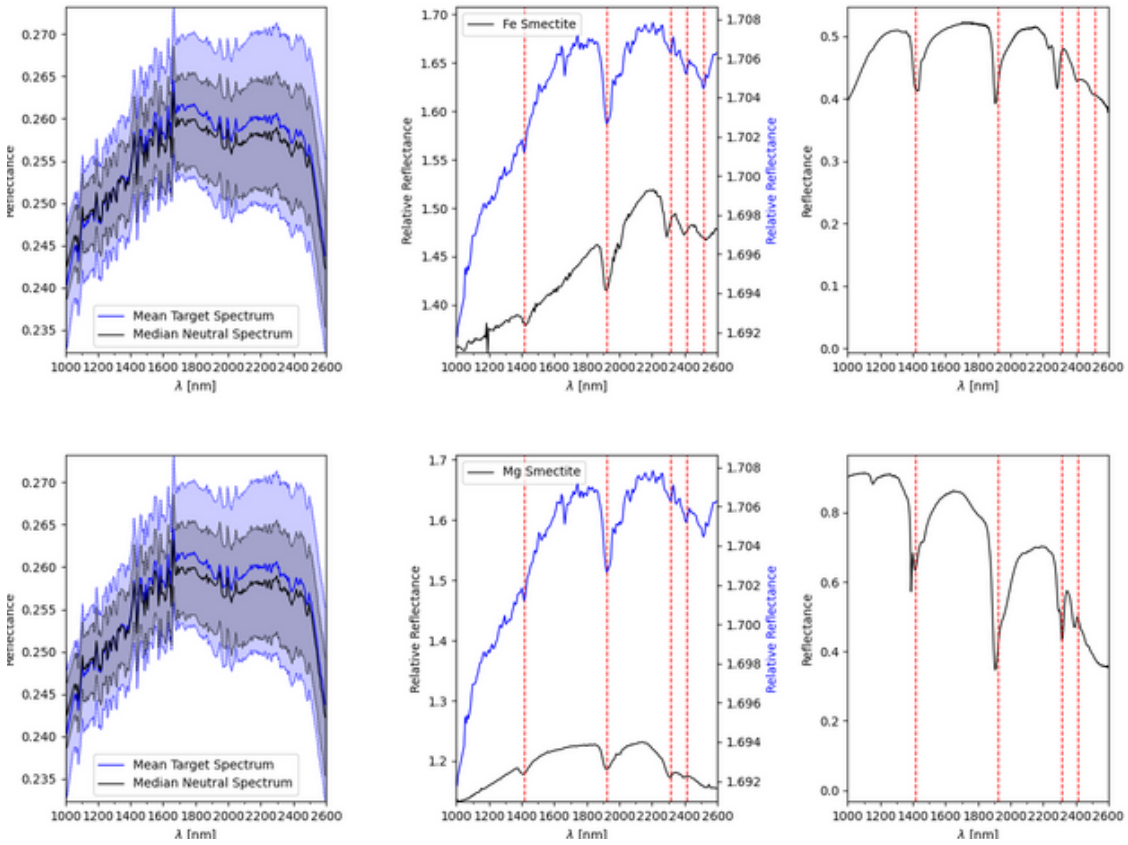

Figure 3.25: Spectral results for ROI HYD_5 of cube FRT00003e24. We associated this spectrum to a mix of Fe/Mg smectite.

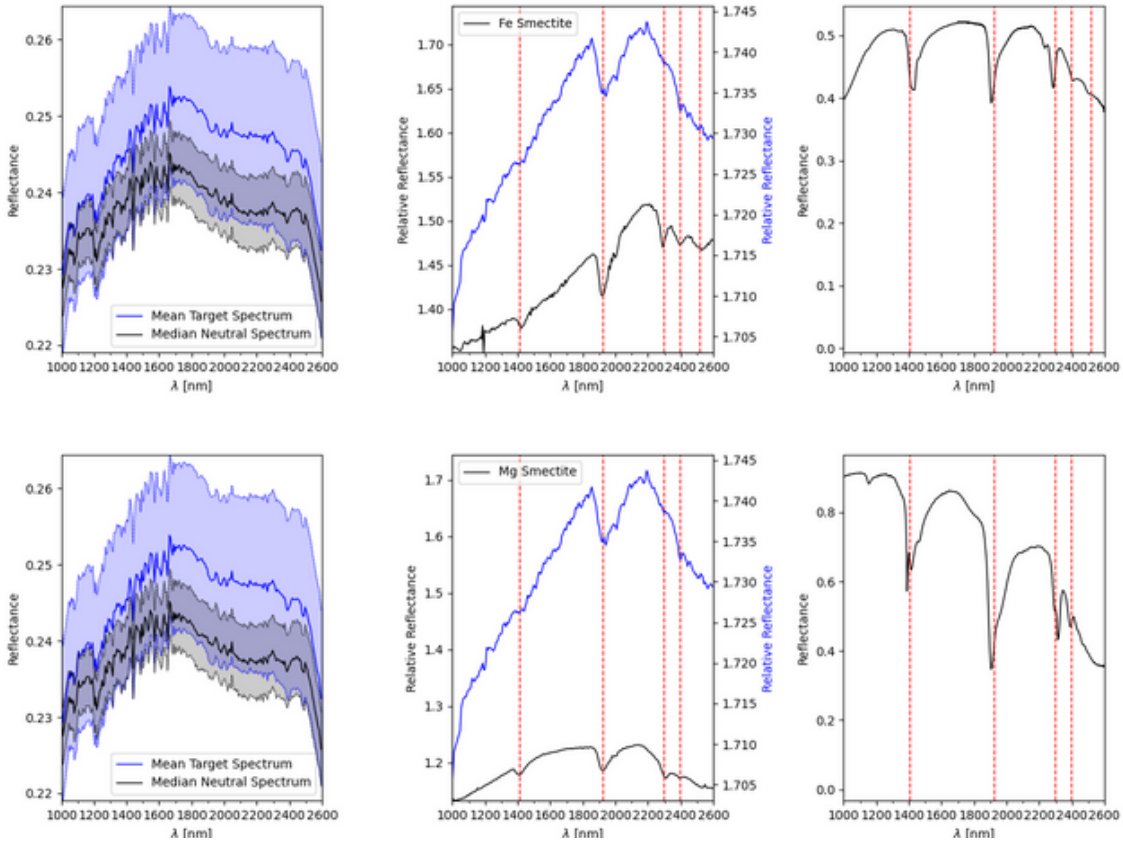

Figure 3.26: Spectral results for ROI HYD_6 of cube FRT00003e24. We associated this spectrum to a mix of Fe/Mg smectite.

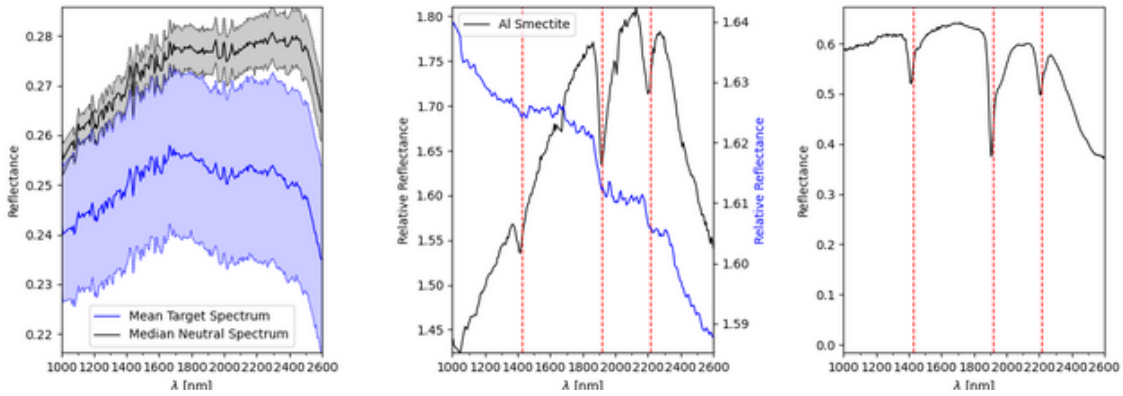

Figure 3.27: Spectral results for ROI PHY_1 of cube FRT00003e24. We associated this spectrum to Al smectite.

Table 3.8: Summary table of the spectral analysis results for each ROI. On the first column there is the detect mineral, the second column stores the certified CRISM lines as given from (MICA, 2019), the second column stores the laboratory absorption, always as given by (MICA, 2019) and the last one stores our detected absorption lines.

	Mineral	MICA Abs. [nm]	Lab. Abs. [nm]	Target Abs. [nm]
HYD_1	Polyhydrated Sulfate	X, 1430, 1940, 2430	1180, 1440, 1940, 2420	1171.73, 1434.31, 1941.25, 2436.92
HYD_2	Monohydrated Sulfate	1630, 1970, 2140, 2400	1620, 1970, 2140, 2400	1644.74, 1967.64, 2145.9, 2410.44
HYD_3	Mg Smectite	1410, 1920, 2310, 2390	1390, 1910, 2320, 2390	1414.59, 1921.46, 2317.79, 2390.58
	Fe Smectite	1420, 1910, 2290, 2390, 2520	1420, 1900, 2230, 2280, 2410, 2500	1414.59, 1921.46, 2284.72, 2390.58, 2522.92
HYD_4	Mg Smectite	1410, 1920, 2310, 2390	1390, 1910, 2320, 2390	1394.89, 1921.46, 2304.56, 2370.72
	Fe Smectite	1420, 1910, 2290, 2390, 2520	1420, 1900, 2230, 2280, 2410, 2500	1394.89, 1921.46, 2304.56, 2370.72, 2529.51
HYD_5	Mg Smectite	1410, 1920, 2310, 2390	1390, 1910, 2320, 2390	1414.59, 1921.46, 2311.18, 2410.44
	Fe Smectite	1420, 1910, 2290, 2390, 2520	1420, 1900, 2230, 2280, 2410, 2500	1414.59, 1921.46, 2311.18, 2410.44, 2516.32
HYD_6	Mg Smectite	1410, 1920, 2310, 2390	1390, 1910, 2320, 2390	1408.02, 1921.46, 2297.95, 2397.2
	Fe Smectite	1420, 1910, 2290, 2390, 2520	1420, 1900, 2230, 2280, 2410, 2500	1408.02, 1921.46, 2297.95, 2397.2, 2516.32
PHY_1	Al Smectite	1410, 1910, 2200	1410, 1910, 2210	1427.73, 1914.87, 2211.99

3.1.3 FRT0000062E6

From this cube we selected 5 different ROIs: 4 using the HYD RGB map as guideline and 1 using the PFM RGB map (see figure 3.28 to see all the RGB maps generated for this cube and table 3.9 to see the stretch values for each map). The minerals identified are Iron, Magnesium and Aluminium smectites, polyhydrated and monohydrated sulfates and talc.
The ROIs were named progressively pertaining to the parent RGB map: HYD_1, HYD_2, HYD_3, HYD_4 and PFM_1. The ROIs named HYD_1 revealed a composition of polyhydrated Sulfate, while the ROIs HYD_2 and HYD_3 revealed the presence of monohydrated sulfate.
The other ROIs revealed a phyllosilicates related mineralogy, in particular HYD_4 shows a composition of Mg/Fe smectite mixed some Al smectite, while PFM_1 reveals a composition of talc.
In table 3.10 the total number of spectra extracted from each ROI is presented, together with the total number of spectra used for the neutral spectra using the polygon method.
Lastly, in figure 3.29 we present all the ROIs selected for this cube and in figure 3.30 we present the neutral polygons chosen for the normalization corresponding to each ROI.

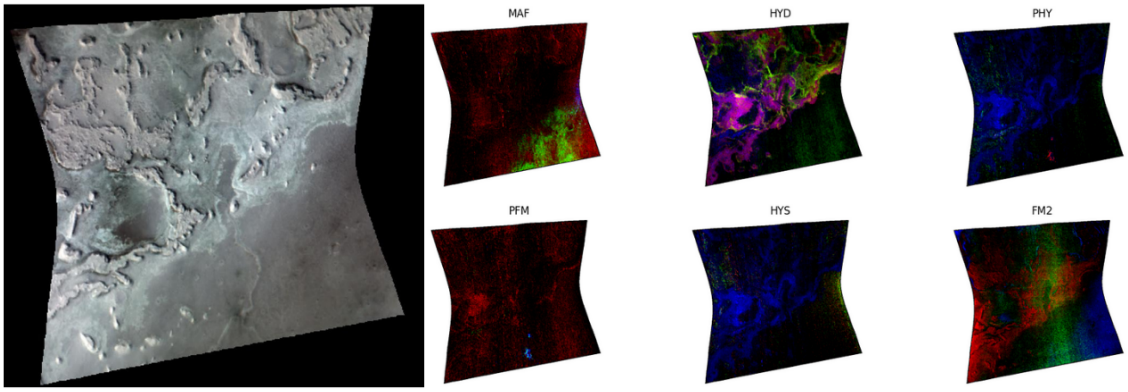

Figure 3.28: Generated RGB maps for the cube FRT000062e6. The false color image is absent due to the fact that it does not clearly represents spectral features

Table 3.9: Stretch values for the FRT000062e6 RGB maps.

	Rmin	Rmax	Gmin	Gmax	Bmin	Bmax
FAL	0.169	0.3388	0.2038	0.3215	0.2002	0.3002
MAF	0.0636	0.0975	0	0.0066	0	0.0027
HYD	0.0089	0.0249	0.0038	0.0145	0	0.0159
PHY	0	0.0004	0	0.0033	0	0.018
PFM	0.003	0.0079	0	0.0004	0	0.001
HYS	0	0.0025	0	0.003	0	0.0181
FM2	0.183	0.2103	0	0.01	0.0111	0.015

Table 3.10: Total number of spectra used for the mean target spectra and neutral spectra used for the median neutral spectra listed for each ROI.

	Target spectra	Neutral spectra
HYD_1	2735	2816
HYD_2	569	4697
HYD_3	6576	15321
HYD_4	1279	6545
PFM_1	1021	1888

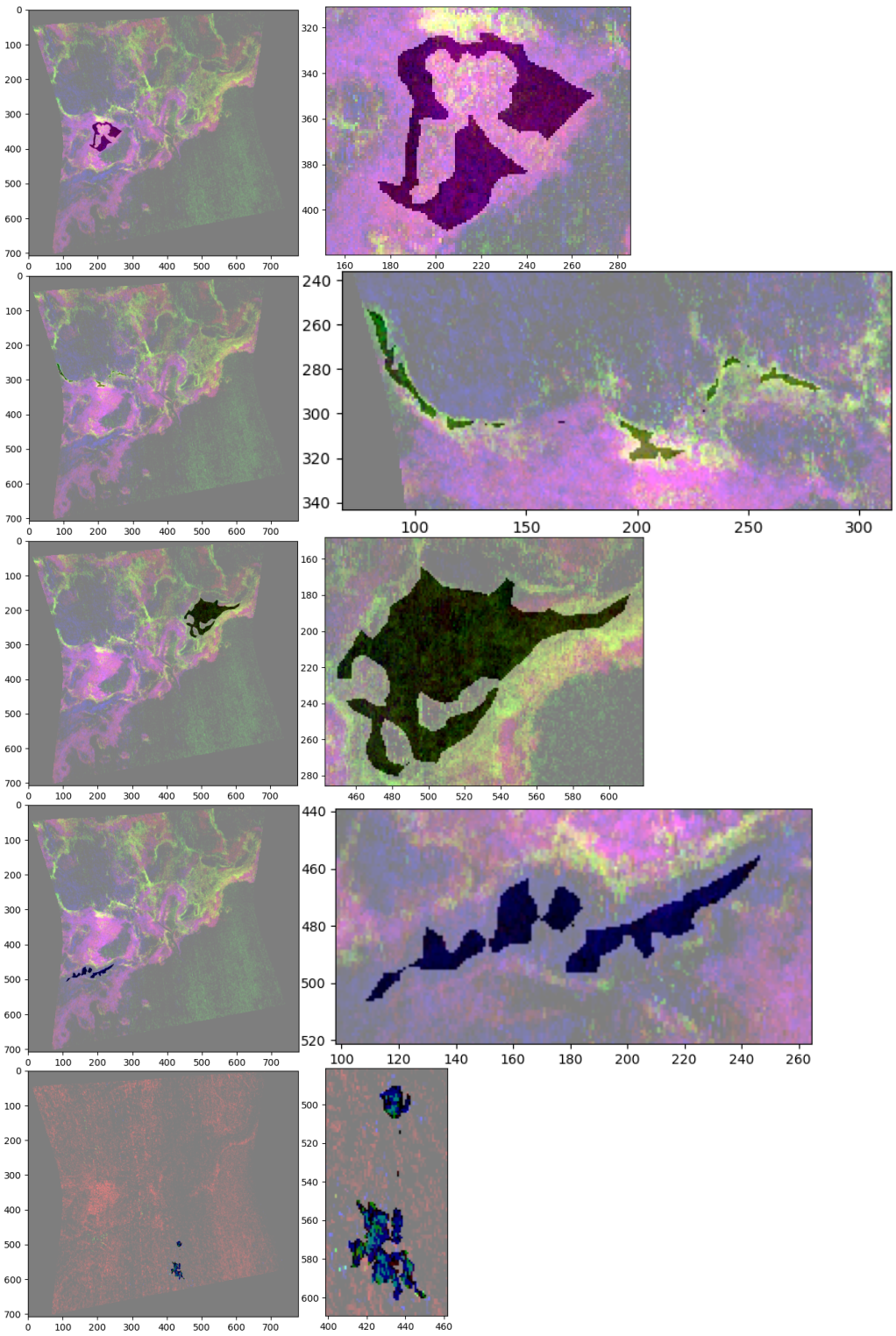

Figure 3.29: Selected ROIs for the cube FRT000062e6. On the right there is position of the ROI on the global scale of the CRISM cube while, on the left, there is the detailed vision of the ROI. From top to bottom are presented the ROIs in the following order: HYD_1, HYD_2, HYD_3, HYD_4 and PFM_1.

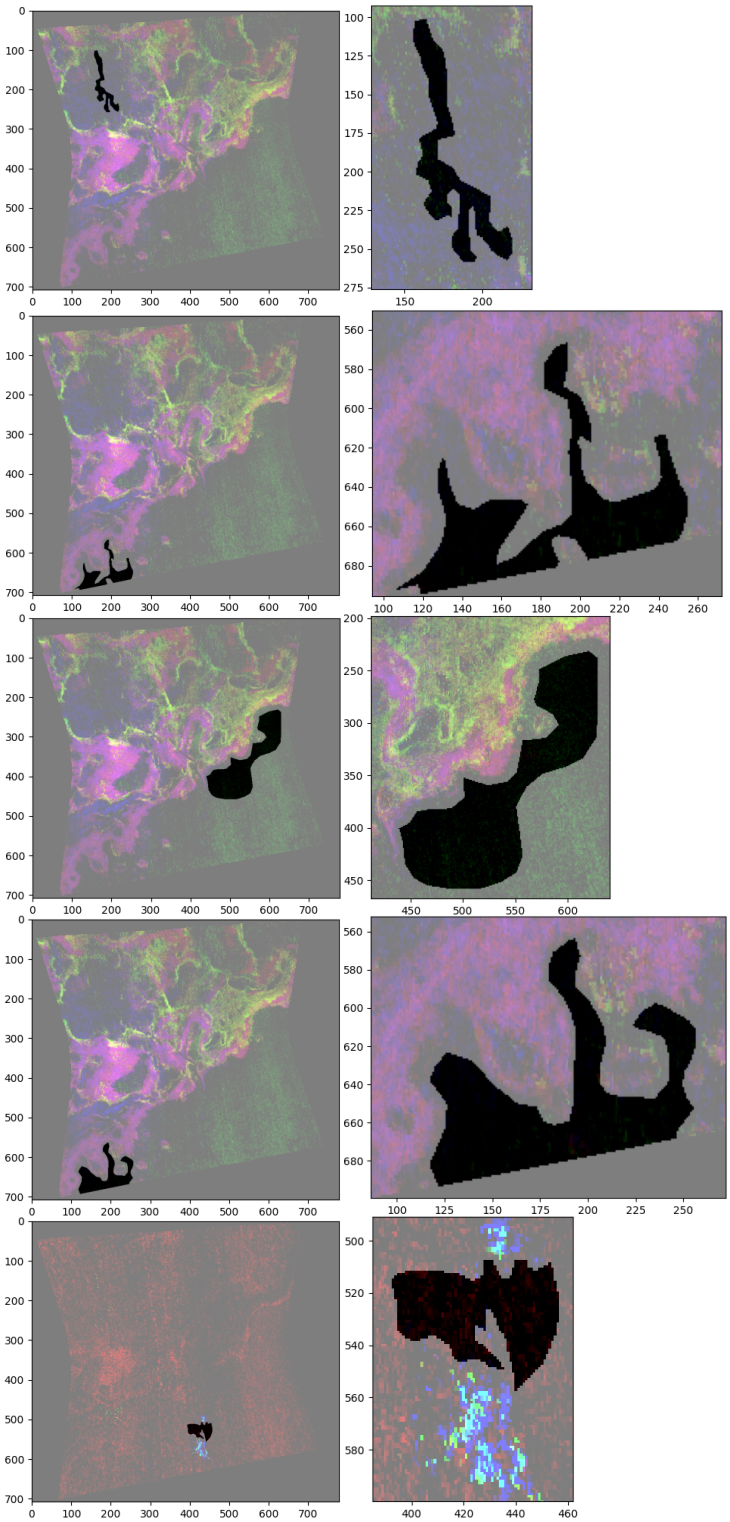

Figure 3.30: Selected neutral ROIs for the cube FRT000062e6. On the right there is position of the neutral ROI on the global scale of the CRISM cube while, on the left, there is the detailed vision of the neutral ROI. From top to bottom are presented the neutral ROIs in the following order: HYD_1, HYD_2, HYD_3, HYD_4 and PFM_1.

For all spectra the confronted mineralogy is given in the legend of the second plot and the resulting lines and associated mineralogy are shown in table 3.11.
In this cube we have found mineralogies similar to the previous two areas, finding both polyhydrated and monohydrated sulfates, Al/Mg/Fe smectites and talc.
We have found polyhydrated sulfate in ROI HYD_1 (see figure 3.31), in which the water-related absorptions at ~1940 nm and ~2430 are clearly visible. The absorptions at ~1180 nm and ~1430 nm are not celarly visible, this might be due to a slope effect or due to noise obscuring the signal. Also the shape is kind of different from the certified CRISM/laboratory ones, but it is probably due to slope issues from the ratioing operation.
In ROIs HYD_2 and HYD_3 we have a clear signature monohydrated sulfates (see figures 3.32 and 3.33) from the water-related absorption bands around 2100 nm and 2400 nm. Fro HYD_2 The broad absorption centered around 1620 nm is not visible in our spectra and this could be partly related to noise-related problems caused by a bad erasure of the artifact between 1650 nm and 1750 nm (caused by the overlap of two filters), and indeed the spike related to this artifact is visible around 1650 nm in figure 3.32. For HYD_3 we have a slope related issue as our ratioed spectrum reveals an upward trend because of the shape of the neutral spectra we chose. Anyway, the broad band between 1800 nm and 2200 nm that contains the absorption lines at ~1970 nm and ~2140 nm is still well visible and also the other two absorptions around 1620 nm and 2400 nm are well visible even if the first one is not as broad as it should be, but, again, this could be due to ratioing/slope issues.
Regarding the last two ROIs, they revealed a Phyllosilicate-related composition: HYD_4 gave a main composition of mixed Mg/Fe Smectite, as it is clear from the last two figures in 3.34. Also, the presence of Al Smectite is recognizable from the small absorption located near 2200 nm.
Lastly, PFM_1 (see figure 3.35) reveals a spectrum that is related to talc, both shape and absorption features match the certified CRISM/laboratory Talc spectrum. We have all the absorption lines well in accordance with the laboratory and CRISM ones, with the exception of the one near 1400 nm for which we have a ~18 nm of discrepancy. In talc this line is narrow from the lack of H_2O and it is instead given usually by the OH bond (Clark et al., 1990). Since ours is slightly more similar to values associated to smectites, the shift could be just related to some water presence inside the talc crystalline structure or to a mixing with smectites. In general, to see what component in the mineral causes the observed absorption see table 3.2.

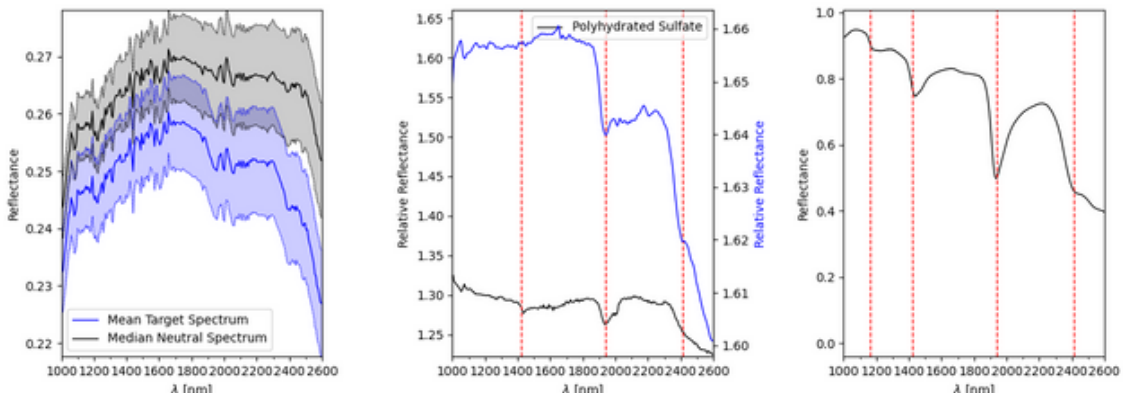

Figure 3.31: Spectral results for ROI HYD_1 of cube FRT000062e6. We associated this ROI to polyhydrated sulfate.

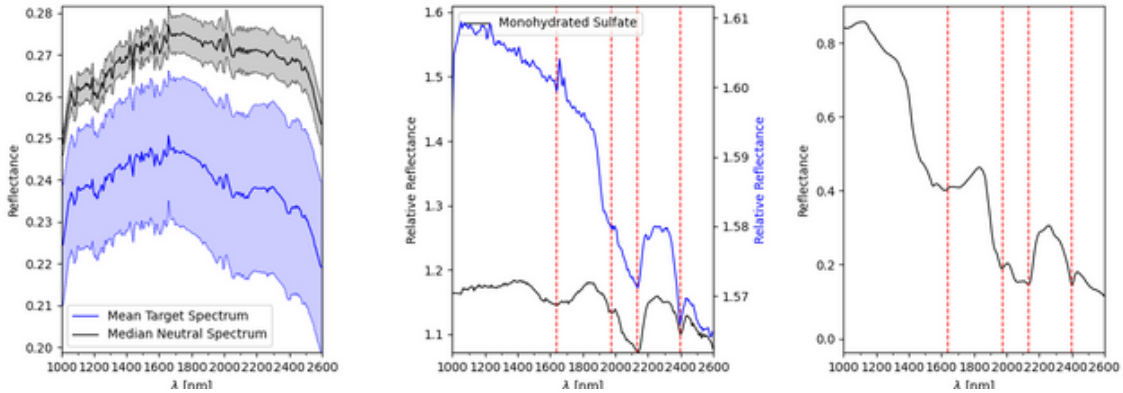

Figure 3.32: Spectral results for ROI HYD_2 of cube FRT000062e6. We associated this ROI to monohydrated sulfate.

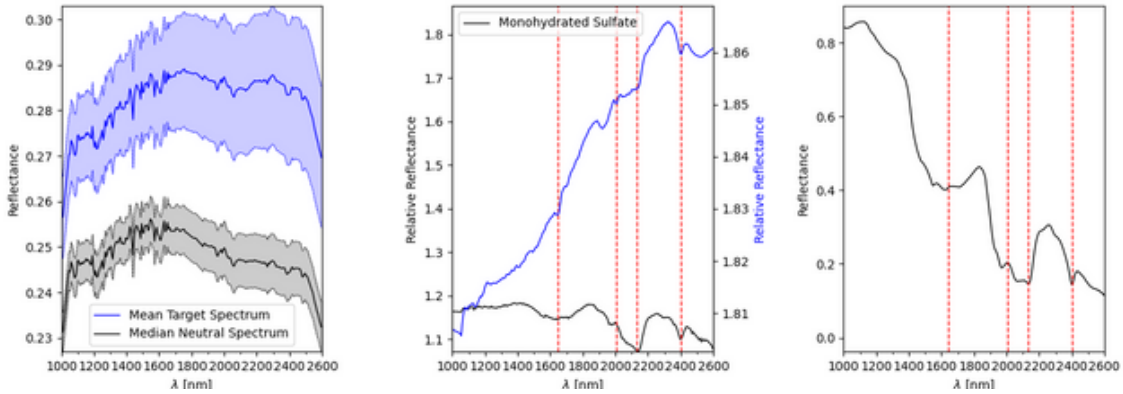

Figure 3.33: Spectral results for ROI HYD_3 of cube FRT000062e6. We associated this ROI to monohydrated sulfate.

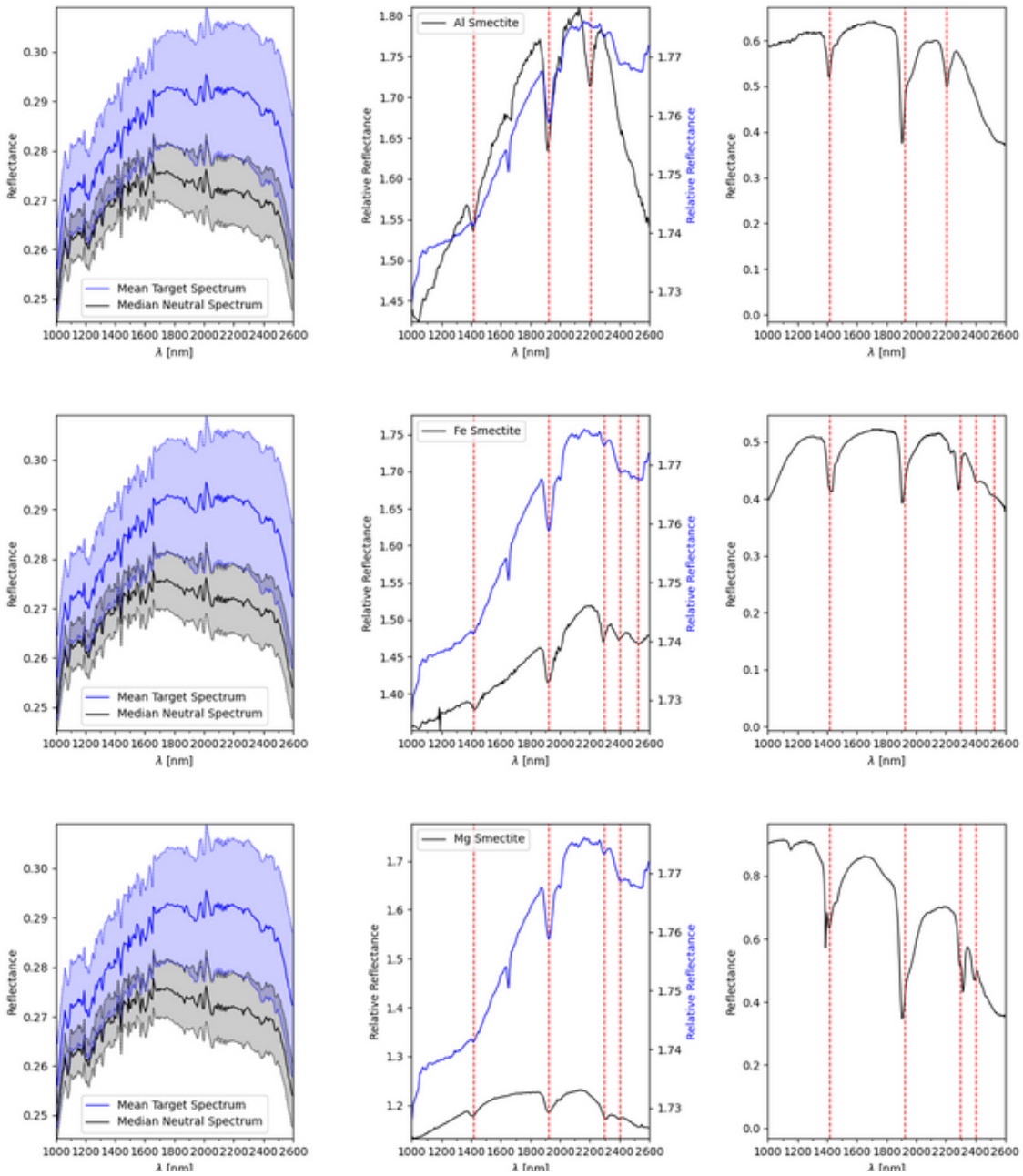

Figure 3.34: Spectral results for ROI HYD_4 of cube FRT000062e6. We associated this ROI to a mix of Al/Mg/Fe smectite.

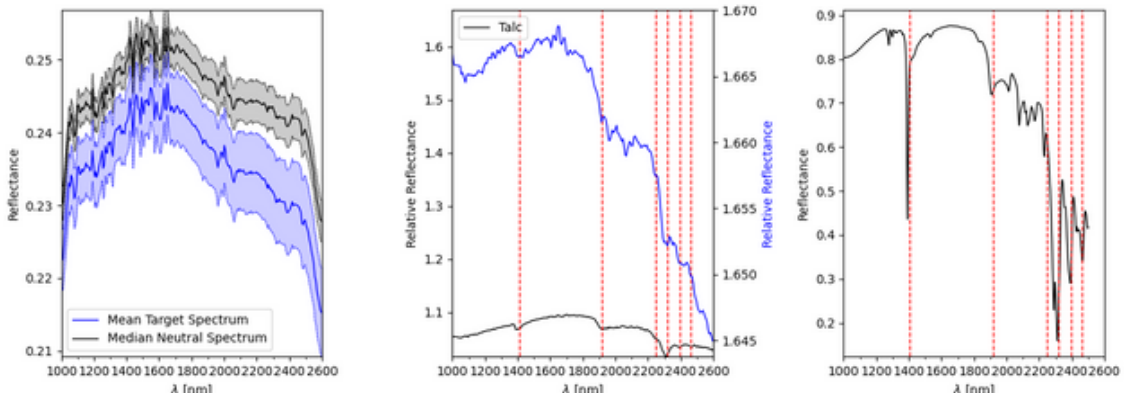

Figure 3.35: Spectral results for ROI PFM_1 of cube FRT000062e6. We associated this ROI to talc.

Table 3.11: Summary table of the spectral analysis results for each ROI. On the first column there is the detect mineral, the second column stores the certified CRISM lines as given from (MICA, 2019), the second column stores the laboratory absorption, always as given by (MICA, 2019) and the last one stores our detected absorption lines.

	Mineral	MICA Abs. [nm]	Lab. Abs. [nm]	Target Abs. [nm]
HYD_1	Polyhydrated Sulfate	X, 1430, 1940, 2430	1180, 1440, 1940, 2420	1165.18, 1421.16, 1941.25, 2410.44
HYD_2	Monohydrated Sulfate	1630, 1970, 2140, 2400	1620, 1970, 2140, 2400	1638.16, 1974.24, 2132.69, 2397.2
HDY_3	Monohydrated Sulfate	1630, 1970, 2140, 2400	1620, 1970, 2140, 2400	1638.16, 1974.24, 2132.69, 2397.2
HDY_4	Al Smectite	1410, 1910, 2200	1410, 1910, 2210	1414.59, 1921.46, 2205.38
	Mg Smectite	1410, 1920, 2310, 2390	1390, 1910, 2320, 2390	1414.59, 1921.46, 2297.95, 2403.82
	Fe Smectite	1420, 1910, 2290, 2390, 2520	1420, 1900, 2230, 2280, 2410, 2500	1414.59, 1921.46, 2297.95, 2403.82, 2522.92
PFM_1	Mg Smectite	1410, 1920, 2310, 2390	1390, 1910, 2320, 2390	1408.02, 1914.87, 2317.79, 2397.2
	Fe Smectite	1420, 1910, 2290, 2390, 2520	1420, 1900, 2230, 2280, 2410, 2500	1427.73, 1914.87, 2297.95, 2397.2, 2522.92
	Talc	1390, 1910, 2240, 2310, 2390, 2470	1390, 1910, 2230, 2320, 2390, 2470	1408.02, 1914.87, 2245.04, 2317.79, 2397.2, 2463.41

4

Discussion and Interpretation of Results

4.1 Local Interpretation

4.1.1 FRT00009B5A

This cube spans three different geological units from the map of (Hynek and Di Achille, 2017): the infilled crater's floor pertains to the $HNme_u$, the crater rim is obviously older than the infilling and is classified as being part of c_1 and the outside belongs to Nhc_1 (see figures in figures 1.7 and 1.9 for context). Our CRISM datacube covers only the northern portion of the crater, in figure 4.1 we present a full view of this peculiar crater, with our projected false color image in evidence.

Kai is a small crater ~20 km in diameter. Its southern rim seems slightly more eroded than the northern one and from its deepest point in the floor to highest point on the rim is ~500 m in difference (see figure 4.2 and the second and third figures in figure 4.6). The floor of Kai is filled with various debris and sediments and, from our spectral analysis, part of these materials are rich in Fe/Mg smectites. Moreover the floor of Kai is interested by various small mounds of not clear origin, implying a complex story of underground fluid circulation. The crater presents lots of other well distinguishable features and from our area covered by CRISM the first one that stands out is the rhythmic layering in the northern portion of the crater floor (see figure 4.3 to see a detail). From our spectral analysis, which was targeted at the dark area that cuts these layers, we have found presence of polyhydrated and monohydrated sulfates, which appear re-

spectively magenta and yellow in the HYD RGB image. The left image shown in figure 4.4, shows that the same magenta colors are also found in association with the rhythmic layering, suggesting that these layers may also have a polyhydrated sulfate composition. These layers are alternated with layers which appear darker/blue in the HYD RGB image, meaning they could contain other hydrated minerals such as phyllosilicates. However, the detailed spectral analysis of these layers was not carried out in this thesis as it's currently the subject of another project by (Baschetti et al., 2023). Finally, these layers seem to descend for ~150 m towards Northeast before stopping at the border with the dark unit on the left of our CRISM cube (see the first figure in figure 4.6. Combining spectral results with high resolution DEMs from HiRISE and CTX it is possible to investigate the stratigraphic relationships of the various mineralogical units in the cube, especially on the rim, in which we have chosen the ROIs (HYD_3, PHY_1 and PHY_3) from the lowest to the highest in elevation. Based on what we have said and shown in Chapter 3.1.1, and knowing the relative altitude of the ROIs, it seems clear that on the rim we have a shift from Fe/Mg mineralogy to more Mg mineralogy for the smectites, and then we observe Talc on top of that (see fig 4.8). Moving our attention on the crater floor we see that monohydrated and polyhydrated sulfates have a lower elevation with respect to the Fe smectites. Regarding the last ROI, which was taken outiside of the crater, due to the lack of HiRISE coverage, it is difficult to understand if the formation that shows the Al smectite composition is part of Kai's ejecta or if it formed at a later stage. To see a schematic view of the stratigraphic relationship between the minerals, divided based on the geological unit they belong to, see figure 4.5. Overall, Kai is surely full of information about aqueous processes and further analysis should be conducted regarding it and especially regarding the layers. At last, it is important to clearly say that, since in the crater's floor we observe phyllosilicates on top of clays, this crater surely needs more accurate and more extended analysis. This is due to the fact that, classically, being phyllosilicates associated with Noachian terrains and sulfates associated with Hesperian terrains (Bibring and OMEGA Team, 2006), we should have expected to see the inverted relation, so sulfates on top of the phyllosilicates.

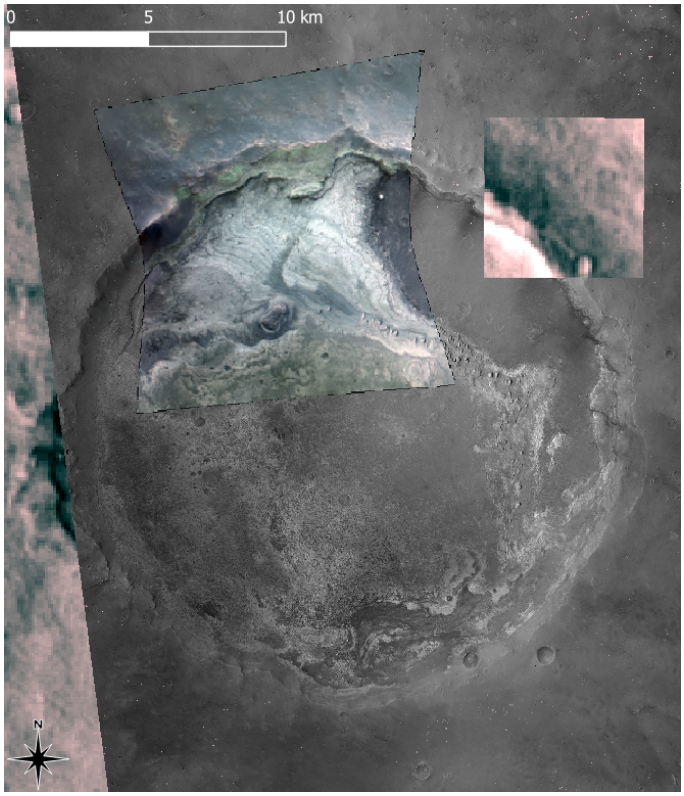

Figure 4.1: Full view of Kai crater. The CRISM cube is located in northern portion of the area. The underlying images are the CTX and THEMIS thermal inertia image, which is given in (Hynek and Di Achille, 2017).

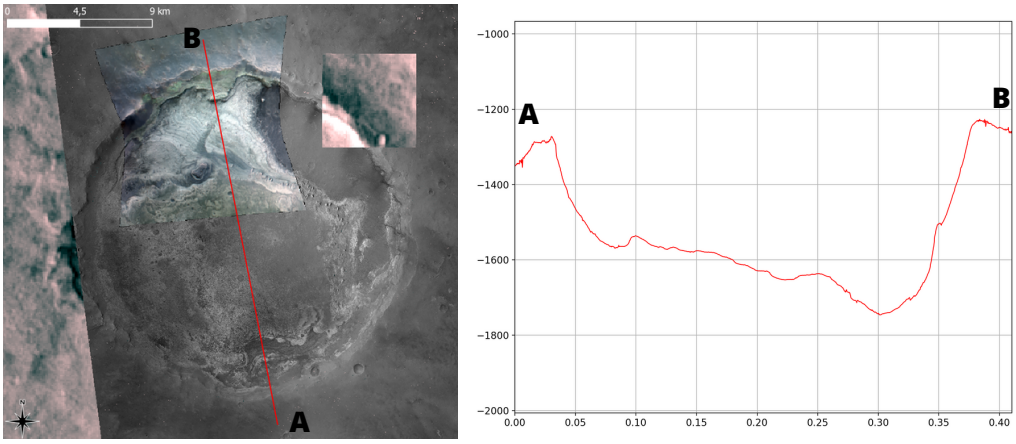

Figure 4.2: Altitude profile of the Kai crater. It is easy to see that the deepest point of the crater is where the layers encounter the darker area on the left of the image.

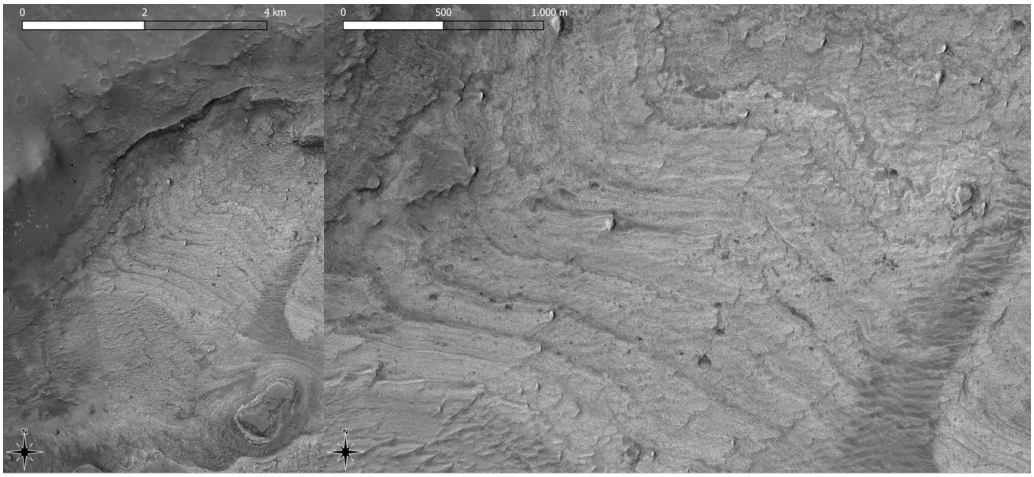

Figure 4.3: Detailed vision of the layers in the Northern floor of Kai crater. The image was taken by the HiRISE camera.

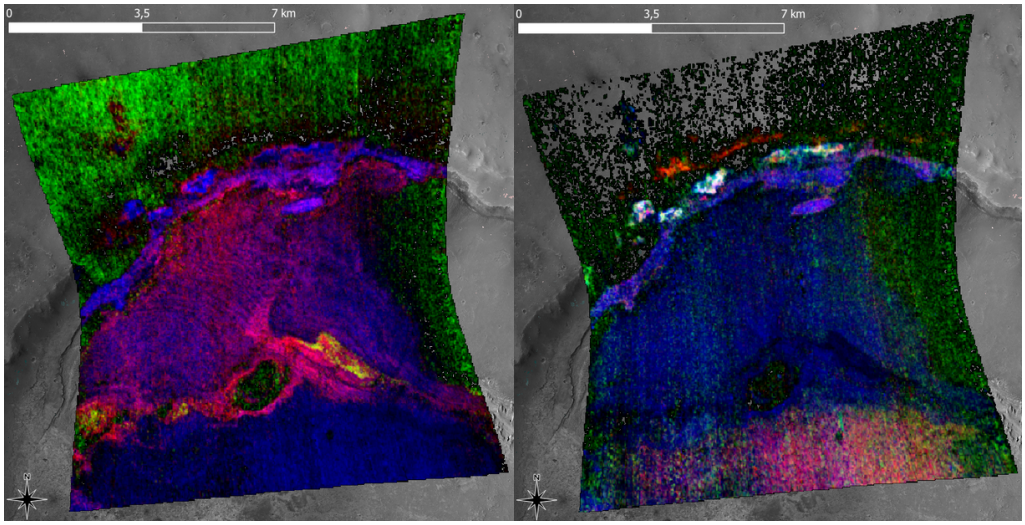

Figure 4.4: CRISM Hydrated minerals RGB map on the left and phyllosilicates RGB map on the right.

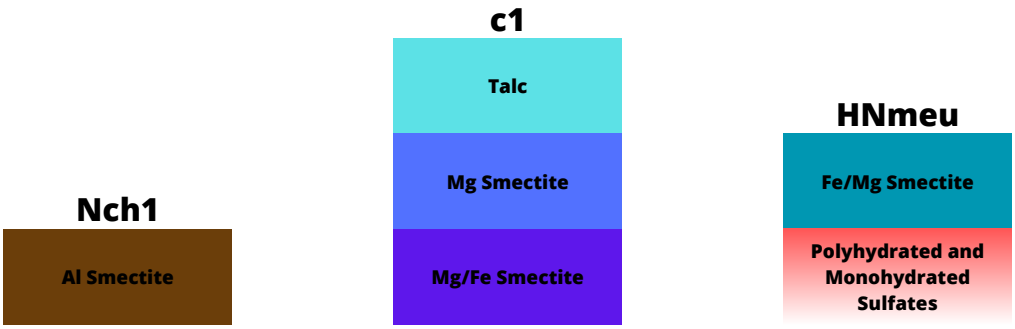

Figure 4.5: View of our identified stratigraphic units and their elevation relations. The strata are based on between the three geological units from (Hynek and Di Achille, 2017) that our CRISM cube spans (corresponding to crater floor, rim and outside). The strata are not to scale with each other and the image is made only to relate the geological units given by (Hynek and Di Achille, 2017) and the relative altitude between the minerals we have found.

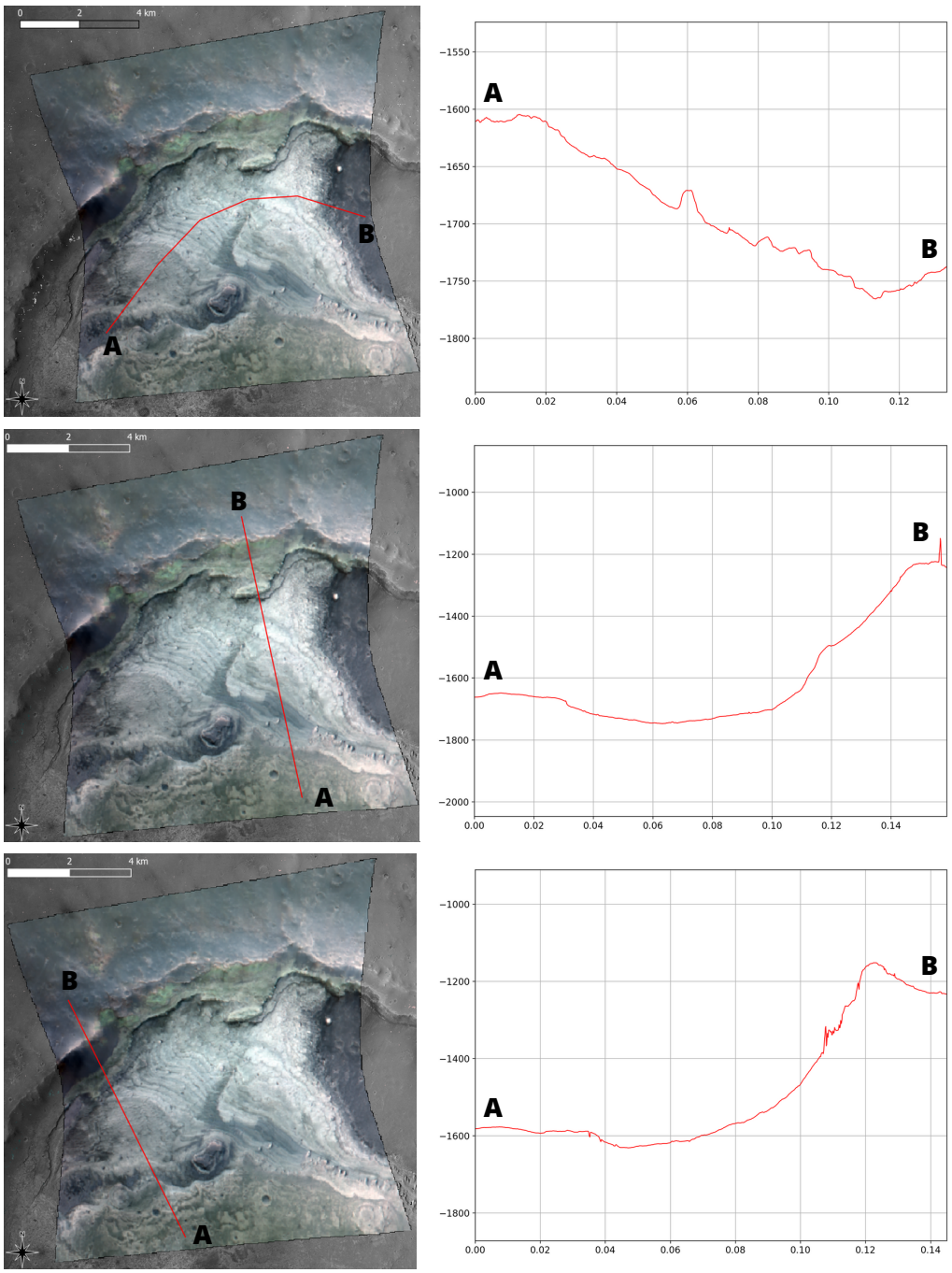

Figure 4.6: Selected profiles on the northern portion of Kai crater. From the first image it is possible to see how the layers proceed downward up to the border with the dark unit on the right. Moreover, from the last two it is easy to see how the the darker unit on the bottom, on which we have found the Fe/Mg smectites, is higher than the sulfate deposits and the layers.

4.1.2 FRT00003E24

This cube is placed in an area which is mapped as Nhc_1 in Hynek and Di Achille (2017), however, this was probably done since the unnamed crater depicted in the cube is smaller than the scale that was used to design the map.
In this area we have an oblique impact crater filled with layered sediments. The major diameter is of ~9 km and minor diameter of ~5 km. The two sides of the rim show major differences, being the Southwest one higher than the Northeast: from the two maximum altitudes we observe a 200 m difference (see figure 4.9 for the profiles and figure 4.10 for a 3D view of the crater). The infilling is almost flat in all the crater's floor with only the southeastern part being slightly higher than the opposing one (see figure 4.9 for the profiles and figure 4.8 for a detailed view of the layers). Always inside the crater, on the border between the rim and the floor, we

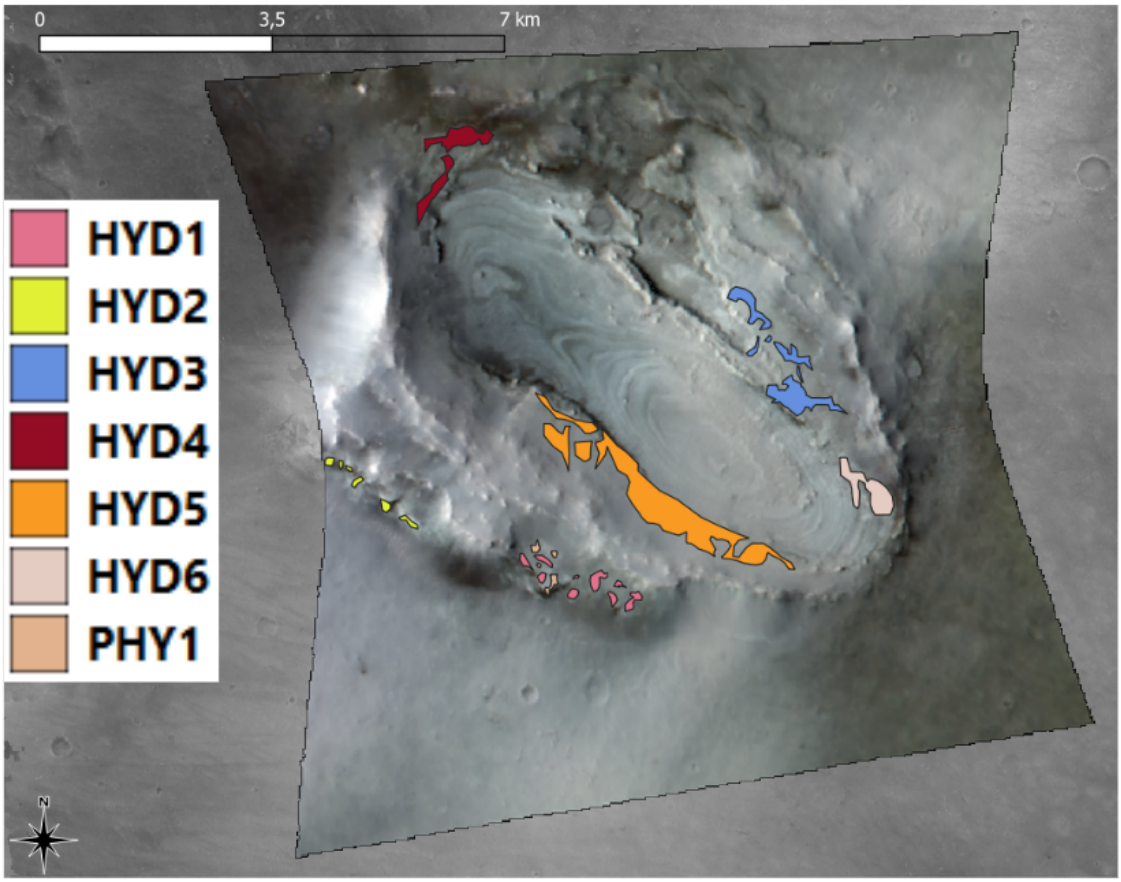

Figure 4.7: Projected false color image of the crater with all the associated ROIs.

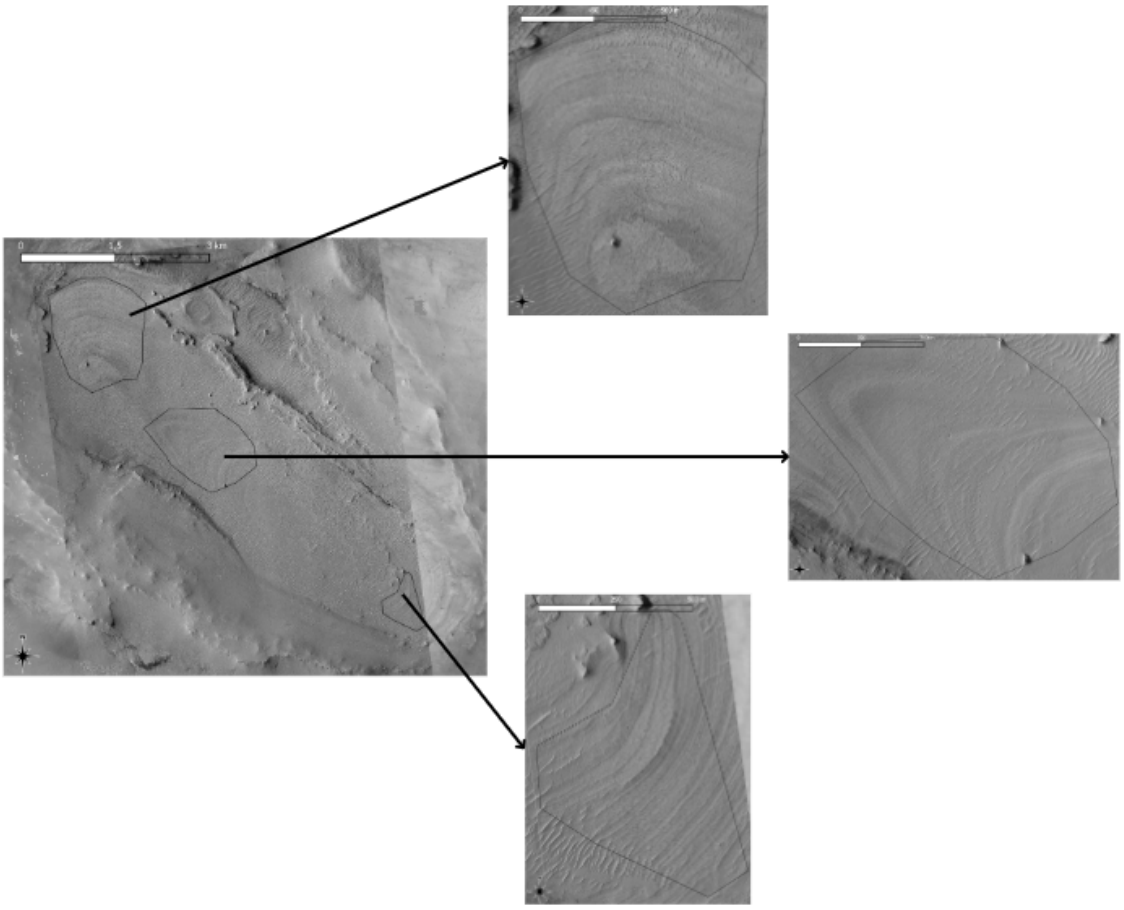

Figure 4.8: Detailed view of the layers. The high resolution image is the HiRISE image available for this zone.

have found presence of phyllosilicates as smectites of mixed composition between Magnesium and Iron (ROIs from HYD_3 to HYD_6, see figures 4.7 and 4.10).
Outside of the crater, on the Southwest outer rim we have found monohydrated sulfate, polyhydrated sulfate and Aluminium smectite (ROIs HYD_1, HYD_2 and PHY_1, see figures 4.7 and 4.10) all located around the same height. This is something peculiar, given that the formation condition of sulfates and phyllosilicates, as we have said in Chapter 1, are quite different as phyllosilicates forms in wetter environments than sulfates, that results mainly from evaporation processes.
From the morphological characteristic of the terrain, it seems safe to assume that on top of these sulfates deposits mafic material is present.
All of the above, and the general shape of the crater rim, points out to the possibility that

the crater formation gave rise to a flapping event (Roddy, 1976) (see figure 4.11 for a general schematic view): by impacting a terrain with two main stratigraphical units made, from top to bottom, of sulfates and basalts (see figure 4.12 A and B), the subsequent ejecta deposition could have inverted the stratigraphical disposition of these materials (see figure 4.12 C). Then, after the impact, the layered materials observed on the floor formed, and during wet events, we could have had the alteration of the flapped basalts in the phyllosilicates we see in the outer part of the floor/inner rim (see figure 4.12 D). This is also supported by the fact that we see polyhydrated sulfate deposits around the crater (colored in magenta, see the second figure of 4.10B), giving hints about the main composition of the surrounding terrain.

The layered features on the floor of the crater are similar to the ones found in Kai and are overlayed by several scattered dune fields (see figure 4.8).

The second image in figure 4.10 shows that the same magenta and blue colors are also found associated with the layers in the crater's floor, suggesting that these layers may be composed by alternation of polyhydrated sulfates and Mg/Fe smectites. As for the layers found in Kai, also these layers will be further analyzed in the project by (Baschetti et al., 2023). Anyway, these layers might have formed after the crater involving some kind of water-related process during which environments favouring sulfate deposition alternated with environments favouring phyllosilicate deposition.

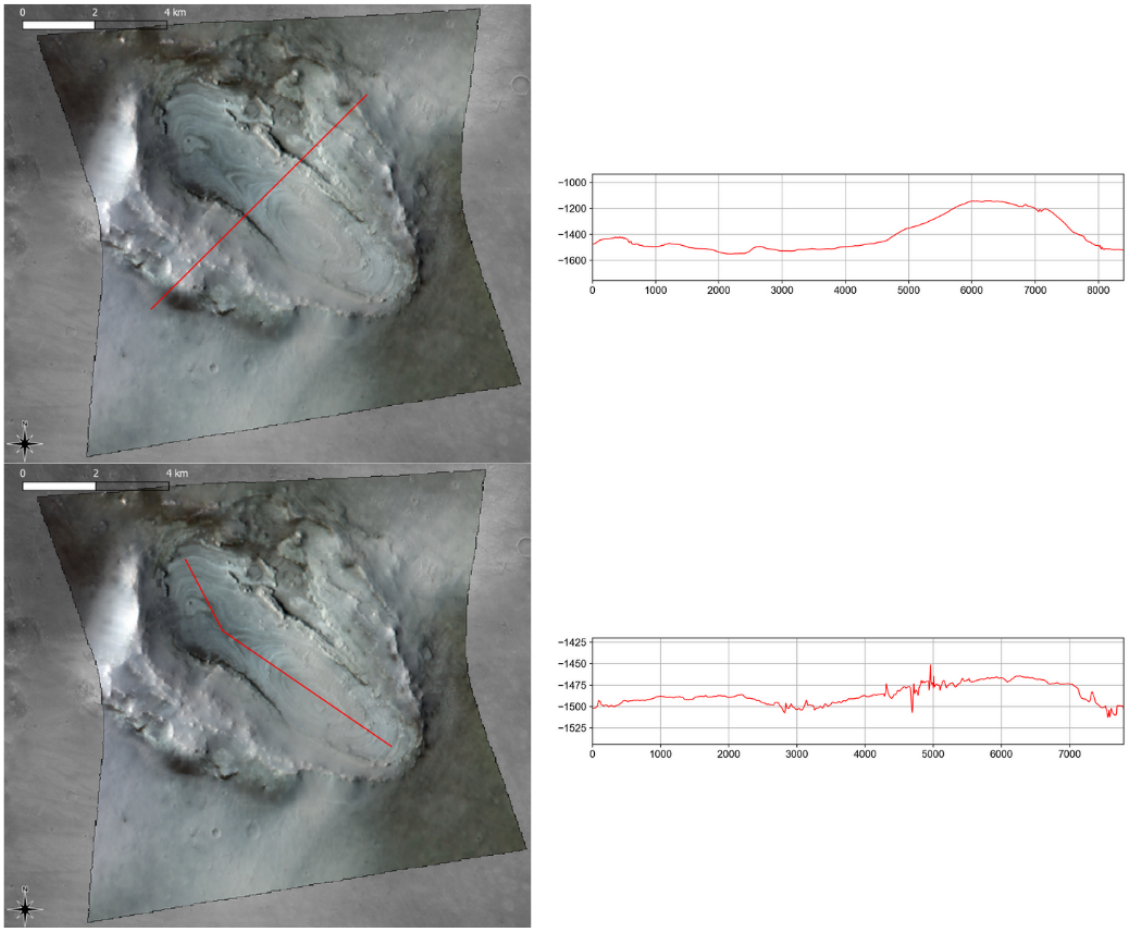

Figure 4.9: Selected profiles of the crater. The first one shows how the infilling is almost homogeneous in all the crater floor with only the southeastern part being slightly higher than the northwestern one. The second shows the difference in altitude between the two rim's sides. The profiles goes, respectively, from right to left and from up to down.

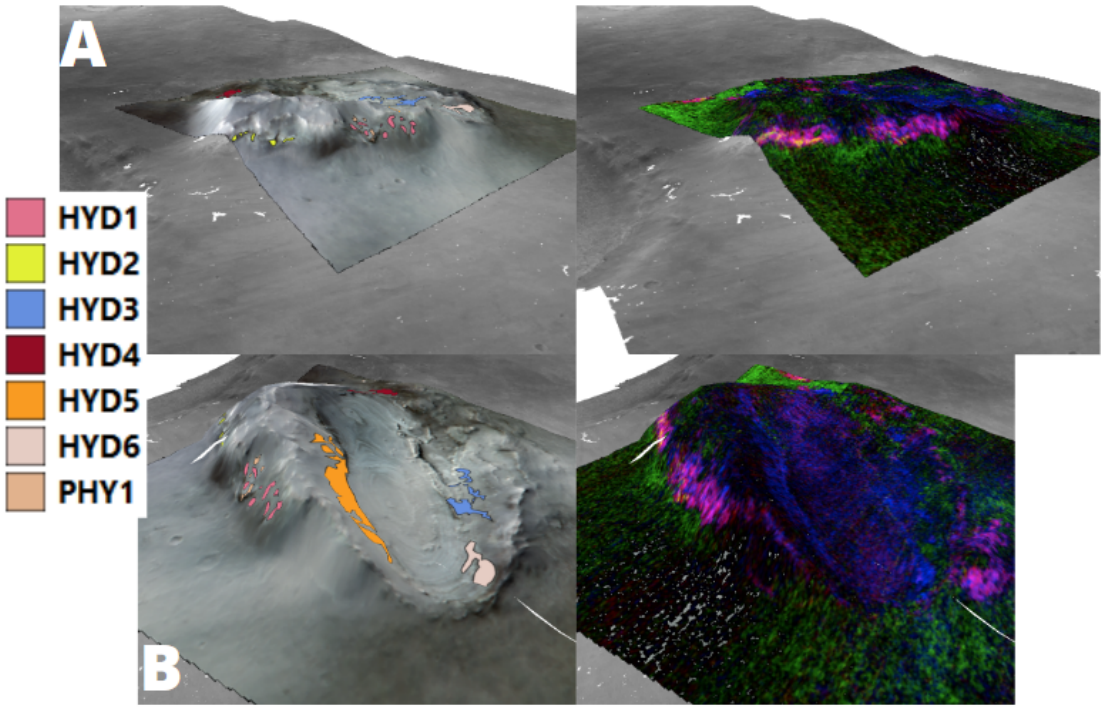

Figure 4.10: Selected 3D views of the crater. The row **A** hosts the 3D false color image with he selected ROIs and the HYD RGB map. These two images focuses on the Southwestern rim to highlight the fact that the sulfates and Al smectite deposits are on the same layer. The second **B** row hosts again the 3D false color image with the selected ROIs and the HYD RGB map but as seen from around the Southeastern rim to highlight the flatness of the crater's floor in comparison to the outside terrain. Moreover it highlights also that, following the HYD RGB map, the polyhydrated sulfates are found in other areas around the crater (magenta-colored areas), indicating that indeed flapping is a plausible hypothesis for the inversion of the stratigraphy. The height scale is exaggerated 4 times.

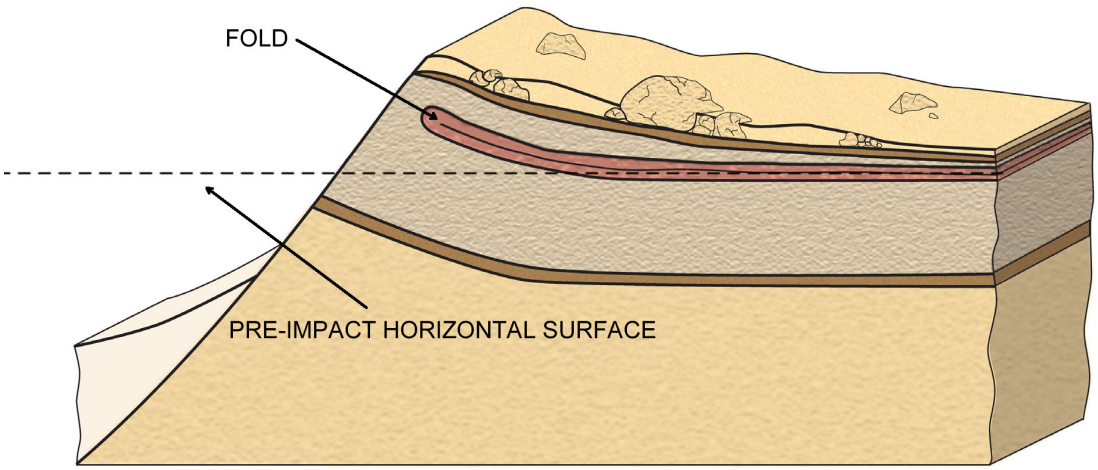

Figure 4.11: Schematic view of the flapping phenomenon: the ejecta resulting from the impact crater that excavated in a stratified terrain folds and inverts the stratigraphy. Credits: Guidebook to the Geology of Barringer Meteorite Crater, Arizona (a.k.a. Meteor Crater), ©2007, David A. Kring, Lunar and Planetary Institute. LPI Contribution No.1355.

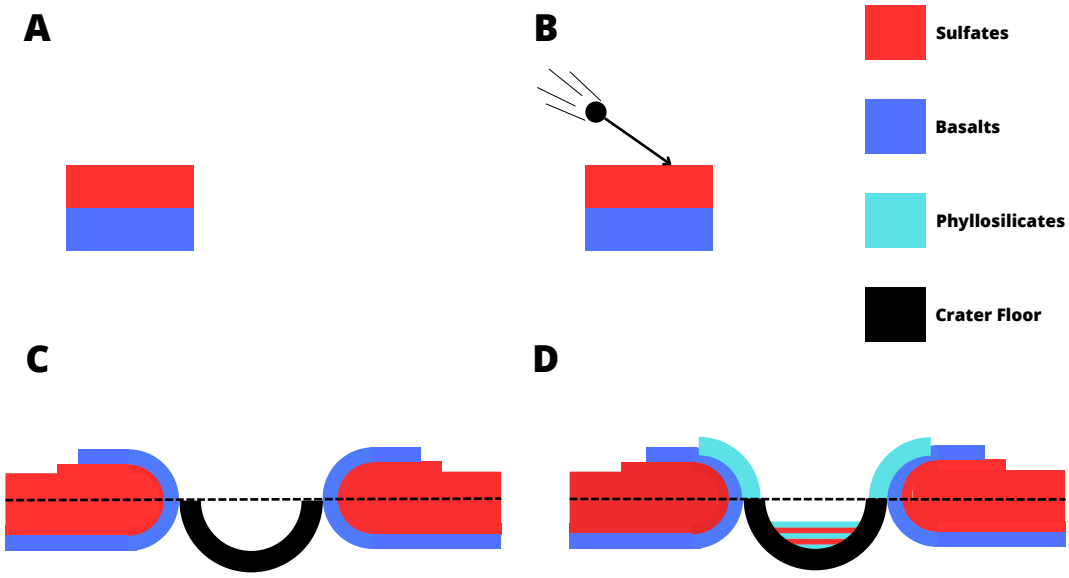

Figure 4.12: Hypothetical formation of the oblique crater:
A: previous impact stratigraphy;
B: the bolide impacts the stratified terrain;
C: the ejecta deposition inverts the stratigraphical relation;
D: alternated wet and dry events deposits the layers in the crater's floor and alter the basalts on the border.

4.1.3 FRT0000 62E6

This cube spans two different terrains, one being the Nhc_1 terrain and the other one being the $HNme_3$ terrain (the same that almost surrounds the Noachian unit) (Hynek and Di Achille, 2017).

The $HNme_3$ terrain is clearly defined by mounds and mesas interspersed by valleys, while the Nhc_1 terrain is smoother and it is crossed by an inverted channel. Inverted channels are thought to form as a consequence of erosional processes (fluvial, aeolian, etc) when a river bed has more resistance to the erosion than the surrounding environment, resulting so in the river bed being uplifted in comparison to the new surroundings (see figure 4.13, up) (Zaki et al., 2021). Inverted channels can be either contiguous or superimposed. This difference determine the stratigraphical relation between the channels, indicating if two, or more, channels have the same age or not (see figure 4.13, down). This subdivision between "highland" ($HNme_3$) and

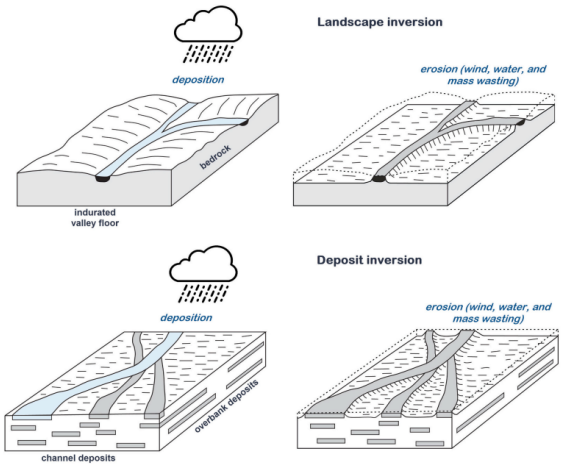

Figure 4.13: Diagram showing the formation of inverted channels through the two methods named landscape inversion and deposit inversion. In the case of landscape inversion, single or multi-thread valleys became inverted as a response to the lower resistance of the surrounding materials leaving the valley floor standing as a ridge. Deposit inversion is the exposure of a fluvial sedimentary body where former channel sediments are more resistant than surrounding materials. Credits (Zaki et al., 2021), (Dibiase et al., 2013).

"lowland" (Nhc_1) is also visible through the albedo and the roughness of the terrain: the highlands shows higher albedo and it hosts more rugged terrains, while the lowlands presents themselves as smoother and with lower albedo, especially on the right of the inverted channel. In figure 4.16 we present a RGB map of the cube obtained by combining the information from the HYD RGB map, the PFM RGB map and the MAF RGB map. To do so we suppressed the red band from the PFM and MAF RGB maps and also the blue band for the MAF RGB

map. Moreover we highlighted in light blue the course of the inverted channel. From this last map we can see that the lowland is subdivided into two different areas almost divided by the inverted channel, one being more mafic and the other one not showing particular mineralogies, with the exception of the areas near the mesas that shows high content in polyhydrated sulfate and the ejecta of two small craters that reveal some talc mineralogy, with mixed Mg/Fe smectite (the ROI we named PFM_1). Moreover, we can see that the global composition is different also for the right and left portion of the highlands: the phyllosilicates over the mesas seems to diminish and almost disappear on the left and the presence of monohydrated sulfates is higher on the right comparing to the left that is richer in polyhydrated sulfates. Using this map, the spectral information we obtained and the information given by the altitude profiles in figure 4.17 we can retrace the clear stratigraphy of the area (see figure 4.15): on the left part of the image and going from top to bottom we find the mixture in Magnesium and Iron smectites with some Aluminium smectites on top of the mesas, then at the foot of the mesas we find the monohydrated sulfate followed downward by the polyhydrated sulfate. The small crater ejecta seems to indicate a possible underlying component of talc, but it is not clear if it is a local deposits or if it underlies all the stratigraphy, while on the right of the inverted channel we see the absence of the phyllosilicates components and the presence of the base in mafic material that is dominated by low Ca pyroxene (as defined by table 2.4). It is important to notice that the first three components of the left stratigraphy are again inverted with respect to the classical disposition (Bibring and OMEGA Team, 2006): indeed we have phyllosilicates on top of sulfates in a unit that, always in the geological map from (Hynek and Di Achille, 2017), pertains to the Noachian/Hesperian boundary. Furthermore, from the altitude profiles in figures 4.17A, C, D and E it is easy to see that the lowland to the right of the inverted channel is lower than the one on the left by $\sim$20 m and it is at a height similar at the one occupied by the monohydrated sulfates.

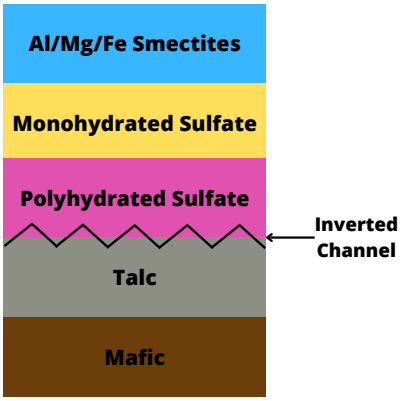

Figure 4.14: Proposed inferred stratigraphy of the area covered by FRT000062e6. The zigzag line represents an unconformity between successive layers (unconformity).

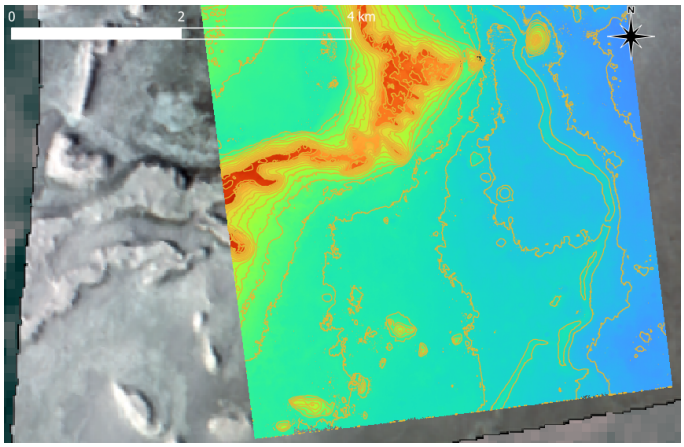

Figure 4.15: DTM of a part of FRT000062e6. The topographic contour lines are separated each by 10 m. From this image is easy to see the difference in elevation between the highland and the lowland and, moreover, it is also immediate the slow downward gradient in altitude from the left lowland to the right lowland. The highest part of the mesa cut by the DTM border on the contact between the lowland and the highland is the mesa on which we have found the mixture of Al/Mg/Fe smectite.

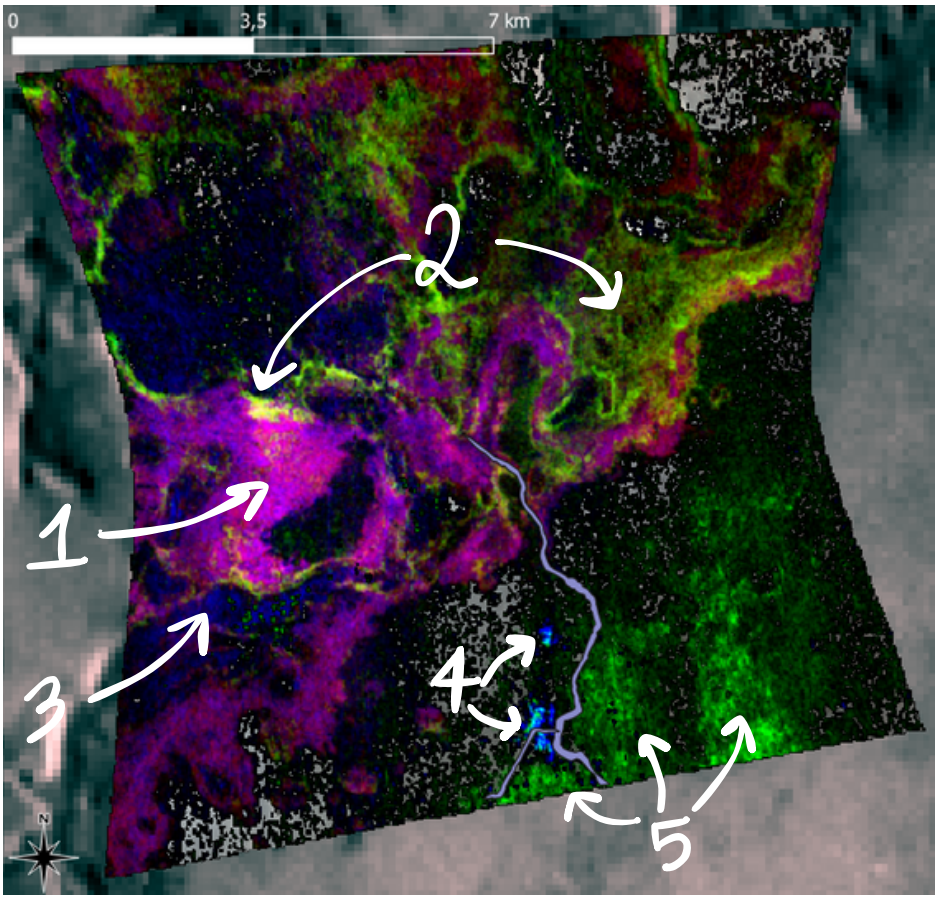

Figure 4.16: Combination of the HYD RGB map, the PFM RGB map and the MAF RGB map with highlighted inverted channel in cyan. The main map is the HYD map that covers all the highlands in which we see the polyhydrated sulfate (1), the monohydrated sulfate (2), the Al/Mg/Fe smectites on top of the mesas (3) and the border between higland and lowland, while the PFM RGB map highlights the talc bearing ejecta (4) and the MAF RGB map highlights the mafic material (5) shown in green in the lowland at the right of the inverted channel. From this we can also see the two division of the lowlands with the right containing mafic material in green and the left part harboring the talc containing ejecta and the polyhydrated sulfates that borders with the highland. From the HYD part of the map also the division of the highlands is visible with left part being bluer than the right (more phyllosilicates) and the right part being greener than the left (more monohydrated sulfates).

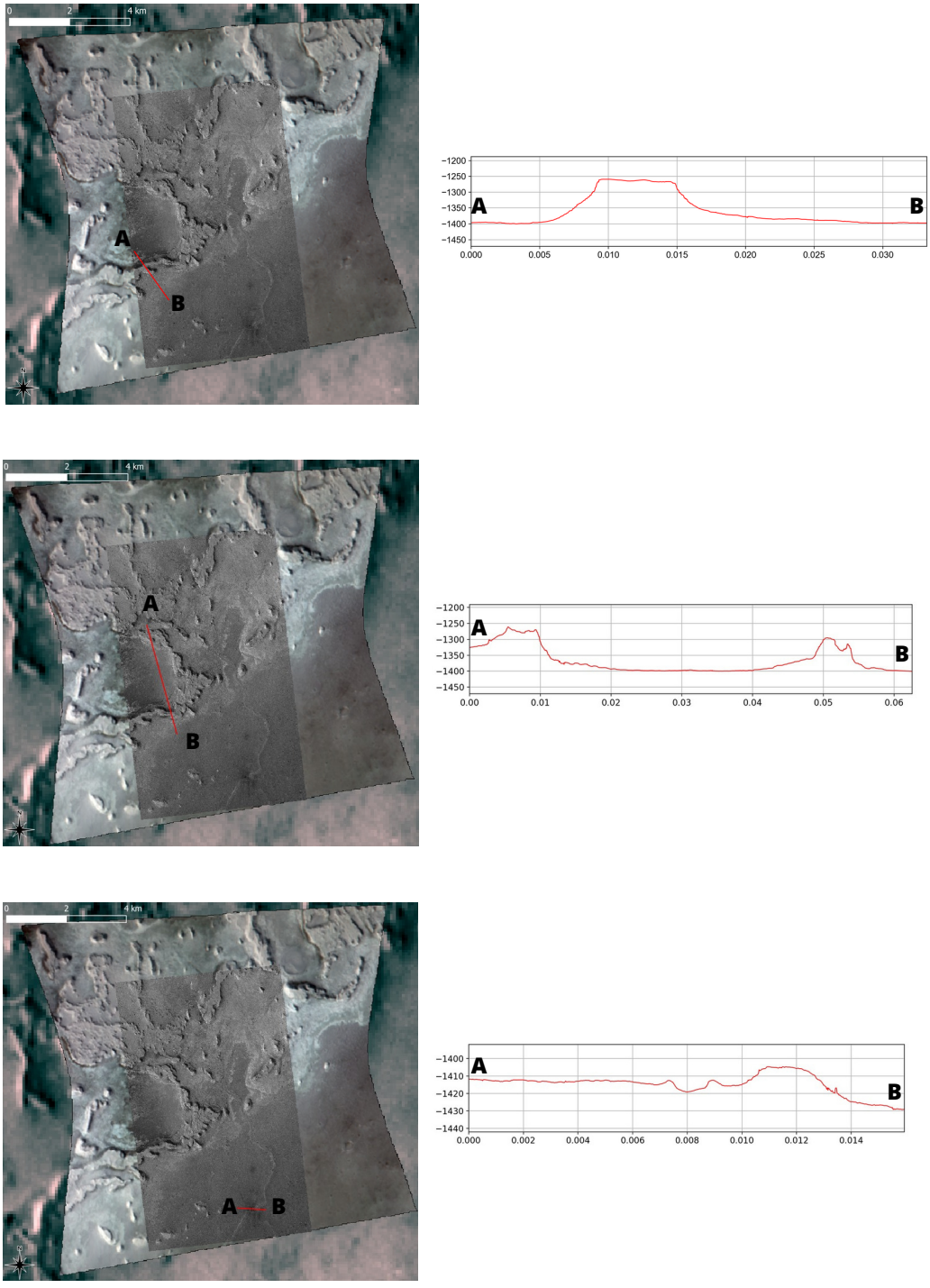

Figure 4.17: Extracted altitude profiles.

4.2 Summary and Global Interpretation

From all the evidences gathered locally in our three targets we see that the presence of water activity surely shaped this part of Meridiani Planum also during the Noachian/Hesperian boundary. In order to connect all our observations, we extracted a stratigraphic profile, using the Mars Laser Altimeter (MOLA) information, passing through the three targets. From figure 4.18 we can see that our targets are at different elevations, with the lowest point being inside Kai and the highest analyzed point being one of the mesas near Piscinas Serpentes. From these profiles we see that trying to stratigraphically connect the three different deposits is not as straightforward as it could seem and the three observations, although mineralogically similar, could have been deposited during different events at the Noachian-Hesperian boundary, unless some kind of deformation affected the area later, disrupting the elevation of the terrains.

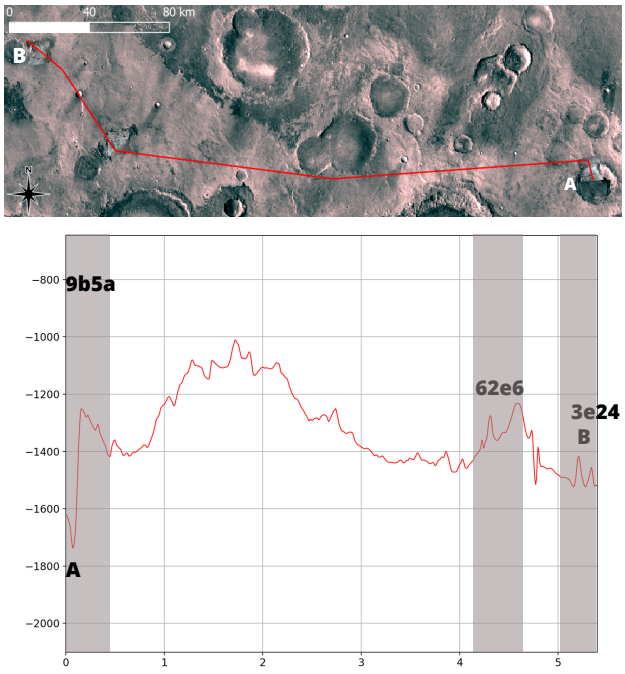

Figure 4.18: Altitude profile the interpolates our three targets. We can see that the deepest point in the track is indeed the sulfate-bearing floor of Kai crater. The units on the x-axis are units called "map unit" and are not to scale with meters, to have an idea of the distance see the top image's scalebar. The y-axis represents the altitude over the reference ellipsoid. The dotted lines represents the approximate border of the target's DTM crossed and are labeled accordingly.

5

Conclusions and Future Work

Summarizing all the information gathered from the spectral analysis, the morphology and the stratigraphy, and finally considering the avaliable information from the USGS geological map of Meridiani Planum (Hynek and Di Achille, 2017), we see that the Kai crater spans three geological units of different age (Nhc_1, c_1 and $HNme_u$), and reveals presence of:

- Aluminium smectite outside the rim;
- Remarkable succession of phyllosilicates on the rim, namely and in order from top to bottom being talc, Magnesium smectite and mixed Iron and Magnesium smectite;
- Sulfates, polyhydrated and monohydrated, and Iron smectite on the floor.

These last component pertains to $HNme_3$ unit, dating back to the boundary between Noachian and Hesperian, during which the wet conditions of Mars were shifting to more dry conditions. In terrains pertaining to this period we should expect to see sulfates on top of phyllosilicates, but as we demonstrate in this work, this is not our case, since we observe that sulfates occupy the bottom of our inferred stratigraphic sequence and more analysis should be conducted but surely this finding shed some light on this period, that surely is more complex and intricate than previously thought.
The small unnamed oblique crater presents a more chaotic scenario, but if the flapping phenomenon is truly the cause for the sulfates on the outer rim this is also another clue about the presence of water activity during the Noachian/Hesperian boundary. That is because the

impact should, at this point, been in a terrain with at least two strata, the upper one being of sulfate deposits and the lower one being the basaltic bedrock. Relatively dry conditions, marked by the presence of sulfates, surely were present for some time but then, later, a more substantial water activity should have started again, because of the traces of Magnesium and Iron smectite we see on the inner rim and because of the presence of layers on the crater floor.
One problem with this small crater is that we do not have a clear age associated to it and more analysis should be conducted to explore this more further. If the crater's infilling is of the same age as Kai's infilling, then we could reach conclusions similar to the ones we obtained for Kai, since we see polyhydrated sulfate deposits around the crater and phyllosilicates on the inner rim plus the layers in the crater's floor.
Lastly, the Piscinas Serpentes formation provides the most clean example of water activity during the Noachian/Hesperian boundary: the stratigraphy is pretty clear, revealing mixed Magnesium and Iron smectites with traces of Aluminium smectite on top of the mesas composing the $HNme_3$ terrain, with monohydrated sulfate being at the foot of the mesa and polyhydrated sulfate composing the last strata and continuing into the lower lands of the Nhc_1 terrain. Again, like for the floor of Kai crater, this is a huge clue about the complexity of the climate change Mars underwent during the Noachian/Hesperian boundary.
The talc found in the ejecta of the small craters on the right of the inverted channel is puzzling, since talc is thought to form by metamorphic processes involving magnesian minerals such as serpentine, pyroxene, amphibole and/or olivine in presence of CO_2 and H_2O (Bucher and Grapes, 2011). Indeed these crater are near the inverted channel, proving that before the deposition of sulfates, liquid water was surely present in this area, but this presence should have continued, at least as small groundwater reservoirs, at least up to the formation of these small craters.

All these findings are of extreme importance because they shed light over a not so well known period of the Red Planet history as with our analysis, and especially from the results of the first and third cubes (Kai crater and Piscinas Serpentes), we observe an inverted order of deposition between sulfates and clays with respect to what is classically found on Mars: phyllosilicates and sulfates on Mars seems to have formed under different climatic conditions and phyllosilicates, which are usually associated with Noachian terrains, are usually found below the sulfates, with this last mineral usually associated with Hesperian terrains. Our analysis seems to indicate a more intricate and complex evolution of the martian climate (especially near the Noachian/Hesperian boundary) as we have found an inversion of the expected stratigraphy in the first and third cubes: here phyllosilicates are observed on top of sulfates. In the first and second cube

(Kai and the unnamed oblique impact) we also observe layered materials seemingly composed of a mix of phyllosilicates and sulfates, whose detailed investigation is the subject of a parallel project by Baschetti et al. (Baschetti et al., 2023) and may hint at an even more complex scenario with multiple, high-frequency deposition events driven by oscillations of regional, possibly global, climatic conditions. These results will useful to better characterize and understand the changes that Mars underwent from its wet past to its dry present.

It is worth to mention that the code we wrote will be used as a back-end code for a Python dashboard that will be created using the Python module Panel. This will be done to create a user friendly alternative to present programs that could be used also by students and/or professionals that do not posses high levels of knowledge in Python or programming in general. This could improve by lots both the availability of spectral analysis tools regarding CRISM data products and the scientific and teaching production regarding this particular field that is reflectance spectroscopy.
Moreover, this work will be included in a broader project taken on by my supervisor and co-supervisor.

Bibliography

Andrews-Hanna, J. C. and Lewis, K. W. (2011). Early Mars hydrology: 2. Hydrological evolution in the Noachian and Hesperian epochs. *Journal of Geophysical Research (Planets)*, 116(E2):E02007.

Baker, V. R. (2001). Water and the martian landscape. , 412:228–236.

Baschetti, B., Massironi, M., Carli, C., Altieri, F., and Frigeri, A. (2022). Clay and sulfate-bearing terrains in Northern Meridiani Planum, Mars: constraining the characteristics of Mars' early climate at the Noachian-Hesperian boundary. In *European Planetary Science Congress*, pages EPSC2022–222.

Baschetti, B., Tullo, A., Massironi, M., Frigeri, A., Carli, C., and Altieri, F. (2023). Interbedded clay and sulfate deposits in Meridiani Planum, Mars: a valuable insight on the planet's ancient climate at the Noachian-Hesperian boundary. In *Biennial European astrobiology conference*.

Berman, D. C. and Hartmann, W. K. (2002). Recent Fluvial, Volcanic, and Tectonic Activity on the Cerberus Plains of Mars. Icarus, 159(1):1–17.

Bibring, J. P. and OMEGA Team (2006). Mineralogic Diversity of Mars and Discovery of Sulfate Deposits from the OMEGA/Mars Express Investigation. In LPI Editorial Board, editor, *Workshop on Martian Sulfates as Recorders of Atmospheric-Fluid-Rock Interactions*, volume 1331 of *LPI Contributions*, page 12.

Bucher, K. and Grapes, R. (2011). *Petrogenesis of Metamorphic Rocks*.

Calvin, W. M., Shoffner, J. D., Johnson, J. R., Knoll, A. H., Pocock, J. M., Squyres, S. W., Weitz, C. M., Arvidson, R. E., Bell, J. F., Christensen, P. R., de Souza, P. A., Farrand, W. H., Glotch, T. D., Herkenhoff, K. E., Jolliff, B. L., Knudson, A. T., McLennan, S. M., Rogers, A. D., and Thompson, S. D. (2008). Hematite spherules at Meridiani: Results from MI, Mini-TES, and Pancam. *Journal of Geophysical Research (Planets)*, 113(E12):E12S37.

Carr, M. H. (2012). The fluvial history of Mars. *Philosophical Transactions of the Royal Society of London Series A*, 370(1966):2193–2215.

Carr, M. H. and Head, J. W. (2010). Geologic history of Mars. *Earth and Planetary Science Letters*, 294(3-4):185–203.

Clark, R. N. (1999). *Spectroscopy of Rocks and Minerals, and Principles of Spectroscopy*.

Clark, R. N., King, T. V. V., Klejwa, M., Swayze, G. A., and Vergo, N. (1990). High spectral resolution reflectance spectroscopy of minerals. J. Geophys. Res., 95:12653–12680.

Cloutis, E. A., Hawthorne, F. C., Mertzman, S. A., Krenn, K., Craig, M. A., Marcino, D., Methot, M., Strong, J., Mustard, J. F., Blaney, D. L., Bell, J. F., and Vilas, F. (2006). Detection and discrimination of sulfate minerals using reflectance spectroscopy. Icarus, 184(1):121–157.

Comins, N. F. (2009). *Discovering the Essential Universe, Fourth Edition*.

Dibiase, R. A., Limaye, A. B., Scheingross, J. S., Fischer, W. W., and Lamb, M. P. (2013). Deltaic deposits at Aeolis Dorsa: Sedimentary evidence for a standing body of water on the northern plains of Mars. *Journal of Geophysical Research (Planets)*, 118(6):1285–1302.

Ehlmann, B. L. and Edwards, C. S. (2014). Mineralogy of the Martian Surface. *Annual Review of Earth and Planetary Sciences*, 42(1):291–315.

Ehlmann, B. L., Mustard, J. F., Murchie, S. L., Poulet, F., Bishop, J. L., Brown, A. J., Calvin, W. M., Clark, R. N., Des Marais, D. J., Milliken, R. E., Roach, L. H., Roush, T. L., Swayze, G. A., and Wray, J. J. (2008). Orbital Identification of Carbonate-Bearing Rocks on Mars. *Science*, 322(5909):1828.

Fassett, C. I., Goudge, T. A., Head, J. W., and Mustard, J. F. (2015). Open-Basin Lakes and the Climate and Surface Environment of Early Mars. In *46th Annual Lunar and Planetary Science Conference*, Lunar and Planetary Science Conference, page 1880.

Franz, H. B., Trainer, M. G., Malespin, C. A., Mahaffy, P. R., Atreya, S. K., Becker, R. H., Benna, M., Conrad, P. G., Eigenbrode, J. L., Freissinet, C., Manning, H. L. K., Prats, B. D., Raaen, E., and Wong, M. H. (2017). Initial SAM calibration gas experiments on Mars: Quadrupole mass spectrometer results and implications. Planet. Space Sci., 138:44–54.

Greeley, R. and Spudis, P. D. (1981). Volcanism on Mars. *Reviews of Geophysics and Space Physics*, 19:13–41.

Grotzinger, J. P., Arvidson, R. E., Bell, J. F., Calvin, W., Clark, B. C., Fike, D. A., Golombek, M., Greeley, R., Haldemann, A., Herkenhoff, K. E., Jolliff, B. L., Knoll, A. H., Malin, M., McLennan, S. M., Parker, T., Soderblom, L., Sohl-Dickstein, J. N., Squyres, S. W., Tosca, N. J., and Watters, W. A. (2005). Stratigraphy and sedimentology of a dry to wet eolian depositional system, Burns formation, Meridiani Planum, Mars. *Earth and Planetary Science Letters*, 240(1):11–72.

Hartmann, W. K. (2005). Martian cratering 8: Isochron refinement and the chronology of mars. *Icarus*, 174(2):294–320. Mars Polar Science III.

Hartmann, W. K. and Neukum, G. (2001). Cratering Chronology and the Evolution of Mars. Space Sci. Rev., 96:165–194.

Head, J. W. and Marchant, D. R. (2003). Cold-based mountain glaciers on Mars: Western Arsia Mons. *Geology*, 31(7):641.

Horgan, B. H. N., Anderson, R. B., Dromart, G., Amador, E. S., and Rice, M. S. (2020). The mineral diversity of Jezero crater: Evidence for possible lacustrine carbonates on Mars. Icarus, 339:113526.

Hynek, B., M. and Di Achille, G. (2017). Geologic Map of Meridiani Planum. *U.S. Geological Survey Report*, page 3356.

Kasting, J. F. (1991). Co2 condensation and the climate of early mars. *Icarus*, 94(1):1–13.

Leask, H. J., Wilson, L., and Mitchell, K. L. (2007). Formation of Mangala Valles outflow channel, Mars: Morphological development and water discharge and duration estimates. *Journal of Geophysical Research (Planets)*, 112(E8):E08003.

Lewis, K. W., Aharonson, O., Grotzinger, J. P., Kirk, R. L., McEwen, A. S., and Suer, T.-A. (2008). Quasi-Periodic Bedding in the Sedimentary Rock Record of Mars. *Science*, 322(5907):1532.

Madden, M. E., Bodnar, R. J., and Rimstidt, J. D. (2004). Jarosite as an indicator of water-limited chemical weathering on Mars. Nature, 431(7010):821–823.

MICA (2019). The MICA Files, An introduction to the visible-near infrared spectral diveristy of Mars as observed by MRO/CRISM. *Johns Hopkins Applied Physics Laboratory*.

Murchie, S., Arvidson, R., Bedini, P., Beisser, K., Bibring, J. P., Bishop, J., Boldt, J., Cavender, P., Choo, T., Clancy, R. T., Darlington, E. H., Des Marais, D., Espiritu, R., Fort, D., Green, R., Guinness, E., Hayes, J., Hash, C., Heffernan, K., Hemmler, J., Heyler, G., Humm, D., Hutcheson, J., Izenberg, N., Lee, R., Lees, J., Lohr, D., Malaret, E., Martin, T., McGovern, J. A., McGuire, P., Morris, R., Mustard, J., Pelkey, S., Rhodes, E., Robinson, M., Roush, T., Schaefer, E., Seagrave, G., Seelos, F., Silverglate, P., Slavney, S., Smith, M., Shyong, W. J., Strohbehn, K., Taylor, H., Thompson, P., Tossman, B., Wirzburger, M., and Wolff, M. (2007). Compact Reconnaissance Imaging Spectrometer for Mars (CRISM) on Mars Reconnaissance Orbiter (MRO). *Journal of Geophysical Research (Planets)*, 112(E5):E05S03.

NASA CRISM Team (2006). CRISM Web Site.

Nimmo, F. and Tanaka, K. (2005). Early Crustal Evolution of Mars. *Annual Review of Earth and Planetary Sciences*, 33:133–161.

Pepin, R. O. (1994). Evolution of the Martian Atmosphere. Icarus, 111(2):289–304.

Putzig, N. E., Mellon, M. T., Kretke, K. A., and Arvidson, R. E. (2005). Global thermal inertia and surface properties of Mars from the MGS mapping mission. Icarus, 173(2):325–341.

Roddy, D. J. (1976). High-explosive cratering analogs for bowl-shaped, central uplift, and multiring impact craters. *Lunar and Planetary Science Conference Proceedings*, 3:3027–3056.

Savitzky, A. and Golay, M. J. E. (1964). Smoothing and differentiation of data by simplified least squares procedures. *Analytical Chemistry*, 36:1627–1639.

Solomon, S. C., Aharonson, O., Aurnou, J. M., Banerdt, W. B., Carr, M. H., Dombard, A. J., Frey, H. V., Golombek, M. P., Hauck, S. A., Head, J. W., Jakosky, B. M., Johnson, C. L., McGovern, P. J., Neumann, G. A., Phillips, R. J., Smith, D. E., and Zuber, M. T. (2005). New Perspectives on Ancient Mars. *Science*, 307(5713):1214–1220.

Tanaka, K. L. (1986). The stratigraphy of Mars. J. Geophys. Res., 91(B13):E139–E158.

Viviano-Beck, C. E., Seelos, F. P., Murchie, S. L., Kahn, E. G., Seelos, K. D., Taylor, H. W., Taylor, K., Ehlmann, B. L., Wisemann, S. M., Mustard, J. F., and Morgan, M. F. (2014).

Revised CRISM spectral parameters and summary products based on the currently detected mineral diversity on Mars. *Journal of Geophysical Research (Planets)*, 119(6):1403–1431.

Zabrusky, K., Andrews-Hanna, J. C., and Wiseman, S. M. (2012). Reconstructing the distribution and depositional history of the sedimentary deposits of Arabia Terra, Mars. Icarus, 220(2):311–330.

Zaki, A. S., Pain, C. F., Edgett, K. S., and Castelltort, S. (2021). Global inventory of fluvial ridges on Earth and lessons applicable to Mars. *Earth Science Reviews*, 216:103561.